Modeling and simulation of grinding processes based on a virtual wheel model and microscopic interaction analysis

by

Xuekun Li

A Dissertation

Submitted to the Faculty

of the

WORCESTER POLYTECHNIC INSTITUTE

in partial fulfillment of the requirements for the

Degree of Doctor of Philosophy

in

Manufacturing Engineering

by

_____

April 2010

APPROVED:

_____

Yiming (Kevin) Rong, advisor, John W. Higgins Professor of Mechanical Engineering.

Associate Director of Manufacturing and Materials Engineering.

ABSTRACT:

Grinding is a complex material removal process with a large number of parameters influencing each other. In the process, the grinding wheel surface contacts the workpiece at high speed and under high pressure. The complexity of the process lies in the multiple microscopic interaction modes in the wheel-workpiece contact zone, including cutting, plowing, sliding, chip/workpiece friction, chip/bond friction, and bond/workpiece friction. Any subtle changes of the microscopic modes could result in a dramatic variation in the process. To capture the minute microscopic changes in the process and acquire better understanding of the mechanism, a physics-based model is necessary to quantify the microscopic interactions, through which the process output can be correlated with the input parameters.

In the dissertation, the grinding process is regarded as an integration of all microscopic interactions, and a methodology is established for the physics based modeling. To determine the engagement condition for all micro-modes quantitatively, a virtual grinding wheel model is developed based on wheel fabrication procedure analysis and a kinematics simulation is conducted according to the operational parameters of the grinding process. A Finite Element Analysis (FEA) is carried out to study the single grain cutting under different conditions to characterize and quantify the grain-workpiece interface. Given the engagement condition on each individual grain with the workpiece from the physics-based simulation, the force, chip generation, and material plastic flow can be determined through the simulation results. Therefore, the microscopic output on each discrete point in the wheel-workpiece contact zone can be derived, and the grinding process technical output is the integrated product of all microscopic interaction output.

From the perspective of process prediction and optimization, the simulation can provide the output value including the tangential force and surface texture. In terms of the microscopic analysis for mechanism study, the simulation is able to estimate the number of cutting and

plowing grains, cutting and plowing force, probability of loading occurrence, which can be used as evidence for process diagnosis and improvement. A series of experiments are carried out to verify the simulation results. The simulation results are consistent with the experimental results in terms of the tangential force and surface roughness $\boldsymbol{R_a}$ for dry grinding of hardened D2 steel.

The methodology enables the description of the 'inside story' in grinding processes from a microscopic point of view, which also helps explain and predict the time dependent behavior in grinding. Furthermore, the process model can be used for grinding force (or power) estimation for multiple-stage grinding cycles which includes rough, semi-finish, finish, and spark out. Therefore, the grinding process design can be carried out proactively while eliminating 'trial and error'. In addition, the grinding wheel model itself can be used to guide the recipe development and optimization of grinding wheels. While the single grain micro-cutting model can be used to study the mechanism of single grit cutting under various complex conditions, it can also be used to derive the optimal parameters for specific grains or process conditions.

ACKONWLEDGEMENT

I would never have been able to finish my dissertation without the guidance of the committee members, help from friends, and support from my family.

I would like to thank the entire dissertation committee: Prof. Yiming(Kevin) Rong, Prof. Christopher. A. Brown, Prof. Richard D. Sisson, Jr., Prof. Mustapha S. Fofana, Prof. Bi Zhang, Dr. K. Subramanian, and Dr. Changsheng Guo. I would like to express my deepest gratitude to my advisor, Prof. Rong, for his guidance, caring, patience, and providing me with all sorts of support for doing research. This work would never have been done without his supervision and direction within the 4-year study.

I would like to thank Dr. Yinggang Tian, Mr. Lukasz A. Glinski, Mr. Ethan Weikleenget, and the fellows from Saint-Gobain R&D Center, Shanghai, for providing me helpful technical support and suggestions through the completion of the work.

I would like to thank Mr. Waleed Bin Rashid from WPI and the visiting Ph.D and undergraduate students from China, who as active teamwork participants, are always contributing their talent to the micro-cutting research with all their endeavors. I would also like to thank Third Wave System, for providing us the AdvantEdge™ FEM simulation software as well as the technical support for the micro-cutting study.

I would like to give a big thank you to all lab mates from CAM-Lab for their help and creating such a friendly and harmonious atmosphere to work in.

I would like to thank the Norton Fellowship and Teaching Assistant-ship from Worcester Polytechnic Institute as partial financial support.

Last but not the least; I would like to thank my grand-parents, my parents, and my wife Fang Liu, to whom this work is dedicated. They are always right there fueling the engine during my doctoral work and stand by my side through the good times and bad.

Table of Contents

List of Figures

1. Introduction

1.1. Introduction of Grinding Processes

Grinding is the common collective name for machining processes which utilize hard abrasive particles as the cutting medium [1]. As a material removal process, grinding has a long history ever since the Stone Age. The modern abrasive technology was only established relative recently through the introduction of grinding machines and synthetic abrasives in the 19th century [2]. Nowadays, grinding becomes the most critical surface finishing process which accounts for about 70% within the spectrum of precision machining [3]. The applications of grinding can be found in most industrial areas, including aerospace, automotive, transportation, medical devices and electronics where high surface quality and fine tolerance are required on the components. Despite of the industrial prominence of grinding operation, it seems that grinding still appears to be a 'black art' and receives the least understanding among all the material removal processes [4].

Grinding, as a complex machining process with large numbers of parameters influencing each other, can be considered as a process where the grinding wheel engage with the workpiece at a high speed. To achieve better process control a model is required to predict and demonstrate the whole life cycle performance in relation to the process input parameters. The process performance generally corresponds to the factors influencing either cost or quality; while the input parameters typically consists of the wheel specification, operational parameters, and the machine tool control methods. All the grinding performance characteristics are interrelated with the process input parameters through the wheel-workpiece contact zone. This becomes extremely complicated when comes to precise quantitative evaluation for the process performance due to the lack of perception in the wheel-workpiece contact zone [5]. Therefore,

viable grinding process modeling and control should be obtainable only if a more detailed understanding of the wheel-workpiece interaction is perceived [6].

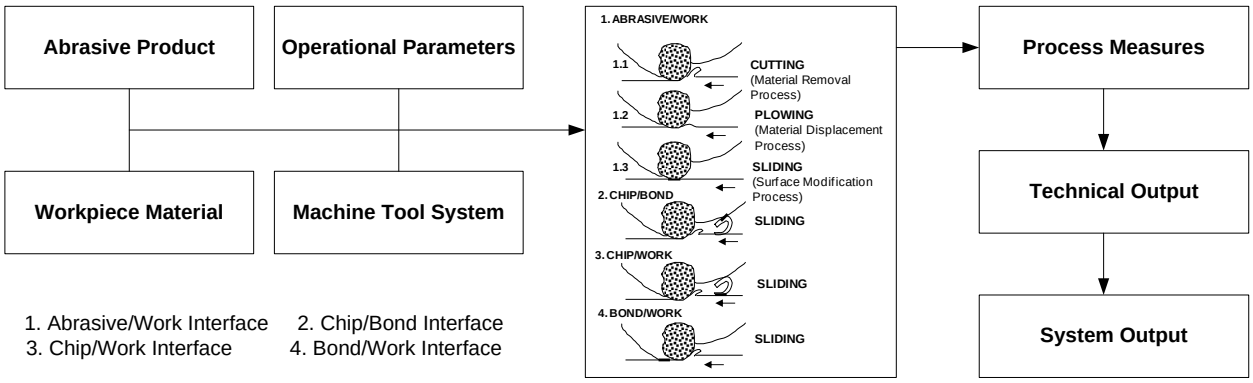

Figure 1 Systematic approach from Dr. Subramanian

It would have been impossible to synthesis a grinding process without a systematic approach considering the complex nature of grinding. When taking the process as a whole, every abrasive process is influenced by the abrasive product used, machine tool involved, work material and operational variables. All these four input categories interact with each other, which culminates in the output or abrasive machining process results. Irrespective of the choice of variables in the four input categories, for every grinding process it is possible to visualize the four interactions between the abrasive product and the work material in terms of abrasive/work interface, chip/bond interface, chip/work interface, and bond/work interface [7]. And Figure 1 indicates the decomposition of the 4 interface into 6 modes at the microscopic scale. For the grain/workpiece interface, cutting and plowing are characterized by the engagement condition as well as the chip formation. Cutting is defined when the grain-workpiece engagement is large enough and hence the workpiece material is removed in the form of chip; while plowing takes place when the engagement is fairly small and the workpiece is mainly experiencing plastic deformation instead of material removal. The workpiece surface is not generated by any of the sliding modes, but its properties could be modified due to the heat accumulation by friction.

From this perspective, every grinding process control strategy is therefore an effort to balance between cutting and plowing (surface generation) while minimizing the tribological interactions of sliding (which controls the characteristics of the generated surface). The ratio of the 6 modes in turn result in certain technical outputs, which when viewed based on the rules of manufacturing economics results in economic or system output. This input/output representation, namely “systems approach” [8] greatly simplifies the understanding and use of the principles of machining and tribology to manage and/or improve grinding processes.

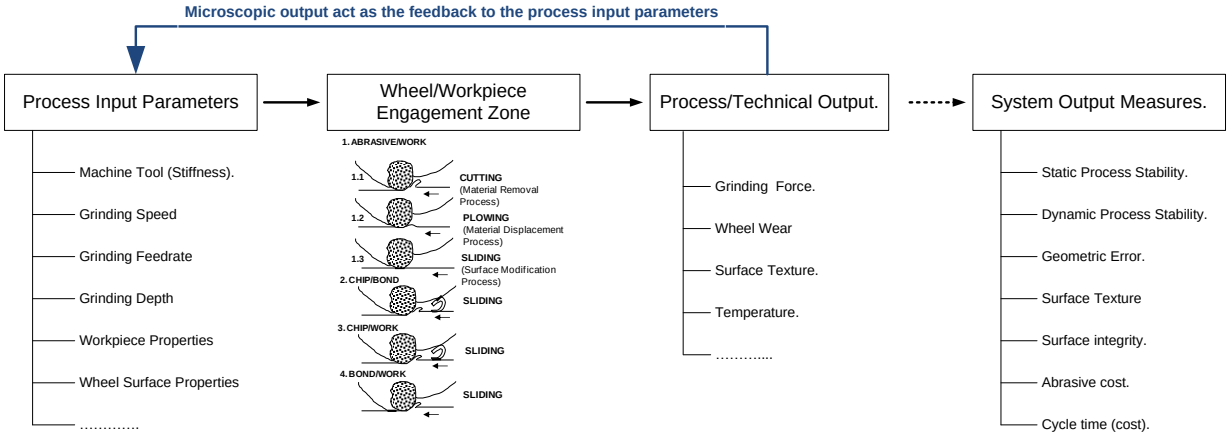

Figure 2 The detailed approach toward a dynamic/interactive grinding system

The perception of grinding process from the micro-level advances the understanding of grinding mechanism as indicated in Figure 2. Since the microscopic modes are intimately related with the process performance, the quantification of microscopic modes could definitely enhance the troubleshooting in grinding processes. The microscopic cutting and plowing are the major enablers for grinding force, and also contribute to the abrasive grain wear [9]. The grain wear, chip formation by an active grain, and localized force could result in the wheel surface condition alteration in terms of wear flat [10], loading [11; 12], and grain or bond breakage [13], respectively. The material removal by the grains and localized heat generated thereon could result the workpiece surface topography and metallurgy change [14]. And microscopic cutting as

well as its integration would influence the actual depth of grinding considering that the grinding system is not perfectly rigid [15; 16; 17]. From this perspective, the quantification of the 6 modes could help the grinding process understanding, monitoring, diagnosis, and optimization. And any minute change of the 6 modes that results in dramatic variation of correspondence grinding process behavior should be extracted for in-depth analysis in the model.

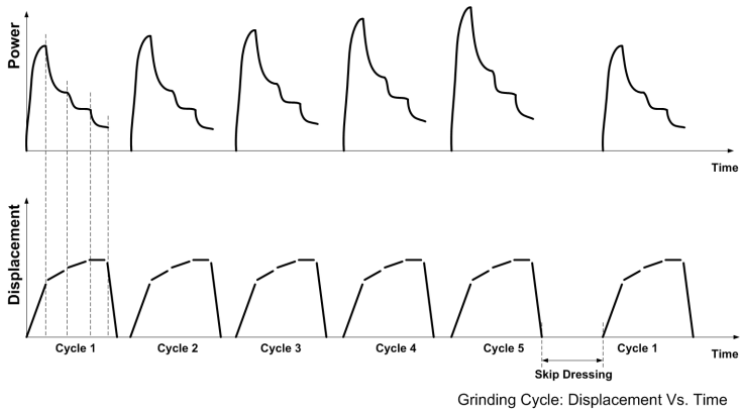

Figure 3 Grinding power change in typical OD grinding processes

Moreover, grinding processes exhibits a strong time dependent characteristic, which must be taken into consideration as a product of the microscopic modes for proactive process design. In industry where grinding power signal is widely measured for process monitoring, while the wheels get worn, loading, or glazing, the power curve will show a steady and gradual change as in Figure 3 [18]. Superimposing the power profiles of cycle 5 and cycle 1 makes the change visible, as shown in. Within one individual grinding cycle which consists of several segments: rough, semi-finish, finish, spark out, etc. the MRR-Power draw can be obtained by curve fitting into a straight line. And the MRR-Power draw change from cycle 1 to cycle 5 tells the “inside story” of the grinding process. An in-depth analysis of the MRR-Power draw, in, leads to the decomposition of the power in terms of threshold and cutting components and other time dependent components. Each one of these components in turn is associated with specific aspects of the microscopic interactions, as well as the wheel properties alteration leading to

such interactions. Figure 4 demonstrates a qualitative understanding of the MRR-Power draw change, which could predict grinding wheel surface conditions but still insufficient in providing an explicit solution for grinding optimization. And quantification of this power curve superimposition and MRR-Power draw for modern grinding process management still requires the analysis and modeling of grinding processes from a microscopic interaction perspective.

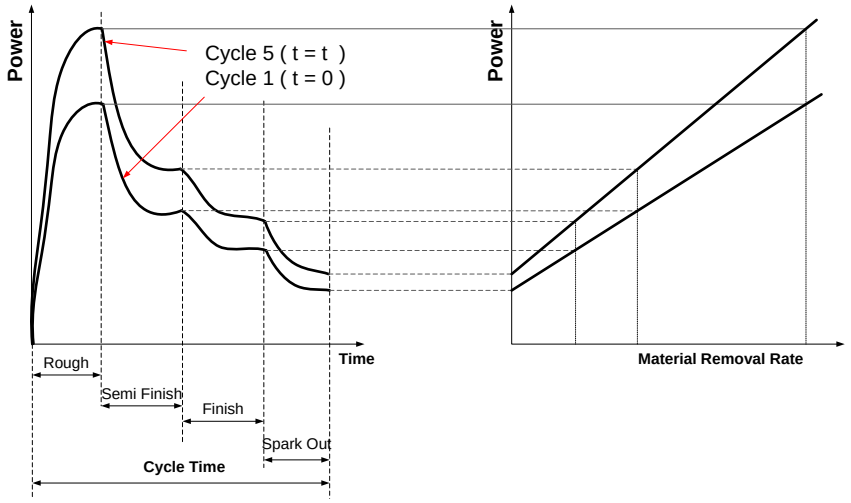

(a) Superimposition of power curves

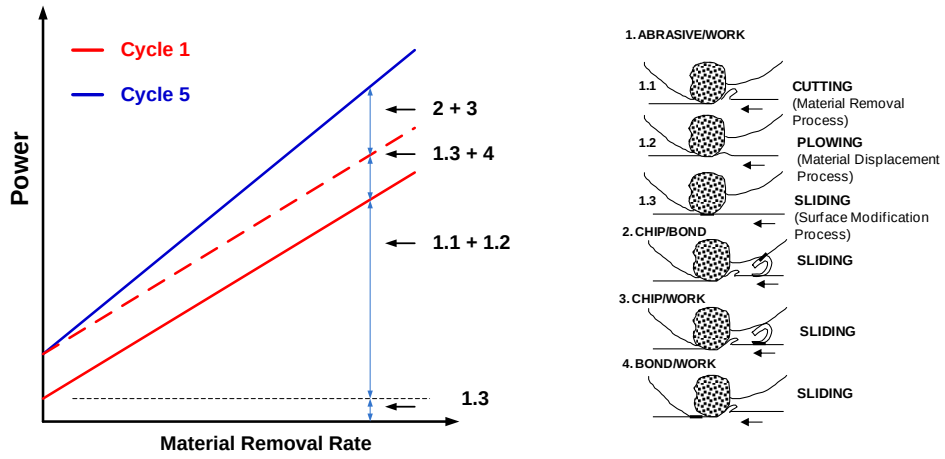

(b) Decomposition of the power curve and its correlation with 6 modes

Figure 4 Grinding power signals and the correlation with microscopic interaction modes

1.2. Literature Review on Grinding Process Modeling

Grinding process model describes the correlation between input and output quantities in order to predict the dynamic as well as the static performances. The relative work is really extensive, however, can still be subdivided into empirical models and analytical models. Figure 5 indicates the differences between the two modeling methods [19]. The empirical models are established through the measured data from grinding tests. According to the objectives, the correlation is established between the selected input and output parameters with a chosen model format, and then verified in further grinding tests. While for the analytical models, it is established based on the conformity of the process to the physical laws, using a mathematical formulation of the qualitative model. Therefore, the analytical models rely on the understanding of the physics behind the process and the subsequent physical models selected to describe the mechanism. And the accuracy of the models is typically dependent on the assumptions and how closely the model describes the physics. A comprehensive literature study is carried out to analyze various approaches toward grinding process modeling and their capability on revealing the grinding mechanism.

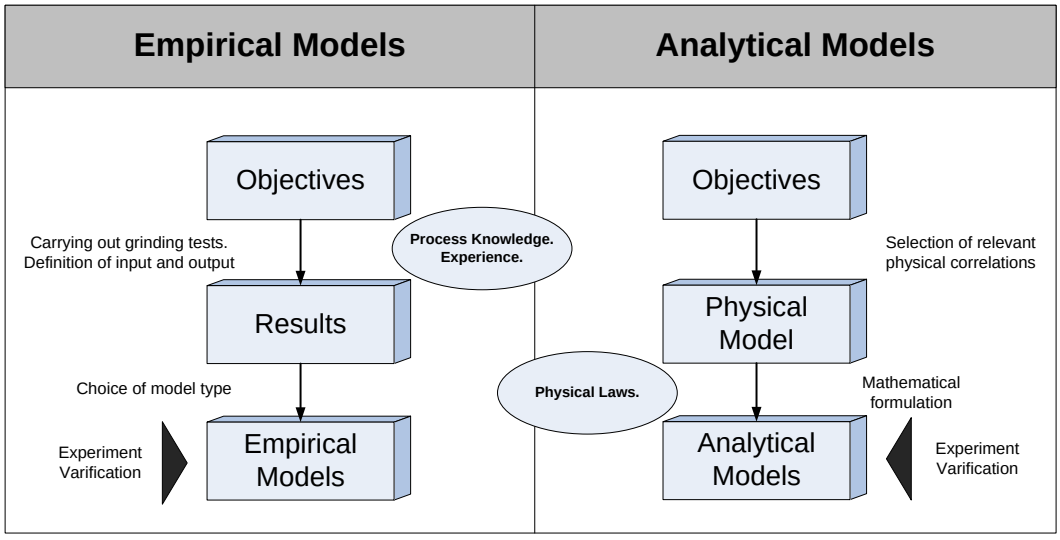

Figure 5 Comparison of empirical modeling and analytical modeling

1.2.1. Empirical Models

The empirical models are established by means of measured values which have been obtained in grinding tests. The popular approach for empirical models is to integrate expert knowledge into the process design or model system. The expert knowledge is represented by a domain of heuristic rules which are captured in a knowledge base [20]. With the rapid advent of computers, expert systems have seen a substantial growth in many grinding applications. A multi-agent approach, which consisted of case based reasoning, neural network reasoning and rule based reasoning is developed for the selection of grinding conditions [21]. Case based reasoning is employed as the main problem-solving agent to select combinations of the grinding wheel and values of control parameters. Rule based reasoning is employed where relevant data are not available in the case base. A neural network is employed to select a grinding wheel if required. However, the operator had to make the final decision about the wheel or the values of control parameters. Neural network and fuzzy logic is used to classify the condition of the grinding wheel cutting abilities for the external cylindrical grinding process [22]. The grinding force signal is measured, and some statistical and spectral features are extracted and calculated from the signal. The characteristic values are used as an input to compare with existing data in the database for wheel selection and classification.

In general, the conventional approaches using knowledge-based expert systems might encounter a difficulty when they are used as a means to develop an advisory system for grinding system design due to the next shortcomings. The expert knowledge is more qualitative than qualitative with the emphasis towards system integration and automation rather than basic study of process itself. It is difficult to incorporate and represent the nonlinear phenomenon and fundamental into the knowledge based system. Furthermore, the continuous rapid advent of new materials requires continual development of new process and might not allow time for knowledge and experience to be built up. Therefore, scientific research has to be performed and

the results of such research must be completed and comprehensive to cover the entire grinding system. What's more, the research must possess adequate mechanism to depict the grinding process in nature.

1.2.2. Analytical Models

Another category for grinding process modeling is to use analytical methods to avoid the 'black art' in empirical modeling. The literature on this aspect is rather broad and it would not be possible to cover it in any detail. As grinding force is the most important technical output measure and contributes almost all aspects of grinding system output, only pertinent literature dealing with force modeling is covered. Currently, there exist 3 popular approaches toward grinding force modeling, including statistical approach, energy approach, and physics-based approach.

1.2.2.1. Statistical approach

The statistical approach regards grinding as a multi-edge cutting process like milling. All contacting grains on the wheel surface are assumed to cut the workpiece material at the same depth of cut. The global grinding force, therefore, is the product of all force tensors on cutting grains. The single grain force is a function of the uncut chip thickness on the grain in the wheel-workpiece contact zone, which is obtained from a kinematics calculation. The statistical approach has a history of about 50 years, and can be summarized into a simplified format into Equation 1, which is expressed as a function of the depth of cut, speed ratio, and the equivalent diameter [4].

$$F = C \cdot N_{kin} \cdot h = C' \cdot \left({}^{1}/_{q}\right)^{D} \cdot {a_e}^{E} \cdot \left({}^{1}/_{d}\right)^{F} \quad (1)$$

where,

C is the constant associated with the process, which needs to be determined through experiments.

N_{kin} is the number of active abrasive grains.

h is the analytical average chip thickness on an active grain.

C' is the constant associated with the process, which needs to be determined through experiments.

q is the speed ratio of wheel speed divided by workpiece feed speed.

a_e is depth of grinding.

d is the equivalent diameter in grinding.

For this approach, the number of active grains is derived based on the assumption of equal-spacing of abrasive grains. The uncut chip thickness is calculated from the theoretical chip value. The generation of this theoretical chip is assumed to start at the moment the abrasive grains enters the workpiece and ends when it emerges from the workpiece. This consideration is based on the assumption of a 2-D problem that during chip formation. Neither plastic deformation nor plowing occurs at the edge of the trace. The geometry of the abrasive grains and the occurrence of traces overlapping are not considered, either. Various approaches toward the active grain count and equivalent chip thickness analysis are described in Table 1, and the multiplication of active grain numbers and single grain force gives the grinding force in global scale.

	NO. of Kinematics Grains.				Chip Thickness.			
Kurrein, 1927; Peters, 1969					h_{eq} =	(1/q)	a_e	
Shaw& Reichenbach, 1956					$h_{max} = {}_{1/2}(4/N\text{-}r)$	$(1/q)^{1/2}$	$(a_e)^{1/4}$	$(1/d_{eq})^{1/4}$
Konig & Kassen, 1969	N_{kin}= 1.5 •$(C_2^2/tg\ x)^{1/3}$	$(1/q)^{1/3}$	$a_e^{1/6}$	$(1/d_{eq})^{1/6}$	h_{max} = 2• Ls	(1/q)	$(a_e)^{1/2}$	$(1/d_{eq})^{1/2}$
Konig & Werner, 1971	N_{kin}= A• K_{gw}	$(1/q)^{m/n+1}$	$(a_e)^{m/2n+2}$	$(1/d_{eq})^{m/2n+2}$	N_{kin}= A• K'_{gw}	$(1/q)^{1/m+1}$	$(a_e)^{1/2m+2}$	$(1/d_{eq})^{1/2m+2}$
Konig & Lortz, 1975	N_{kin}= A	$(1/q)^m$	$(a_e)^n$	$(1/d_{eq})^n$				
Malkin, 1989					h_{max} = K_{gw}	$(1/q)^{1-m/2}$	$(a_e)^{1-m/4}$	$(1/d_{eq})^{1-m/4}$
Inasaki, 1989					$h_{max} = (L^2/r)^{1/2}$	$(1/q)^{1/2}$	a_e	$(1/d_{eq})^{1/4}$
Basic model.	N_{kin} = C_{gw}	$(1/q)^A$	$(a_e)^{A/2}$	$(1/d_{eq})^{A/2}$	h_{max} = C'_{gw}	$(1/q)^B$	$(a_e)^{B/2}$	$(1/d_{eq})^{B/2}$
Force model.	$F = C_{wp} \bullet C_{gw} \bullet N_{kin} \bullet h = C_{wp} \bullet C_{gw} \bullet (1/q)^D \bullet (a_e)^E \bullet (1/d_{eq})^F$							

Table 1 Summary of stochastic approach.

1.2.2.2. Energy Approach

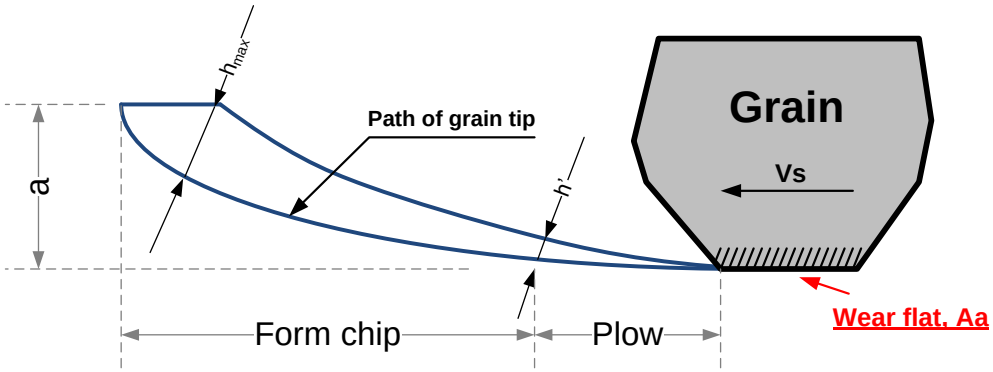

Figure 6 Chip formation, plowing and sliding.

The energy approach was initiated by S. Malkin more than 20 years ago [1]. It is assumed that the grains engaging with the workpiece would experience 3 stages, chip formation, plowing, and sliding, depending on the grain-workpiece engagement depth. Figure 6 demonstrates the 3 stages when the abrasive grain interact the workpiece at the specified conditions. Therefore, the overall energy consumption is the summation of all 3 components. Through the observation of the grinding chip (swarf), it indicated that the workpiece material was melted and then removed in grinding, which suggested the correlation of cutting energy consumption with material melting energy. In his theory, cutting energy is about 75% of the melting energy for most metallic material as indicated in Figure 7. The melting energy, for iron or steel, is about u_{ch}=13.8J/mm^3. And the value would change as the material element change. The chip formation force can be analogized from the energy consumption of chip formation. Plowing refers to the localized deformation of the workpiece material without removal, especially as the abrasive grains engage the workpiece causing permanent plastic deformation. And the tangential plowing force per unit width is estimated to be 1N/mm for steels as deduced from Figure 7. Sliding is associated with rubbing of dulled flattened areas on the abrasive grain tips (wear flats) against the workpiece surface. The sliding energy is a function of the wheel wear flat area, which is

developed on the tip of all abrasive particles. Based on the calculation, the global grinding force can be deduced accordingly in Equation 2 and 3.

$$u = u_{ch} + u_{pl} + u_{sl} = u(MMR) + u_{pl,Constant} + u(Ware\_flat) \quad (2)$$

$$F_t = F_{t,ch} + F_{t,pl} + F_{t,sl} \quad (3)$$

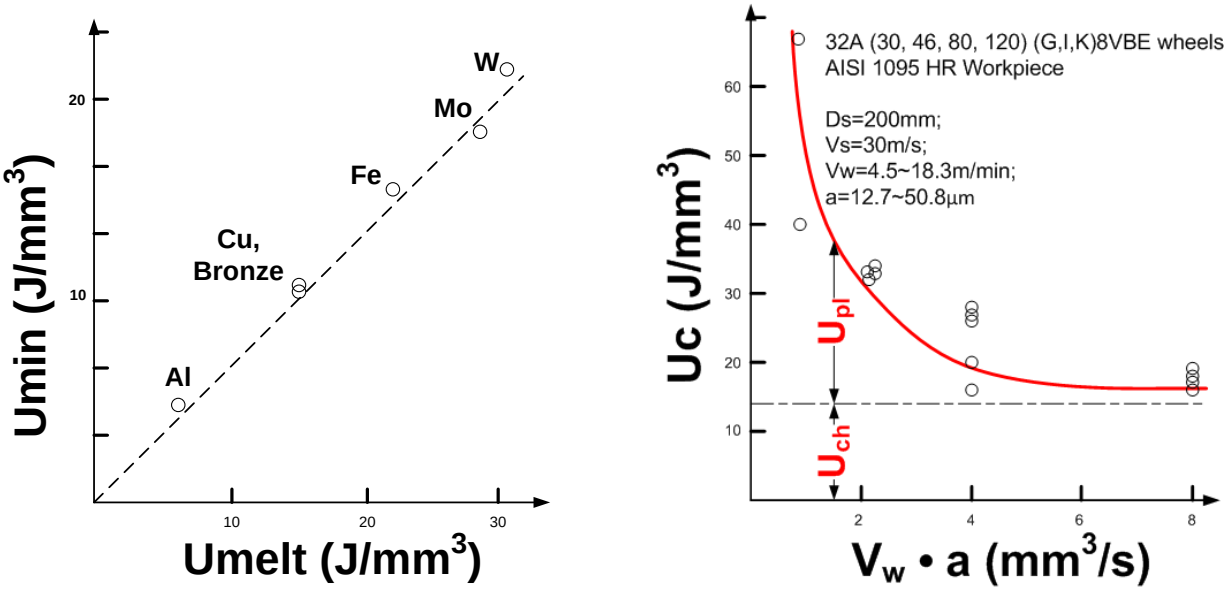

Figure 7 Determination of chip formation energy and plowing energy.

Unlike the statistical methods the energy approach models the grain/workpiece interface in terms of cutting, plowing, and sliding, which discriminates grinding process from a multi-edge cutting process. However, this approach is insufficient to provide any detail information regarding to the physics in the wheel-workpiece contact zone in terms of the micro-modes. And the ground surface texture in relation to the process parameter may not be estimated by this approach. In addition, the cutting and plowing energy calculation can be improved due to the recent progress of micro-machining Finite Element simulation package.

1.2.2.3. Physics based Approach

The concept of the physics based approach toward grinding process modeling was discussed in 1983, a paper from the CIRP Annual [23]. In general, the physics based grinding process modeling should cover all primary aspects of grinding process input. The methodology usually contains 2 folds: 1. analyzing the wheel-workpiece interface at a microscopic level through which the engagement condition of each single grain with the workpiece can be determined, and 2. calculating single grain force and integrating microscopic force tensor to the global scale. The starting point of this simulation is the digital wheel properties description, which can be established through measurement, analytical modeling, or mathematical modeling.

As of the grinding wheel surface measurement method, the cutting edges on a wheel surface can be measured through an optical profilometry by counting the peak points. A threshold value has to be set up, and all points that are higher than that are regarded as the active abrasive points. And the points that can form a close loop are regarded belonging to the same abrasive grain [24]. And the engagement of active abrasive grains with the workpiece can be treated as machining at micro-scale [25]. A topography model based on analytical analysis that assumed uniform, spherical grains arranged in bond material similar to a simple cubic unite cell packing can also be developed [26]. The number of cutting grains can still be calculated based on analytical formula [27; 28]. And the grinding process could be regarded as a multi-grain material removal process, and the grinding force equals to the sum up of cutting force on each single grain. When the random nature of grit distribution is incorporated into the model, a stochastic grit density function to describe the random grit distribution of the rotating wheel is studied, as shown in Figure 8 [29; 30].

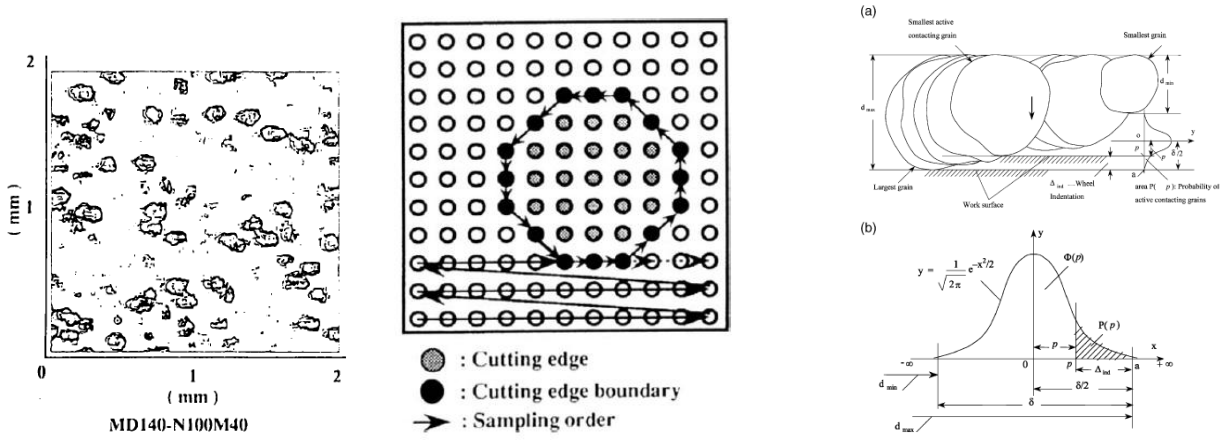

(a) Measurement of grinding wheel surface [24] (b) Statistical analysis of wheel surface [29]

Figure 8 Grinding wheel surface description

The determination of microscopic output for the engaging grain with the workpiece in terms of specific force, workpiece material side flow, chip formation, is another input required for the simulation apart from the wheel surface model. Various ideas are adopted for this calculation. The single grain cutting force can be regarded comparable to indenter-specimen interaction in Brinell hardness test in the absence of friction. Therefore, the specific force could be determined as the ratio between the tangential indention force and the cross-sectional area of an unreformed chip. And the side flow material shape is approximated as a parabola due to the material plastic deformation [31]. The cutting force on a single grit can also be calculated as a function of maximum chip thickness or chip length [27; 28]. Both Challen and Oxley's 2D plane-strain slip-baline field theory and Williams and Xie's 3D pyramid-shaped asperity model have been used to calculate grinding force on each single grain [25].

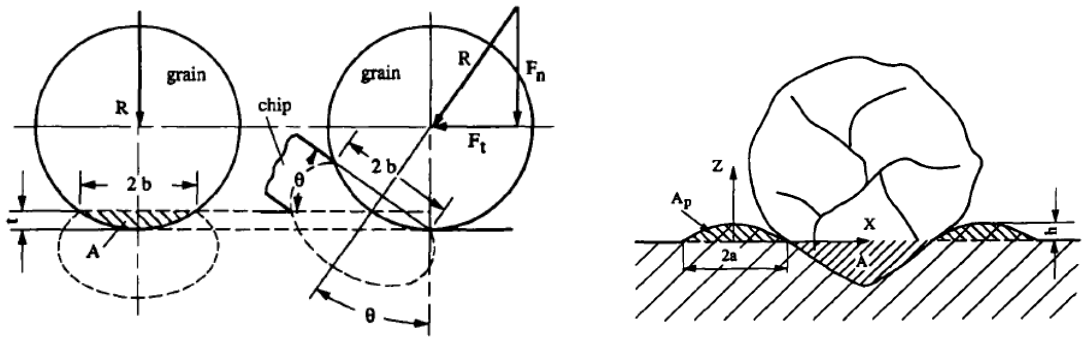

Figure 9 Specific force and side flow determination [31]

The grinding kinematics simulation serves to determine the wheel-workpiece contacting condition at the microscopic level. The general grinding kinematics simulation algorithm can be found in extensive literatures [1; 32; 33]. The most comprehensive kinematics simulation typically include: 1. Cutting point trajectory equation; 2. Cutting points trajectories and workpiece surface mapping; 3. Interaction determination of grains and workpiece; 4. Side flow profile update with respect to the workpiece surface.

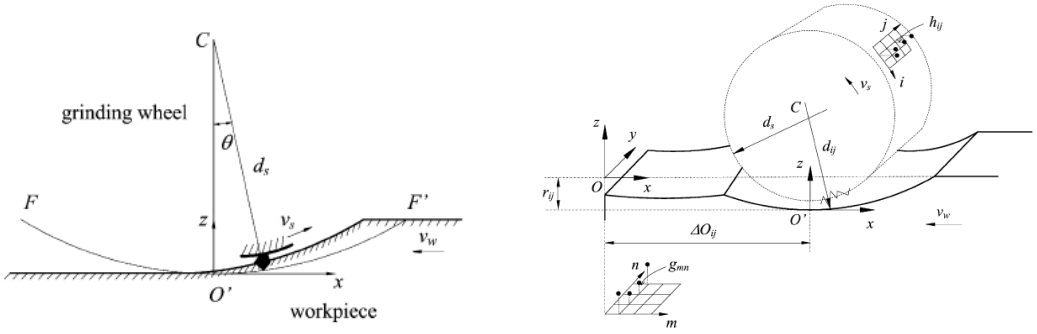

Figure 10 Representation of grinding kinematics [32]

Figure 10 shows the principle for a grinding kinematics simulation. If a ***O'xyz*** coordinate system is set with its origin ***O'*** fixed on the workpiece and coinciding with the grain at the lowest point the cutting path ***FO'F'*** of the cutting point is a trochoid formed by the superposition of the

circular motion around the wheel center at the velocity V_s and tangential motion along the workpiece at velocity V_w. The equation of the trochoid path is described as follows.

$$x = \frac{d_s}{2}\sin\theta \pm \frac{d_s \cdot v_w}{2 \cdot v_w}\theta \quad (4)$$

$$y = y \quad (5)$$

$$z = \frac{d_s}{2}(1 - \cos\theta) \quad (6)$$

Where x, y and z are the coordinates of on wheel superficial point, V_w is the velocity of the workpiece, d_s is the nominal diameter of the grinding wheel, and θ is the rotation angle of the wheel. The plus sign in the equation refers to up-grinding, and the negative to the down-grinding with the workpiece. Therefore, for any point $z(i,j)$, on the wheel surface with a distance d_{ij} to the wheel center, the position with reference to the coordinate system can be described as below.

$$x = \frac{d_{ij}}{2}\sin\theta \pm \frac{d_{ij} \cdot v_w}{2 \cdot v_w}\theta \quad (7)$$

$$y = y \quad (8)$$

$$z = \frac{d_{ij}}{2}(1 - \cos\theta) \quad (9)$$

All kinematic-based simulations of the grinding process require some schemes of mapping the cutting path to the workpiece surface. Suppose that the workpiece surface can be presented by a topographical array [g_{ij}]. Similarly, the grinding wheel topography can be described by an array of height [h_{ij}] with the indices i and j corresponding to the position of the topographical point h_{ij} in the peripheral and axial directions of the wheel, respectively. When the trajectory of the wheel points are translated from its local coordination system to the global coordinate system where the workpiece is, the workpiece surface topographic array can be updated as:

$$g_{mn}^{i} = min\{g_{mn}^{i-1}, z_{mn}\} \quad (10)$$

With g_{mn}^{i}, g_{mn}^{i-1} are the workpiece surface heights at point (***m, n)*** after and before cutting point $\boldsymbol{h_{ij}}$ passes through.

Depending on the grinding condition, only a small number of the abrasive grains on the grinding wheel will contact the workpiece surface. Among this small number of active grains, only a small portion will cut and form chips while the other will only plough or rub the workpiece surface. For the cutting and plowing grains, the workpiece material is also deformed plastically apart from removal. Therefore, the side flow geometry formation should be considered and included into the kinematics simulation. In current simulations, the cross section of the side flow can be modeled as an isosceles triangle or parabola. And the geometry can be modeled as a function of the engagement condition in terms of engagement cross section area, or engagement depth. The single grit scratch testing showed that the ratio could be varied from 70 to 100% for plowing, and 10–50% for cutting.

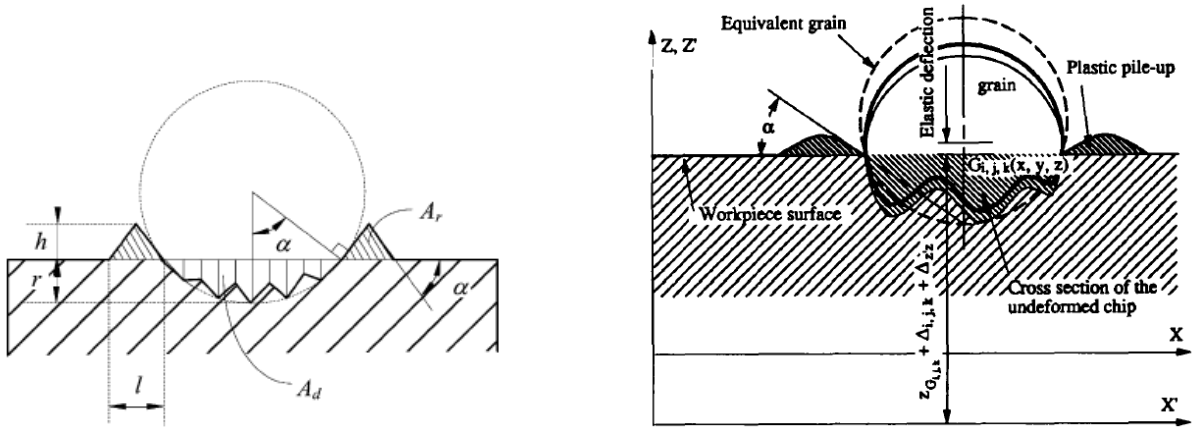

Figure 11 Side flow representation [32; 31]

The direct output from the kinematics simulation is the workpiece surface texture, which is reported in most process simulation literatures [31; 24; 33; 32]. The number of contacting or active grains can be derived from the kinematics simulation. The forces on each grain can be expressed as a function of grain-workpiece engagement cross section area [31; 24], or the

depth of cut on each grain [29]. The total grinding force can be determined by summing up the loads for all grains involved in grinding.

As the grinding process is very complex, and for grinding kinematics analysis, simplification is needed. For this reason, a few assumptions are made in current grinding simulations.

1. The vibration of the grinding wheel and system is negligible;
2. The material of the workpiece in contact with the cutting edges of the wheel is cut off when the wheel is fed into the workpiece;
3. No slide flow, built-up-edge phenomena (for some literatures).

1.3. Gaps between Industry Need and Academic Research

The analysis of the industrial need and current academic research status suggests that the gap mainly lie in two aspects: 1. a description of the grinding physics for better grinding process predictability [34], and 2. a prediction of their time dependent properties [18]. And a viable grinding process model cannot be established only if the following issues are considered and improved based on current academia research.

1. A physics-based grinding process modeling, aiming to characterize and quantify the 6 modes.
2. Sophisticated micro-cutting analysis, quantifying the microscopic conditions and advancing the state-of-the-art of material removal mechanism in grinding.
3. Improved grinding wheel model, complying with the 6 mode prediction on a time dependent basis.

1.3.1. Physics based Process Modeling

Although a grinding process can be regarded as a multiple edge cutting process, it indeed differs from the cutting process in two key areas: chip-bond/workpiece interaction and the bond-work interaction are absent in single or multiple-point cutting processes such as turning or milling [8]. The chip-workpiece and chip-bond friction may be prominent when the grinding wheel cannot cope with the quantity of chip produced. This applies to close-grained and in particular to hard wheels as a reduced proportion of porosity [35]. The accumulated chip attributes to the wheel surface condition change, causing extra friction and change on active cutting edges' geometry. The phenomenon of chip-workpiece and chip-bond friction is termed as loading, which accounts for 15% of wheel life termination [11]. In addition, wheel loading results in an increase in grinding forces and temperature. As a consequence, the rate of abrasive wear increases and the surface finish of the workpiece deteriorate.

Thus, the modeling of any grinding processes can be decomposed into 2 levels, the modeling of multiple edges micro-cutting (or grain-workpiece interactions) and the modeling of other frictional interactions that are introduced after the micro-cutting process. The literature review shed light on the modeling of grain-workpiece interactions from pervious physics based approach, which involves the determination of contacting grain numbers as well as force acting on each single grain. However, modeling of other frictional modes is not yet developed. Even more, the existing multi-edge cutting model needs further improvement to reflect the stochastic and micro-cutting nature in grinding.

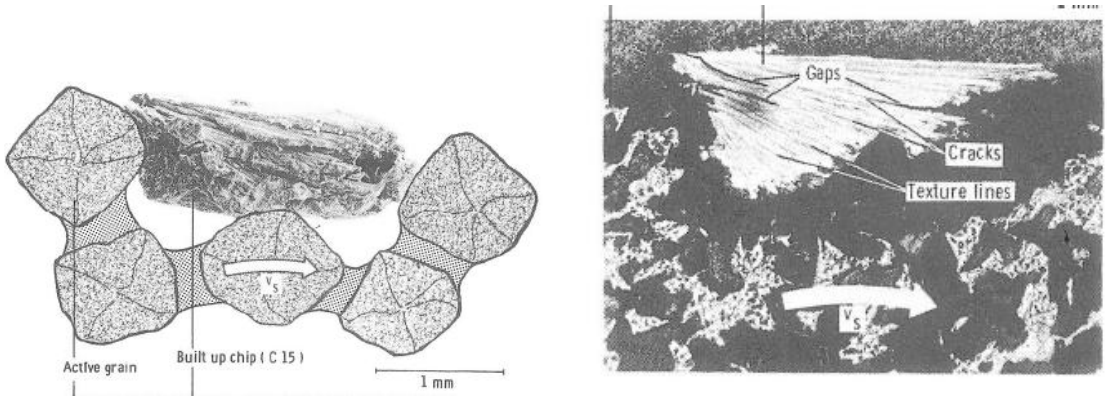

Figure 12 Loading phenomenon on grinding wheels [11]

Therefore, the microscopic frictional interactions, especially loading, must be identified and included in the grinding process model. A final explanation of the causative mechanism may open up new vistas towards grinding wheel loading and alleviation and avoidance. The effect of grinding wheel loading upon the metal cutting process and the development of the grinding forces are of a different nature. The geometric properties of chip clearance zone in front of an active grain change as the loading particles will build up primarily on or at the active grain edges, which hinder the chip formation of the grain in the next pass as well as enhance the probability chip-workpiece friction. Both of them result in a higher share of frictional forces occurring in the chip formation and lead to increased energy consumption. An increase of the share of frictional forces is additionally produced by the changed friction system. The frictional system grain-workpiece is replaced by the workpiece-workpiece or hardened workpiece-workpiece in the chip clearance zone, which result in a higher frictional system.

However, the modeling and quantification of wheel loading is not found in existing literature yet, due to the lack of understanding of loading mechanism. When loading is understood from a frictional interaction perspective, it would appear clear for loading modeling. Since loading occurs whenever the grinding wheel structure is unable to cope with the quantity of chips produced, it is believed that using the wheels with porous structure will definitely alleviate the

loading phenomenon [36]. Therefore, figuring out the effective pore volume and chip generated by a single abrasive grit would be two characteristic variables for the determination loading energy consumption. And the loading force can be estimated as a ratio of accumulated chip volume versus the effective pore volume. However, due to the insufficiency in single grain cutting analysis as well as the grinding wheel model, the required variables cannot be found in recent works.

1.3.2. Micro-cutting Analysis

The abrasive/workpiece interface contributes to the material removal directly and dominates the surface generation. Due to the similarity of a micro-cutting and a single grain cutting process, the micro-cutting theory can be used in the research. In the single grain cutting study, finite element simulation is the most up-to-date method to derive the specific force, side flow geometry, and chip formation that are required for the grinding process model [37]. In addition, the FEM simulation also helps understand the material removal mechanism by single grain, which may reveal the optimal grain geometry, process parameter for material removal in grinding processes.

A fundamental parameter for characterizing the micro-cutting process is the specific force (energy), which is defined as the force (energy) expended per unit material removal [1]. For most models the specific cutting energy or force is required to calculate the energy consumption or cutting force on each single grain. In most previous models, the specific cutting energy (or force) is treated as a constant value for the grain-workpiece interface, which is obtained from analytical equations or based on simplification. However, both simulations and experiments indicate that the specific cutting force varies as a function of cutting conditions, such as cutting speed, and depth of cut [38]. Particularly, when depth of cut varies from 0 to certain value that forms chip, specific cutting force will decrease drastically in a nonlinear manner, which is well identified as the “size effect” in grinding and machining as in Figure 13 [39; 40; 41; 42].

Considering that the real depth of cut for each grain vary a lot due to the stochastic nature of grinding, a constant specific cutting energy is no longer suitable for grinding force calculation. Especially for grinding, the fraction of micro-cutting dominates the overall surface modification, thus the simplification of specific cutting energy or force would yield inaccuracy with using a constant specific cutting energy (or force).

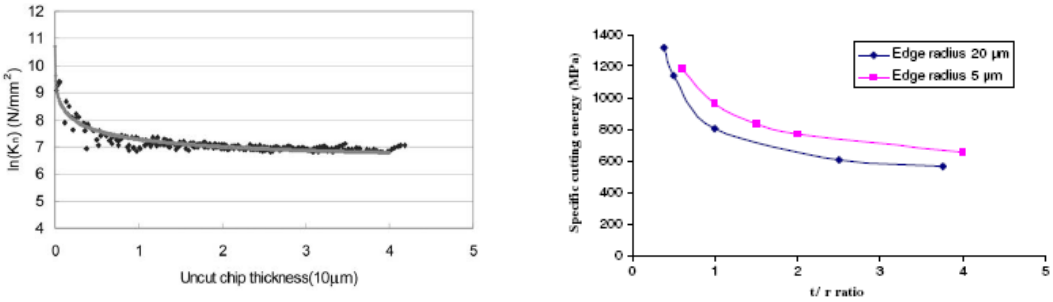

Figure 13 Specific cutting force Vs. depth of cut [41; 42]

Another critical phenomenon that has been overlooked in the micro-cutting in grinding is the side flow effects by single grain as well its effect on the next cut. In single grain cutting, the material around the cutting edge is subjected to sufficiently high pressure to cause the material to flow to the side [9]. The side flow material is always hardened compared with the matrix workpiece material due to the severe plastic deformation, which not only affects the surface roughness, but also increase force consumption of next cut [43; 44]. Considering the random and multiple-edge cutting nature in grinding process, the side flow formation would affect the material removal and energy consumption in a large extent, which indicates the interactive procedure among the abrasive particles. For most active abrasive grains they have to remove both matrix material as well as the hardened side flow material, as shown Figure 14. Thus how the grain shapes as well as cutting parameters are related with the side flow formation needs comprehensive investigation.

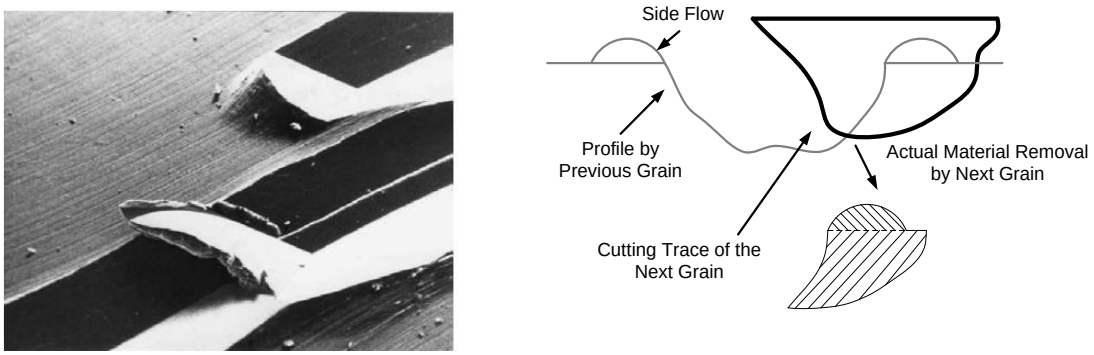

Figure 14 Surface modification by single grain [9]

1.3.3. Grinding Wheel Model

Most models deal with the grinding force based on a uniform grit distribution or an estimated average grit density on the wheel without considering the random nature of the grinding process. The random distribution of the grits position and protrusion height on the wheel surface, however, makes the grinding process stochastic in nature. Figure 15 shows the actual material removal and three possible types of undeformed chip shape due to the stochastic nature of grinding wheels [45; 46]. The first active grain cuts chip removed from a flat surface and the chip cross section will be the same as the grain profile. The shapes of the chip cross sections cut by the next active grains are more complex, as they depend on two successive active grain profiles. If the grain profile crosses a previous active grain profile, undeformed chip transverse cross section is asymmetrical (‘‘comma-like’’). The second shape occurs when sequential active grain profiles do not cross and undeformed chip shape is more symmetrical (‘‘boat-like’’). This phenomenon induces a slower material removal with higher energy consumption and a higher probability of plowing, which forms the primary features of a grinding process.

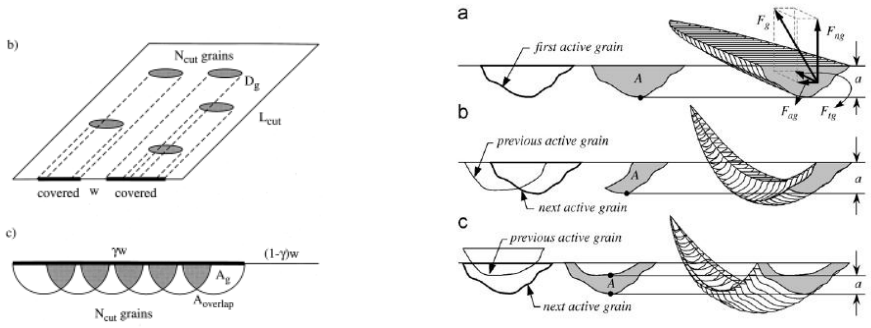

Figure 15 Material removal by single grain in grinding [46]

The representation of loading phenomenon also requires a sophisticated 3D grinding wheel model that includes both topographical and mechanical properties. The occurrence of loading is affected by the wheel localized pore volume and the chip generation in the process. Therefore, from a perspective of wheel modeling, the localized pore volume should be considered. The pore volume on a wheel surface typically is influenced by the wheel specification, fabrication procedure, and dressing process. However, current wheel models mainly focus on the wheel surface topography modeling based on the equal space distribution assumption [47] or arbitrary randomness assumptions of grains. Furthermore, the dressing procedure, in which the localized mechanical properties of the grinding wheel are involved, is seldom found in the current simulation. Therefore, a virtual grinding wheel model that bares resemblance with a real product appears to be essential for the process simulation.

1.4. Summary

Through the literature review and analysis, following summary can be made.

1. The industrial needs for grinding process modeling are identified as following.
   - A description of the grinding physics for better grinding process predictability, and
   - A prediction of time dependent microscopic behavior of grinding processes.
2. The existing literatures are analyzed, and their gap with the industrial need is concluded.

– A grinding process simulation should be established based on the physics analysis in grinding, and

– Finite element simulation could be a powerful tool to study the material removal in grinding, and

– A grinding wheel model which provides both wheel topographical and mechanical properties is in need.

1.5. Dissertation organization

Within the research scope, the dissertation is organized into 6 parts.

Chapter 1: Introduction and literature review.

– The industrial need for grinding process modeling is analyzed as the motivation of the research.

– The academic literature review on grinding process modeling with various approaches is conducted.

– The gap between industrial need and academic research is identified, which defines the research goal, objectives, and tasks. The research will focus on two aspects in the dissertation: 1. The formulation of the research methodology and framework; 2. The verification of the method.

Chapter 2&3: Research objective description and methodology establishment.

– The research methodology is established to model the grinding processes from a microscopic perspective for better predictability and physical understanding. The scope of the research is also defined in this chapter for a specific application – vitrified wheel grinding process.

Chapter 4: Virtual grinding wheel modeling and verification.

– The fabrication analysis based virtual wheel model method is proposed in this chapter, and corresponding mathematical modeling is carried out for vitrified grinding wheels. The virtual wheel model provides a digitalized grinding wheel structure with the capability of presenting the topographical and mechanical properties for the physics based simulation. To verify the efficacy of the method, simulation results are compared with the experimental values.

Chapter 5: Microscopic interaction mode analysis.

– The principle microscopic interaction modes for grinding process with vitrified wheel are studied, which provides the benchmark for the characterization and quantification of micro-modes in grinding.

Chapter 6: Process integration and verification.

– The kinematics simulation is conducted to determine the wheel-workpiece engagement condition under the specified grinding conditions. The localized kinetics condition is calculated based on the localized engagement condition and the microscopic interaction mode analysis in Chapter 5. And the final simulation results would be able to represent the grinding force usage for each micro-mode. The applicability of the model is verified by comparing the simulation results with the experimental data.

Chapter 7: Conclusion and future work.

– The conclusions are drawn, and potential applications as well as future work for the dissertation are discussed.

2. Research Objectives and Tasks

2.1. Research Objectives

As so far the process models that could demystify the wheel-workpiece contact zone are still missing, the goal of the research is to develop a predictive grinding process model that is derived based on the quantification of basic physical microscopic interactions. The objectives for the research, therefore, from the literature as well as the industrial need analysis can be deducted as following.

- To formulate the research framework of physics based grinding process modeling for better mechanism understanding.
- To establish the basic modules of the research framework, including the grinding wheel model, microscopic interaction analysis, and physics based process integration.

As of the process model, it should cover at least the input, output, and the process that correlates the input and output. Figure 16 describes the basic modules that constitute the model, which suggests that the completion of the research objectives generally involves 3 steps.

1. A grinding wheel model, which describes both surface topographical and mechanical properties. Among all the process input parameters, the wheel surface condition is the most complex and difficult to specify. When all other input parameters are fixed, the grinding wheel surface condition is the deterministic factors to microscopic interaction, and the change of the wheel surface conditions along the process is the fundamental cause of the time dependent behavior of grinding. The properties represented in the wheel model determine the capability to quantify the microscopic modes of the process model. Therefore, a grinding wheel model is a prerequisite for grinding process modeling,

through which the microscopic wheel properties and their change as a function of time should be presented.

2. The microscopic interaction model, which serves to categorize microscopic modes and quantify microscopic output. To specify and quantify the 6 interaction modes, some criteria should be deduced for the identification and modeling of each mode for given engagement condition at micro-level. The output of each single interaction mode, such as force (or power) consumption, heat source generation, should be correlated with the input parameters in the microscopic interaction model.

3. A physics-based simulation model, which provides the contact condition for each micro-mode and integrates the output value to the global scale for the technical output. To determine the input data for microscopic interaction model, physics based simulation is necessary, from which the contacting condition of each interaction can be specified from a kinematics perspective. Meanwhile, the microscopic force for each mode can be derived based on the kinematics simulation results through calling the data from microscopic interaction analysis. This step serves to convert the kinematics information to the kinetics information. The integration of the micro-scale output force (or power) provides the grinding force (or power consumption) in macro-scale, and the heat source that is discrete in nature can be deducted from the microscopic heat source for grinding temperature calculation.

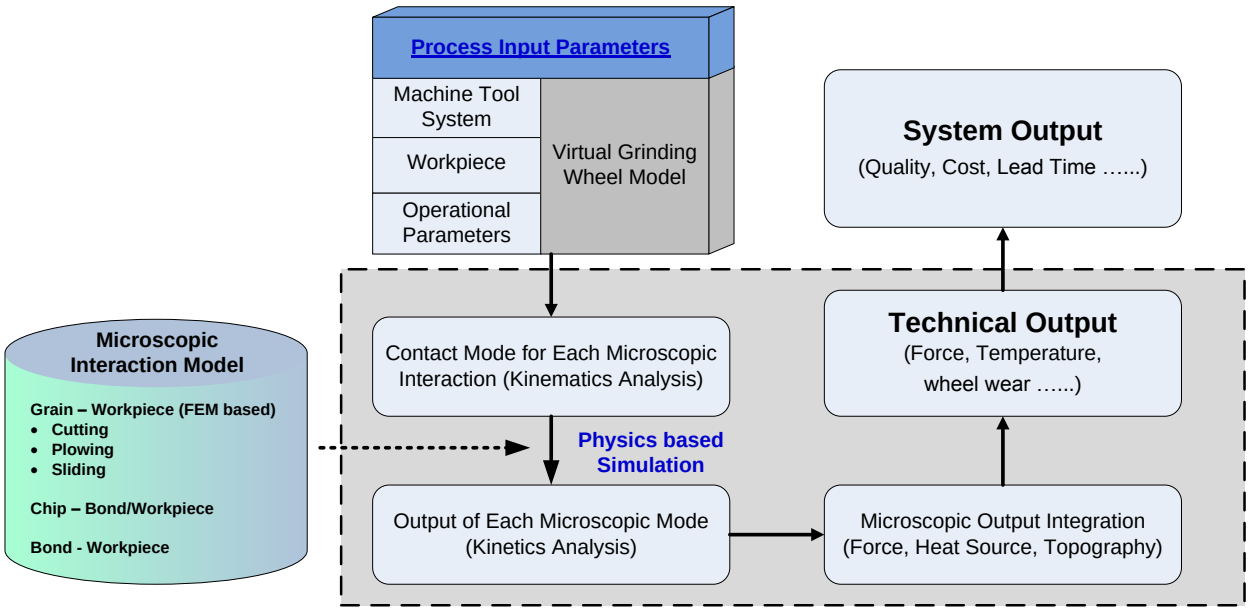

Figure 16 Flowchart of grinding process simulation

– To verify the process model in terms of tangential grinding force with test results or data from the literature.

2.2. Research Scope and Tasks

In order to verify the effectiveness of the research, a vitrified wheel grinding process simulation is carried out to compare with the experiment results in terms of tangential grinding force. Considering the intricate properties of vitrified wheel grinding with a perfectly rigid grinder, following assumptions are made:

1. The grinding system is considered to be perfect rigid, and the dynamic responses in grinding processes are not considered.
2. The grinding wheel surface change is mainly resulted from loading phenomenon due to the accumulated grinding swarf in the pores. Therefore, the grain/bond breakage and grain nose tip wear is neglected in the process.

3. The workpiece material metallurgy structure does not change during the grinding process.

The essence of grinding process is really complex, and dissertation research would have not been finished with a properly defined scope. Therefore, the scope and tasks of the research is defined as following:

1. Establishment of the research framework and the primary modules for grinding process modeling.
    - Virtual grinding wheel model.
    - FEM based 3D microscopic interaction analysis.
    - Programming of process integration.
2. Demonstration of the feasibility and effectiveness of the methodology by comparing with the experimental data.

3. Research Framework

Figure 17 describes the research framework for grinding process modeling. When all the input parameters are specified, the wheel-workpiece contact zone can be calculated macroscopically and microscopically. Therefore, through calling the microscopic interaction analysis module, the number and output of each mode can be derived. And corresponding microscopic output can be determined in terms of the grain wear, chip formation, force, heat density, and resultant surface texture change. It is the microscopic output affects the input parameters as feedback, and hence influences the transient properties during grinding. The integration of the microscopic output yields the technical output on the global scale, based upon which the system output can be calculated.

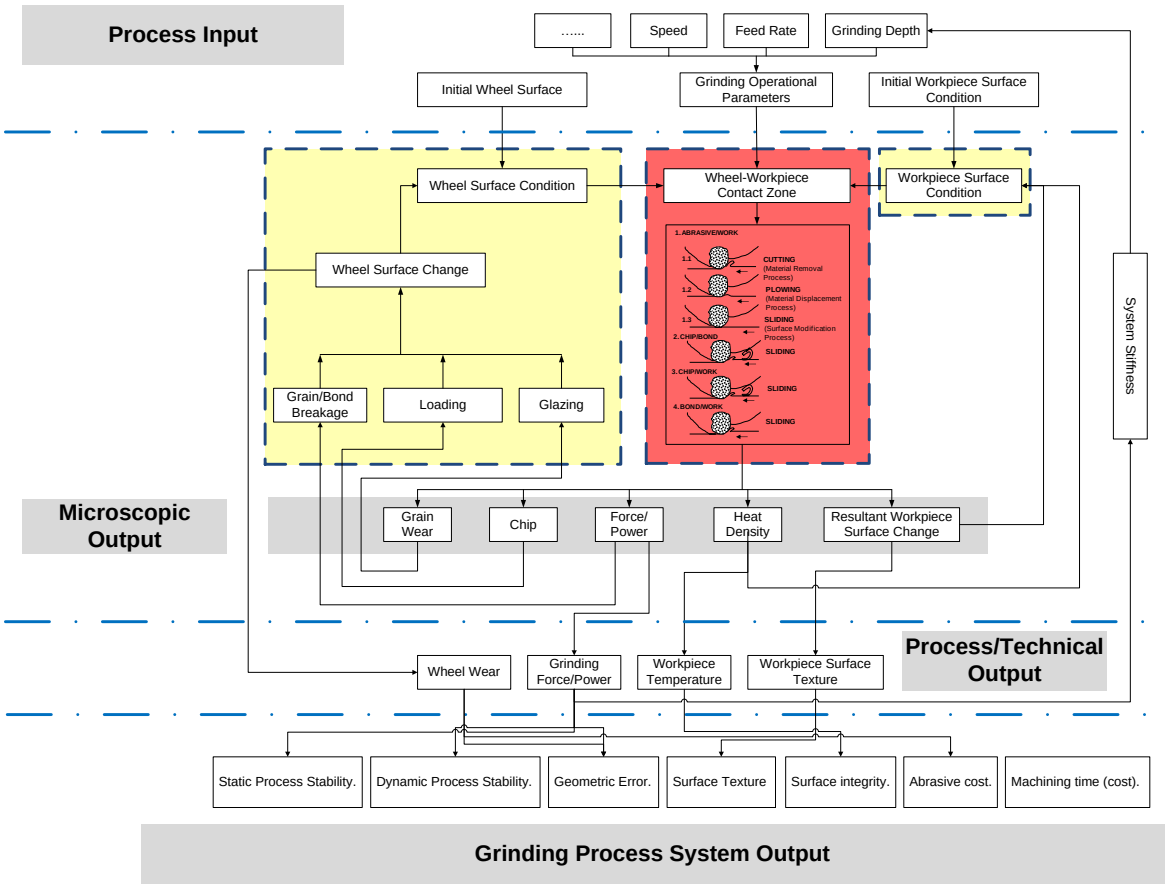

Figure 17 The framework of grinding process modeling

Taking the research scope into consideration, the research framework can be simplified as Figure 18, as the grain/bond breakage, workpiece material metallurgy structure change, and system deflection are not necessarily considered for vitrified wheel grinding process.

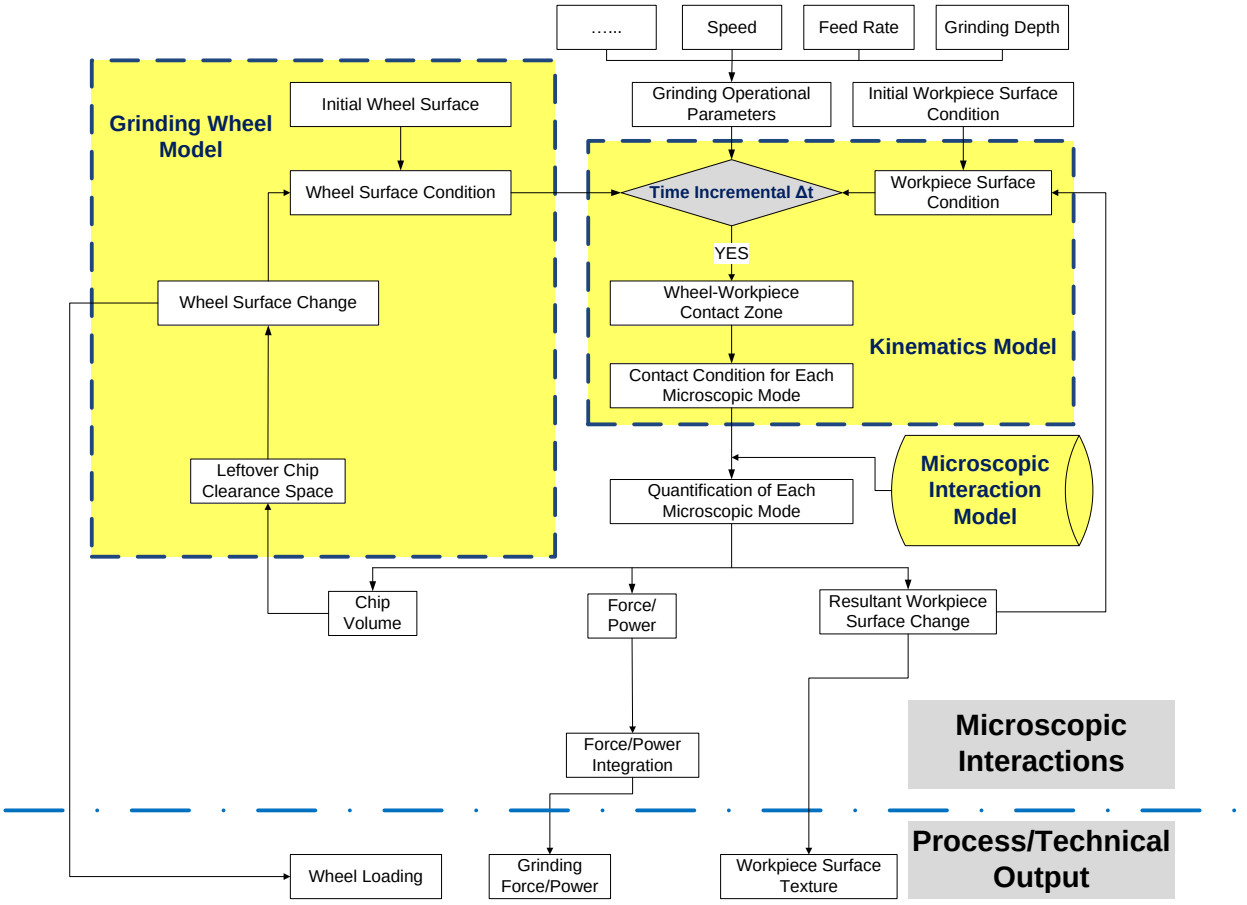

Figure 18 Framework of the research scope

In the modeling, the overall grinding process simulation can be regarded as an iteration procedure. At any time instance ***T***, the wheel surface condition, workpiece surface condition, and the relative motion parameter deduced from the operational parameter are determined as the model input. The mapping of the wheel surface and the workpiece surface in the kinematics model would provide the microscopic engagement condition for each mode at the wheel-work

contact zone. The engagement condition of each individual microscopic mode is the basis for calculation of all microscopic output.

1. The resultant surface texture can be derived in the kinematics simulation.
2. Given the engagement condition for all microscopic modes at the wheel-work contact zone, the microscopic force tensor can be estimated if the specific force is provided.
3. The chip generated by the micro-cutting mode can be estimated for the loading mode force calculation.
4. The grinding wheel wear in terms of abrasive grain wear, grain breakage, and bond breakage can be predicted when comparing the localized force with the localized wheel properties.
5. The localized heat source density can also be derived from microscopic force or power consumption.

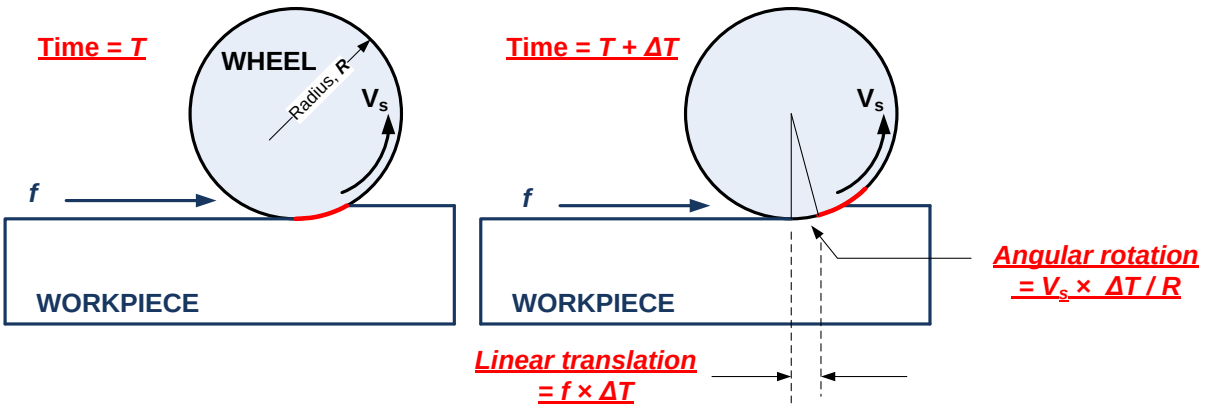

Figure 19 Kinematics in one iteration step

The integration of the microscopic output delivers the process as well as the technical output in each calculation step. For the next iteration step (***T+ΔT***), the grinding wheel will rotate at the degree of $V_s \times \Delta T / R$, and translate about $f \times \Delta T$ along the workpiece surface as indicated in

Figure 19. Therefore, the mapping of the wheel surface and workpiece surface will start again, initiating the next iteration.

3.1. Grinding Wheel Model

Currently, there exist two popular approaches for grinding wheel modeling. One approach is to use pure mathematical methods to simulate the wheel surface. The other is to apply statistical approaches to solve this problem considering random distribution of grains on the grinding wheel surface [47]. However, the pore volume and the mechanical properties of the wheel, which are critical to the grinding process, cannot be obtained from all the reported methods.

In order to provide the a virtual grinding wheel 3D morphology which is equivalent to a real product in terms of topography feature as well as mechanical features, a through-the-process modeling method is proposed. The idea is to utilize mathematical methods to intimate each wheel fabrication step, from raw material mixing to final wheel dressing. Not only the composition of wheel, such as grain size, grain shape, grain fraction, and bond fraction, but also the mechanics, and bond material diffusion during wheel firing are considered. After dressing simulation, the virtual wheel surface should bear resemblance with the real products in terms of static grain count, protrusion height, effective pore volume, and local wheel hardness.

3.2. Microscopic Interaction Analysis

Figure 20 show the 6 microscopic modes in grinding, which reflect the science of grinding processes. For the microscopic interaction model, it should provide the capability of characterization and quantification. Given the contact condition from the process integration model, the force as well as energy consumption should be derived accordingly. In addition, the microscopic interaction model itself also helps the understanding of mechanism in grinding.

The microscopic interactions can be grouped by mechanism into 3 categories: abrasive/workpiece, loading friction, and bond/workpiece friction, therefore, it is impossible to use one universal method to model all 3 modes. For the abrasive – workpiece interface, finite element simulation for micro-cutting with ThirdWave AdvantEdge^{TM} is used; while an analytical model is developed for the loading model as it has a diverse mechanism compared with the abrasive/workpiece interface. The bond – workpiece friction in the grinding with vitrified wheel is not prominent as the metal bonded wheel, therefore, the bond – workpiece friction is not considered within the research scope. In the following parts, the Finite Element Method analyses of abrasive/workpiece interface as well as the analytical study of loading phenomenon are carried out.

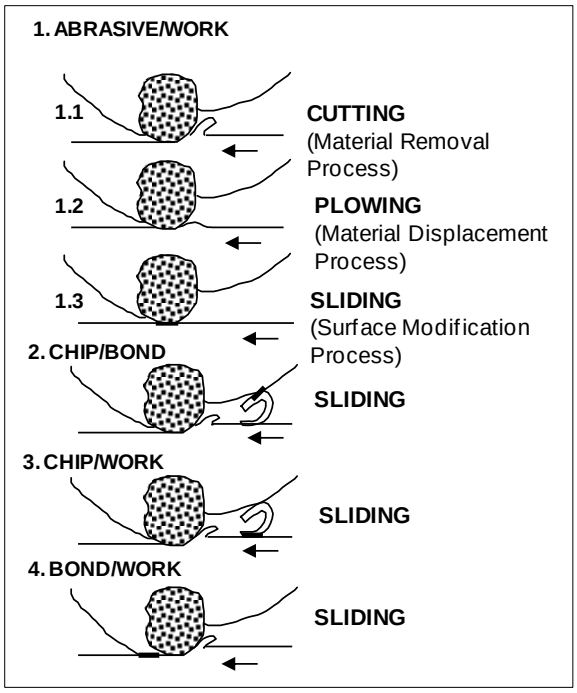

Figure 20 Microscopic interaction modes in grinding

3.3. Process Integration

The kinematics model serves to simulate the wheel moving against the workpiece under the specified grinding condition, which provides the number of contacting grains, contact cross-section area for each grain, and contact area of bond-workpiece interface, as shown in Figure 21. To determine the time dependent properties in grinding, the kinematics simulation is performed as an iteration procedure. During each iteration interval ***Δt***, the wheel surface move relatively respect to the workpiece complying with the grinding parameters. The material removed by the simulated wheel sample can be regarded equivalent to a triangular shape in cross-section, as indicated in Figure 21. Both wheel and workpiece surface conditions are imported from previous simulation step, based on which the wheel-workpiece contact mode is calculated. The workpiece surface will be updated after each time duration ***Δt*** and feedback as the input for the next iteration step. Through calling the microscopic interaction models, the force consumption for each single contact couple can be obtained. Integration of the all the microscopic force gives the grinding force (power) consumption in global scale, which also gives a discrete heat source moving along the workpiece surface for future grinding temperature calculation.

$$Grinding\ Force = Cutting\ force + Plowing\ force + Sliding\ force + Loading\ force + Bond\_Work\ force \quad (11)$$

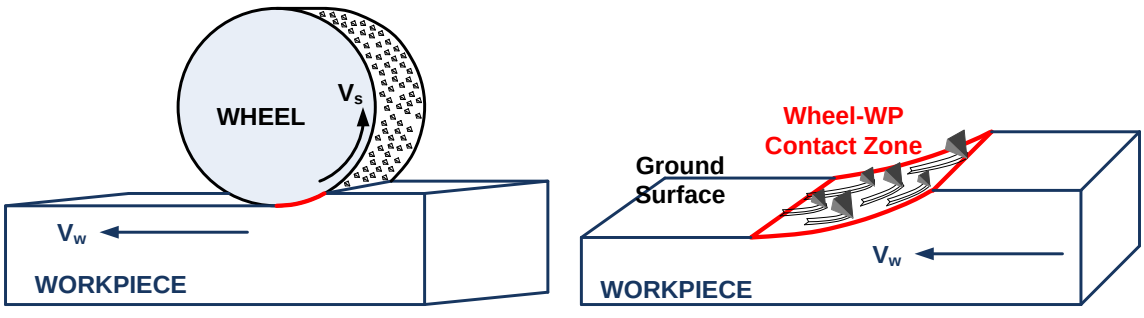

Figure 21 Grinding kinematics simulation

3.4. Summary

In this chapter, the objectives of the research are discussed. And to manage the research in a reasonable time frame, the research scope and tasks are defined as following:

- Establishment of the research framework and primary modules for grinding process modeling.
- Demonstration of the feasibility and effectiveness of the methodology by comparing with the experimental data.

In Chapter 4, 5, 6 the virtual wheel modeling, microscopic analysis, and physics based integration will be described in detail.

4. Virtual Grinding Wheel Modeling

In order to provide the a virtual grinding wheel 3D morphology which is equivalent to a real product in terms of topography as well as mechanical features, a through-the-process modeling method is proposed. The idea is to utilize mathematical methods to intimate each wheel fabrication step, from raw material mixing to final wheel dressing. Not only the composition of wheel, such as grain size, grain shape, grain fraction, and bond fraction, but also the mechanics, and bond material diffusion during wheel firing are considered. After dressing simulation, the virtual wheel surface should bear resemblance with the real products in terms of static grain count, protrusion height, effective pore volume, and local wheel hardness.

4.1. Grinding Wheel Fabrication Procedure

Manufactured grinding wheels are, in general, a composite of abrasive particles held together by bond material. Figure 22 indicates the typical structure of a grinding wheel. The void left in the wheel forms pores, which provide channels for lubrication and clearance for chips to escape the wheel matrix during grinding. The formation and distribution of pores in most grinding wheels are controlled by the natural packing of the ingredients in the mixture [48]. The manufacturing processes for most wheels vary slightly; in general, the following procedures apply. First of all, the abrasive grains with the required size and the bonding material are carefully weighted and mixed thoroughly. A slight amount of wetting agent is added to moisten the mixture so that the bond particles adhere to the grains during the entire process. Then a proper amount of the mixture is evenly distributed in a steel mould of the desired wheel shape and compressed hydraulically. After particle packing and compressing of the mixture, the green blanks are carefully fired in the kiln of accurate temperature control. This process causes the bond to melt and form a saturated case around each grain, which convert the green blank into a hard, durable grinding tool. Considering the extensive usage and uncomplicated fabrication

process compared with organic bonded wheel, the modeling of vitrified wheels is conducted in this paper. And its typical fabrication steps are described in Figure 23.

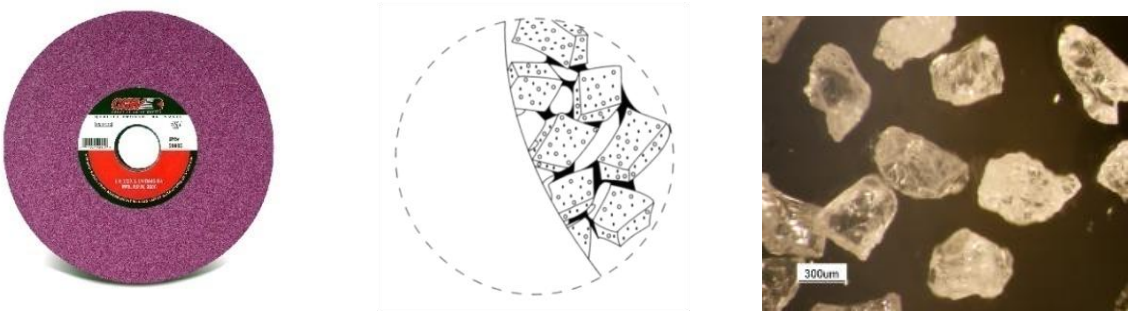

(a) Grinding wheel (b) Wheel structure (c) Abrasive particles

Figure 22 Grinding wheel structure

Figure 23 Grinding wheel fabrication steps

4.1.1. Raw materials mixing

Two important components, abrasive grains and bonding materials, make up any grinding wheel. Often, additives are blended to create a wheel with the properties necessary to shape a particular material in the manner desired. Usually, the ratio of the additives for conventional vitrified wheel accounts for around 1%; while that may reach up to 10% for organic bonded wheel.

Abrasive grains constitute the central component of any grinding wheel, and the hardness and friability of the materials will significantly affect the behavior of a given wheel. The bonding matrix in which the abrasive grains are fixed may include a variety of organic materials such as rubber, shellac or resin; inorganic materials such as clay are also used. Vitrified bonds with glass-like or vitreous structures are used on the precision machining wheels, while resin bonds

are used in masonry or steel-cutting wheels. Generally, resin bonds are used generally with coarse grains and for heavy metal removal operations such as foundry work. Vitrified bonds are used with medium to fine grain sizes in wheels needed for precision work.

(a) Grain (b) Bond (c) Grain and Bond mixture

Figure 24 Grinding wheel ingredients

In addition to their abrasive and bonding materials, grinding wheels often contain additional ingredients that produce pores within the wheel or assist chemically when a particular abrasive is used to grind a special material. One important aspect of a grinding wheel that can be created or altered through additives is porosity, which also contributes to the cutting characteristics of the grinding wheel. Porosity refers to the open spaces within the bond that allow room for small chips of metal and abrasive generated during the grinding process. Porosity also provides pathways that carry fluids used to control heat and improve the cutting characteristics of the abrasive grains. Without adequate porosity and spacing between abrasive grains, the wheel can become loaded with chips and cease to cut properly. A variety of products are used as additives to create proper porosity and spacing. For a conventional vitrified wheel, WA46L8V for example, the wheel receipt is comparatively simple, which only contains abrasive grains of grit 46, bond material, and less than 1% organic glue as initial bonding agent.

4.1.2. The molding process

Vitrified grinding wheels are manufactured by the cold-press method, in which a mixture of components is pressed into shape at room temperature. The details of processes vary considerably depending upon the composition of wheel and the practices of individual companies, which makes the wheels with the same specification may vary a lot for different wheel manufacturers. For mass production of small wheels, many portions of the process are automated.

4.1.2.1. Mixing the ingredients

Preparing the grinding wheel mixture begins with selecting precise quantities of abrasives, bond materials, and additives according to a specific formula. A binder, typically a water-based wetting agent in the case of vitrified wheels, is added to coat the abrasive grains; this coating improves the grains' adhesion to the binder. The binder also helps the grinding wheel retain its shape until the bond is solidified. All materials can be either mixed in a single mixer or in several separate steps.

During the mixing, the blend must be free-flowing and distribute grain evenly throughout the structure of the grinding wheel to assure uniform cutting action and minimal vibration as the wheel rotates during use. This is particularly important for large wheels, which may be several feet in diameter, or for wheels that have a shape other than the familiar flat disk.

4.1.2.2. Molding

For the most common type of wheel, an annular disc, a predetermined amount of grinding wheel mixture is poured into a mold consisting of four pieces: a circular pin the size of the finished wheel's arbor hole (its center hole); a shell with a 1-inch (2.5-centimeter) wall, about twice as high as the desired grinding wheel is thick; and two flat, circular plates with diameter

and arbor hole sizes equal to those of the wheel. A variety of methods are used to distribute the mixture evenly. Typically, a straight edge pivots about the center arbor pin to spread the mixture throughout the mold.

Using pressures in the range of 100 to 5000 pounds per square inch (psi) for 10 to 30 seconds, a hydraulic press then compact the mixture into the grinding wheel's final shape. Some manufacturers use gage blocks between the two face plates to limit their movement and establish uniform thickness. Others control wheel thickness by closely monitoring the consistency of the mix and the force of the press.

After the mold has been removed from the press and the wheel stripped from the mold, the wheel is placed on a flat, heatproof carrier. Final shaping of the wheel may take place at this time. All work at this stage has to be done very carefully because the wheel is held together by only the temporary binder. Lighter wheels can be lifted by hand at this stage; heavier ones may be lifted with a hoist or carefully slid on a carrier to be transported to the kiln.

4.1.3. Firing

Generally, the purposes of the firing are to melt the binder around the abrasives and to convert it to a form that will resist the heat and solvents encountered during grinding. A wide range of furnaces and kilns are used to fire grinding wheels, and the temperatures vary widely depending upon the type of bond. Wheels with a resin bond are typically fired at a temperature of 300 to 400 degrees Fahrenheit (149 to 204 degrees Celsius), and wheels with vitrified bonds are fired to temperatures between 1700 and 2300 degrees Fahrenheit (927 to 1260 degrees Celsius).

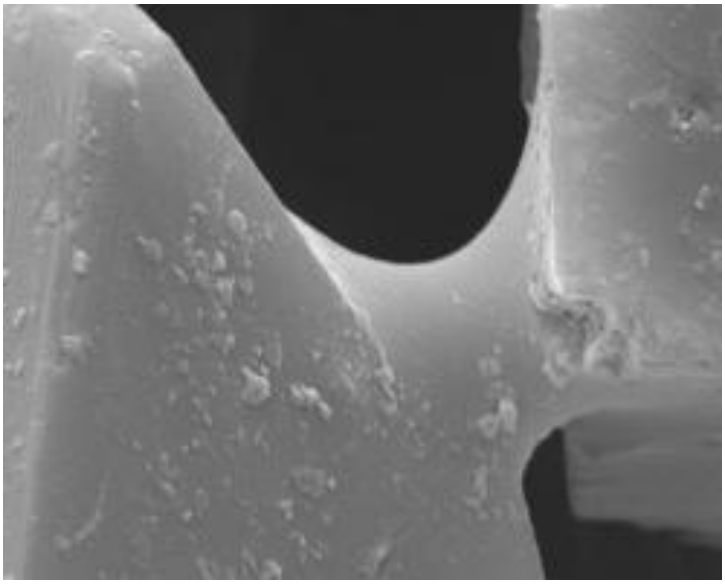

Figure 25 Formation of bond neck

4.1.4. Finishing

After firing, wheels are moved to a finishing area, where arbor holes are reamed or cast to the specified size and the wheel circumference is made concentric with the center. Steps may be necessary to correct thickness or parallelism of wheel sides, or to create special contours on the side or circumference of the wheel. Manufacturers also balance large wheels to reduce the vibration that will be generated when the wheel is spun on a grinding machine. Once wheels have received labels and other markings, they are ready for shipment to the consumer.

4.1.5. Summary

The extent to which grinding wheel quality is checked depends upon the size, cost, and eventual use of the wheels. Typically, wheel manufacturers monitor the quality of incoming raw materials and their production processes to assure product consistency. Special attention is given to large wheels for the strength and integrity of the bonding system as well as the

uniformity. Acoustical tests measure wheel stiffness; hardness tests assure correct hardness of bonds; and spin tests assure adequate strength.

Upon the understanding of the wheel fabrication procedure, it demonstrates that the position of all abrasive particles are neither uniform nor random distributed in the wheel body, but in fact dominated by the packing procedure during its making. And the mechanical properties of the wheel would then affected by packing as well as the bond material property. Considering all these factors, it appears that when each wheel fabrication step is modeled physically, a virtual grinding wheel that resembles the real product could be achieved. And the virtual wheel model could be able to reflect the nature of a grinding wheel and cumulate all wheel properties. In following paragraphs, the virtual wheel model algorithm is described step by step, and its programming is carried out with MATLAB.

4.2. Mathematical Description of Virtual Wheel Modeling

The idea in the research will be to utilize currently matured mathematical methods to model each step of the wheel fabrication process, from raw material mixing to final wheel dressing. Not only the composition of wheel, such as grain size, grain shape, grain fraction, and bond fraction, but also the mechanics, and bond material diffusion during wheel packing and firing are considered. After dressing simulation, where both kinematics and kinetics are involved, the virtual wheel surface should bear resemblance with the real products in terms of static grain count, protrusion height, effective pore volume, and local wheel hardness. The results of this simulation are also intended to be applicable in industrial situations for design and optimization of wheel composition and fabrication processes.

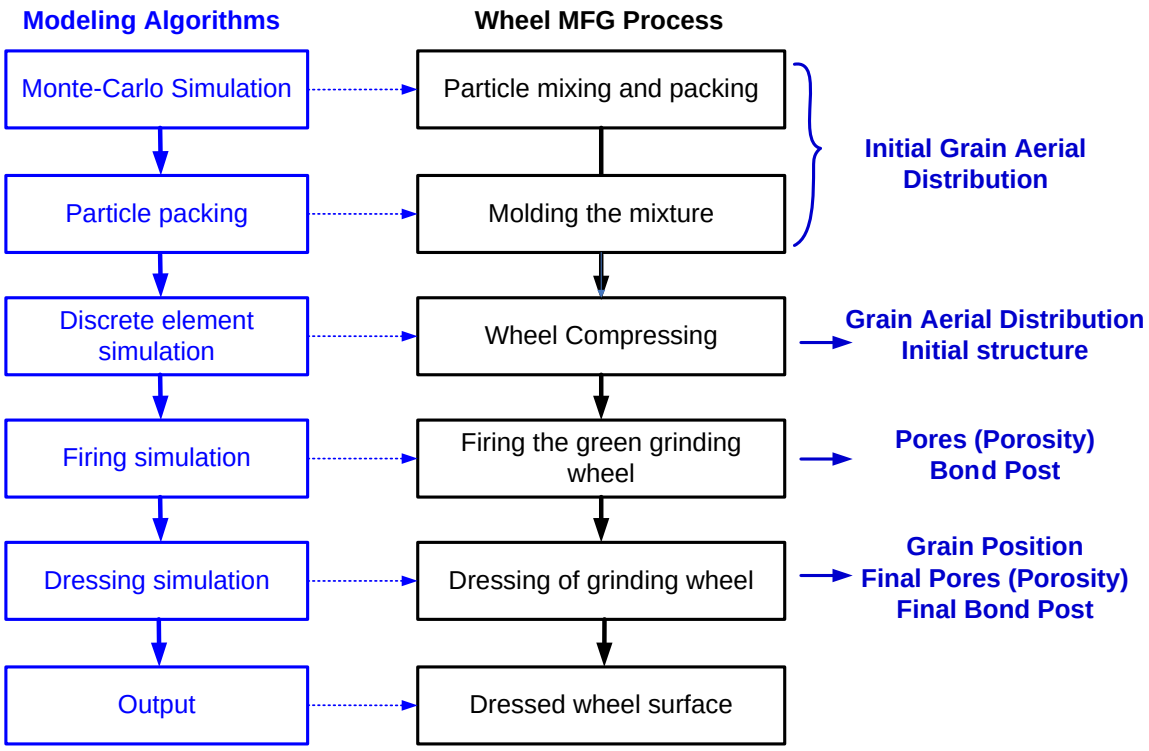

Figure 26 Wheel model methodology.

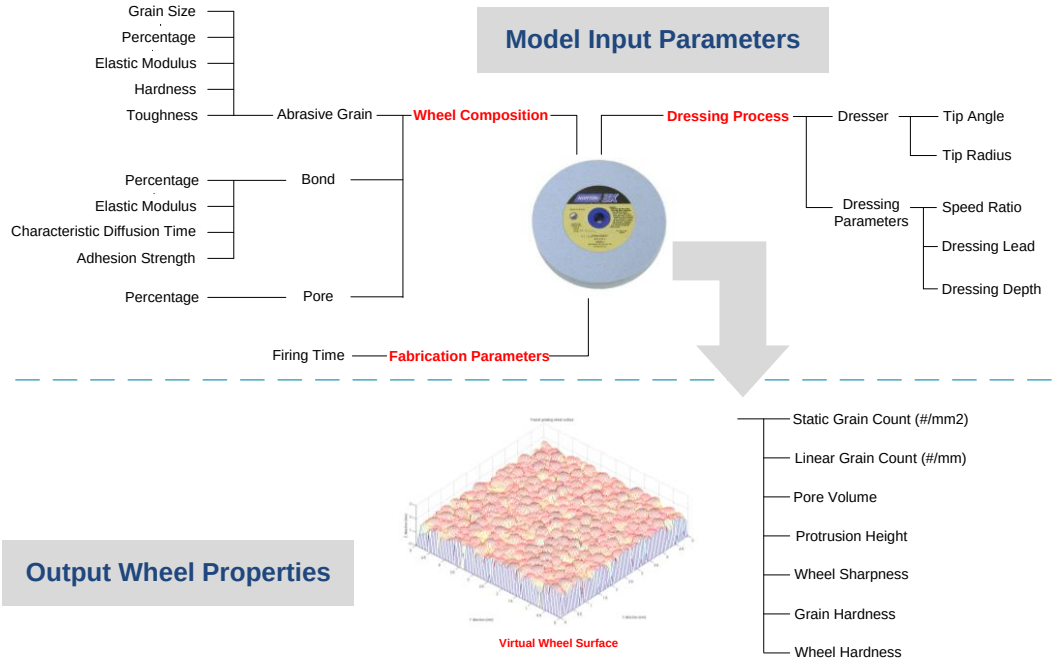

Figure 27 Input parameters and output measures for grinding wheel modeling

Considering the extensive application and straightforward fabrication process compared with organic bonded wheel, the modeling of vitrified wheels is conducted in this paper. The notations used in the algorithm are as follow: the simulation sample volume is $\boldsymbol{V}$ mm^3; $\boldsymbol{f_b}$ is the bond fraction; $\boldsymbol{f_g}$ is the grain fraction; $\boldsymbol{N}$ is the total number of grains; i (={1,2,…,N}) is grain index; $\boldsymbol{R_{gi}}$ is the radius of the $\boldsymbol{i^{th}}$ grain; $\boldsymbol{R_{pi}}$ is the radius of the $\boldsymbol{i^{th}}$ particle surrounded by bond layer.

4.2.1. Particle Mixing and Packing

When all ingredients are measured and mixed, the extremely fine bond powders, usually several microns or even finer, adhere to the abrasive grains forming a uniform bond layer due to the addition of wetting agent. When the grit number of grains is specified, the equivalent diameter can be corresponded to the mesh size and the next finer mesh size. For example, the maximum diameter is determined using sieve 46 and the minimum diameter using the next fine sieve, namely, 54 [29]. Thus, the grain diameters comply with the normal distribution of $\boldsymbol{N}$(0.323, 0.01) as shown in Figure 28. And the particle size $\boldsymbol{R_{pi}}$ due to the adding of bond powder can be derived from the following equation.

$$R_{pi} = R_{gi} \cdot \left(1 + \frac{f_b}{f_g}\right)^{\frac{1}{3}} \tag{12}$$

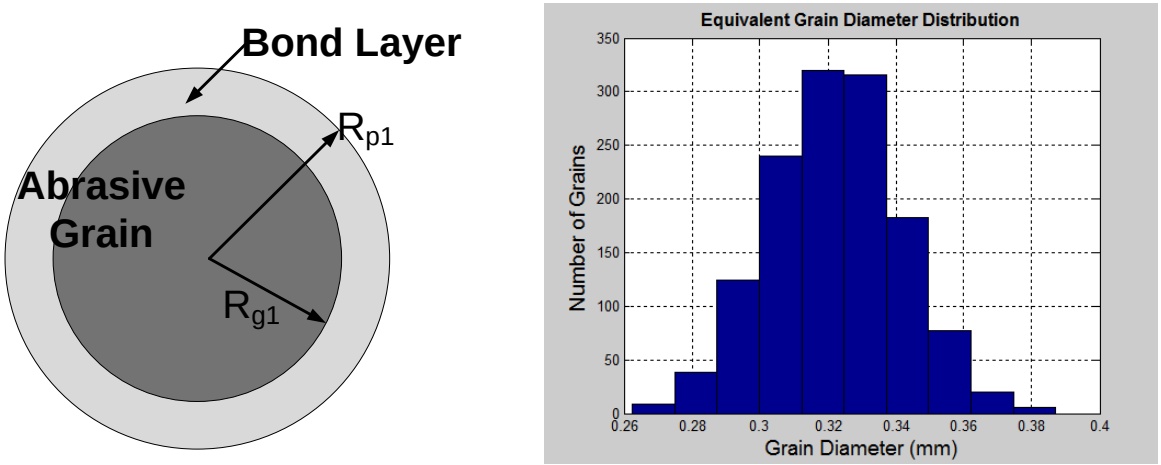

Figure 28 Grain diameter distribution (Grit 46) and particle structure in the mixture.

In the simulation, when the number of abrasive particles is determined, their diameters would comply with a normal distribution. The mean value of the distribution is consistent with the nominal diameter of the grit size, e.g. 0.323mm for grit-46 white aluminum oxide. The standard deviation is about 0.05. The algorithm to generate Gaussian distribution variables is described as below.

$$R_i = Rand * SIGMA + MU \ (0 < i \leq m) \quad (13)$$

where,

rand is a random number generated in between [0, 1].

SIGMA is the average.

MU is the standard derivation.

Given the wheel sample volume as x, y and z, the initial position of all particles is generated through Monte-Carlo method above the sample basal plain. The spatial position of all particles is random without contacting each other. If two particles are detected contact with each other, the successive grain would be regenerated till it does not contact with any previous particles. When pouring the mixture into the mould cavity, the bond powder surrounded particles move downward sequentially or along its neighboring particle surface if it is contacting with the neighboring particle. Considering the growth of a cluster of particles, a particle added to the cluster's surface can attain a stable packing position by first touching another particle, rolling to touch two particles, and rolling into a valley between three particles, as shown in Figure 29. The movement will stop till the particle contacts with the mould bottom or other three objects beneath its gravity center [49].

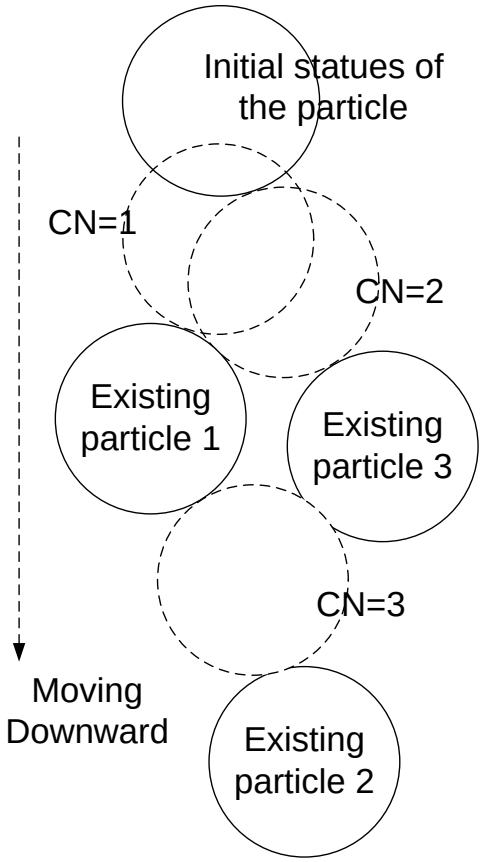

Figure 29 A particle movement under the gravitational force.

4.2.2. Compressing Algorithm after Packing

After all the grain and bond material are well mixed and poured into the mould cavity, the compressing process starts. During compressing, the position of the particles rearranges and the bond material outside the grain overlaps so that initial contact necks between two neighboring particles come into being. In order to simulate the movement of all the particles under applied external force and inter-particle force causing initial neck formation, discrete element method (DEM) is applied to the process.

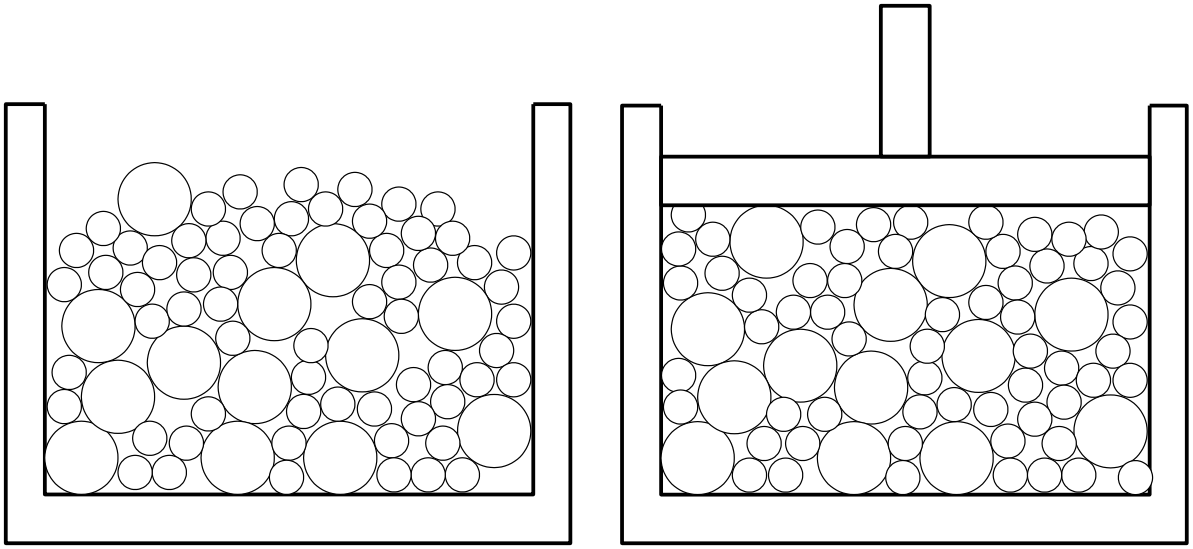

(a) Before compressing **(b) After compressing**

Figure 30 Initial status and particle rearrangement after compressing.

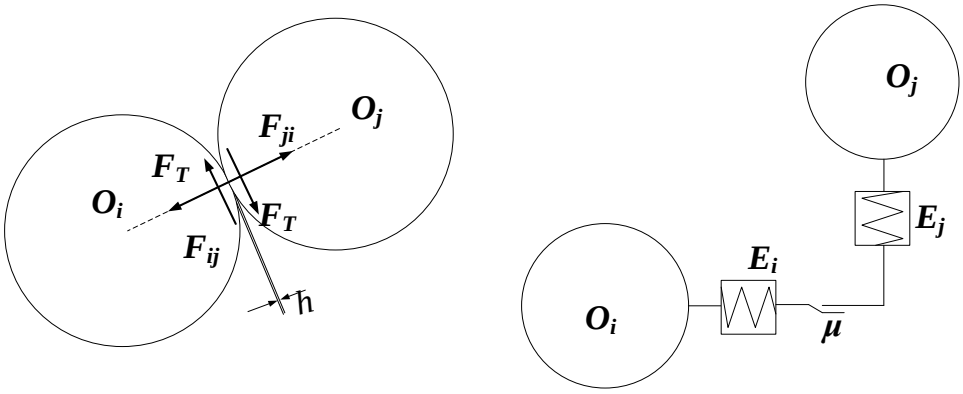

Figure 31 Schematic presentation for particle compressing.

Contrary to other methods, the discrete element method, in particular, treat each particle as a separate element. It enables the simulation of the dynamical behavior of granular material by direct introspection of physical effects of individual particles on the resulting behavior of static and flowing granular material without any global assumptions. Here, the granular material is

modeled as an abrasive grain with outside bond layers, while all dynamical parameters (position, velocity, etc.) and inter-particle contact forces between the particles are tracked during the simulation [50]. In order to simulate the movement of all the particles under applied external force, the interaction of two contacting particles should be studied. The contact situation for two particles is shown in Figure 31, when there is relative motion between them.

The notations used in the algorithm are as follow: the engagement depth of two contacting particles is $\boldsymbol{h}$; the radii of the two particles are $\boldsymbol{r_i}$ and $\boldsymbol{r_j}$, respectively; the displacement and velocity of one particle are $\boldsymbol{u}$ and $\boldsymbol{v}$, respectively. The engagement depth $\boldsymbol{h}$ can be decomposed in to normal direction and tangential direction:

In normal direction:

$$h_N = u_{N1} - u_{N2} \tag{14}$$

In tangential direction:

$$h_T = u_{T1} - u_{T2} \tag{15}$$

The normal force acting on the ith particle by the jth particle is:

$$F_{ij} = \frac{4}{3} \cdot \frac{E_i \cdot E_j}{E_i \cdot \left(1 - v_j^2\right) + E_j \cdot \left(1 - v_i^2\right)} R_{ij} h_N - \gamma_N m_{ij} v_{n,ij} \tag{16}$$

Where,

$$m_{ij} = \frac{m_i \cdot m_j}{m_i + m_j} \tag{17}$$

$$R_{ij} = \frac{R_i \cdot R_j}{R_i + R_j} \tag{18}$$

$\boldsymbol{E_i}$ and $\boldsymbol{E_j}$ are elasticity modular, and $\boldsymbol{u_i}$ and $\boldsymbol{u_j}$ are Poisson's ratios, $\boldsymbol{\gamma_n}$ is the damping coefficient in the normal direction.

Then the equation above can be simplified as:

$$F_{ij} = \frac{4}{3} \cdot \frac{E_i \cdot E_j}{E_i \cdot \left(1-\upsilon_j^2\right)+E_j \cdot \left(1-\upsilon_i^2\right)} R_{ij} h_N - \gamma_N m_{ij} v_{n,ij} = k_{n1,ij} \cdot (u_{N1} - u_{N2}) - k_{n2,ij} \cdot (\dot{u}_{N1} - \dot{u}_{N2})$$

(19)

The friction force between particle i and particle j is:

$$F_{t,ij} = -\mu \cdot \left|F_{n,ij}\right| \quad (20)$$

Then the tangential force can be expressed as:

$$F_{t,ij} = -\mu \cdot k_{n1,ij} \cdot (u_{N1} - u_{N2}) + \mu \cdot k_{n2,ij} \cdot (\dot{u}_{N1} - \dot{u}_{N2}) \quad (21)$$

Then differential equation for the contact couple (ith particle and jth particle) can be depicted as the following differential equations (gravity force is not included here):

$$\dot{u}_{N1} = v_{N1} \quad (22)$$

$$\dot{u}_{T1} = v_{T1} \quad (23)$$

$$\dot{v}_{N1} = \frac{1}{m_i} \cdot F_{n,ij} = \frac{k_{n1,ij}}{m_i} \cdot (u_{N1} - u_{N2}) - \frac{k_{n2,ij}}{m_i} \cdot (v_{N1} - v_{N2}) \quad (24)$$

$$\dot{v}_{T1} = \frac{1}{m_i} \cdot F_{t,ij} = -\frac{\mu \cdot k_{n1,ij}}{m_i} \cdot (u_{N1} - u_{N2}) + \frac{\mu \cdot k_{n2,ij}}{m_i} \cdot (v_{N1} - v_{N2}) \quad (25)$$

$$\dot{u}_{N2} = v_{N2} \quad (26)$$

$$\dot{u}_{T2} = v_{T2} \quad (27)$$

$$\dot{v}_{N2} = -\frac{1}{m_j} \cdot F_{n,ij} = \frac{k_{n1,ij}}{m_j} \cdot (u_{N1} - u_{N2}) - \frac{k_{n2,ij}}{m_j} \cdot (v_{N1} - v_{N2}) \quad (28)$$

$$\dot{v}_{T2} = -\frac{1}{m_j} \cdot F_{t,ij} = -\frac{\mu \cdot k_{n1,ij}}{m_j} \cdot (u_{N1} - u_{N2}) + \frac{\mu \cdot k_{n2,ij}}{m_j} \cdot (v_{N1} - v_{N2}) \quad (29)$$

Then the differential equation for the contact couple is expressed as below:

$$\begin{pmatrix} \dot{u}_{N1} \\ \dot{u}_{T1} \\ \dot{v}_{N1} \\ \dot{v}_{T1} \\ \dot{u}_{N2} \\ \dot{u}_{T2} \\ \dot{v}_{N2} \\ \dot{v}_{T2} \end{pmatrix} = \begin{pmatrix} 0 & 0 & 1 & 0 & 0 & 0 & 0 & 0 \\ 0 & 0 & 0 & 1 & 0 & 0 & 0 & 0 \\ \frac{k_{n1,ij}}{m_i} & 0 & \frac{k_{n2,ij}}{m_i} & 0 & \frac{k_{n1,ij}}{m_i} & 0 & \frac{k_{n2,ij}}{m_i} & 0 \\ \mu \cdot \frac{k_{n1,ij}}{m_i} & 0 & \mu \cdot \frac{k_{n2,ij}}{m_i} & 0 & \mu \cdot \frac{k_{n1,ij}}{m_i} & 0 & \mu \cdot \frac{k_{n2,ij}}{m_i} & 0 \\ 0 & 0 & 0 & 0 & 0 & 0 & 1 & 0 \\ 0 & 0 & 0 & 0 & 0 & 0 & 0 & 1 \\ \frac{k_{n1,ij}}{m_j} & 0 & \frac{k_{n2,ij}}{m_j} & 0 & \frac{k_{n1,ij}}{m_j} & 0 & \frac{k_{n2,ij}}{m_j} & 0 \\ \mu \cdot \frac{k_{n1,ij}}{m_j} & 0 & \mu \cdot \frac{k_{n2,ij}}{m_j} & 0 & \mu \cdot \frac{k_{n1,ij}}{m_j} & 0 & \mu \cdot \frac{k_{n2,ij}}{m_j} & 0 \end{pmatrix} \begin{pmatrix} u_{N1} \\ u_{T1} \\ v_{N1} \\ v_{T1} \\ u_{N2} \\ u_{T2} \\ v_{N2} \\ v_{T2} \end{pmatrix} \tag{30}$$

The matrix can be represented as:

$$\dot{D} = K_{ij} \cdot D \tag{31}$$

For the entire contacting system, the differential equation is:

$$\dot{D} = K \cdot D \tag{32}$$

where,

$$D = \begin{pmatrix} u_{N1} \\ u_{T1} \\ v_{N1} \\ v_{T1} \\ u_{N2} \\ u_{T2} \\ v_{N2} \\ v_{T2} \end{pmatrix};\ K = \begin{bmatrix} 0 & K_{nm} & \cdot & \cdot & \cdot & \cdot \\ K_{mn} & 0 & \cdots & \cdot & \cdot & \cdot \\ \vdots & \cdot & \ddots & \cdot & K_{ij} & \vdots \\ \cdot & \cdot & \cdot & 0 & \cdot & \cdot \\ \cdot & \cdot & K_{ji} & \cdot & 0 & \cdot \\ \cdot & \cdot & \cdots & \cdot & \cdot & 0 \end{bmatrix} \tag{33}$$

In the stiffness matrix K, if the $\boldsymbol{p^{th}}$ particle and the $\boldsymbol{q^{th}}$ particle are not contacting, $\boldsymbol{K_{pq}}$=0.

Then the differential equation for the whole mixture system, when gravity is included, is:

$$\dot{D} = K \cdot D + G \tag{34}$$

Initial Conditions and Boundary Conditions

For initial condition:

$$D(0) = 0 \tag{35}$$

$$\dot{D}(0) = 0 \tag{36}$$

When the iteration starts, the position of the particles on the top layer in the system will start to move downward. For each time incremental ***ΔT***, the rearranged position for all particles is calculated. The displacement of the particles is also confined by the wheel sample boundary in the simulation. The iteration will stop when the particles on the top layer reach the expected position.

4.2.3. Firing Algorithm

After the “green” wheel is compressed and dried in a controlled atmosphere for several hours or a few days, it undergoes firing procedure in a kiln. Throughout the firing cycle of several days at around 2000 Fahrenheit, the friable “green” wheels are converted into tough, rigid tools capable of working the hardest materials. In the micro-level, the coalescence between two particles as well as the diffusion of bond powder on to the abrasive grain will be accomplished during firing. As firing going on, the bond material will keep on diffusing to the bond neck due to surface tension causing neck radius increase from a0 to a as indicated in Figure 32. The position of all grain particles are not changed in the simulation considering that no external force is applied to the wheel during firing in the kiln. In addition, the bond powder is still in the solid state during firing, which still confines the movement of all particles. The diffusion of bond material to the neck bridge will stop till the firing procedure ends or all bond material around the particle is transferred to the neck bridge. The neck that holds two immediate particles can be treated as a cylinder shape. Then, the parameters to characterize the particle contact couple after firing are the neck radius a, particle radius R_{p1}, R_{p2}, and the neck height h. The calculation of the neck radius after certain firing time T is given in Equation 42.

$$a = \frac{192}{\tau_s} \cdot T^{1/6} \cdot a_0 \tag{37}$$

where, τ_s is the characteristic diffusion time for the bond material [51].

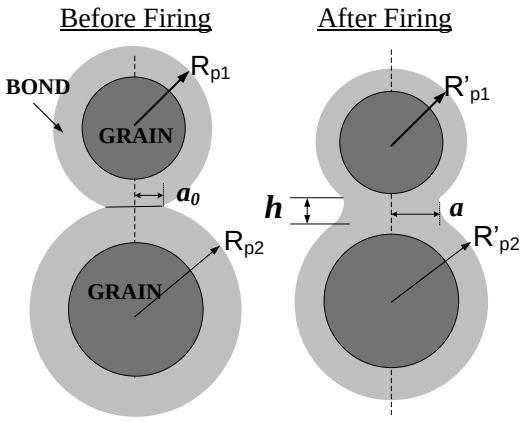

Figure 32 Formation and increase of bond neck during firing.

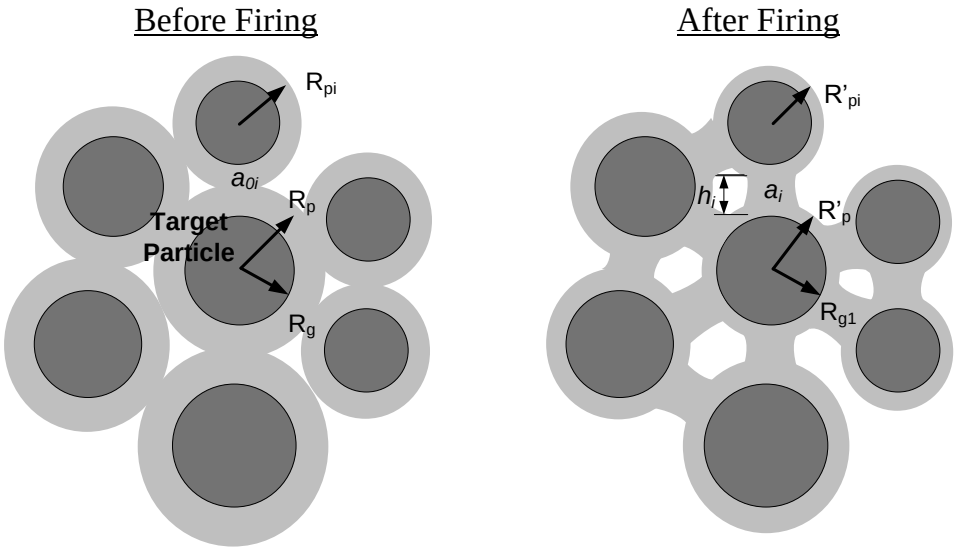

Figure 33 Neck bridge formation for multiple particles contact.

Figure 33 shows that how one particle forms neck bridges with multiple particles around it in the mixture. For the target particle in the center, mass conservation applies before and after firing. As the position of all particles doesn't change during firing, and the target particle contributes the formation of half of the neck bridge material. Then, following equation can be derived for the target particle for mass conservation.

$$\frac{4}{3}\cdot\pi\cdot R_p^3 = \frac{4}{3}\cdot\pi\cdot R_p'^3 + \sum_{i=1}^{N}\pi\cdot a_i^2\cdot\left(\frac{1}{2}\cdot h_i\right) \quad (38)$$

where, hi can be calculated by the following equation:

$$h_i = \sqrt{R_p^2 - \left(\frac{a_{0i}}{2}\right)^2} - R_p^{'} \tag{39}$$

Integration of above two equations gives the following equation with the only variable Rp'.

$$\frac{4}{3} \cdot \pi \cdot R_p^3 = \frac{4}{3} \cdot \pi \cdot R_p^{'3} + \frac{1}{2} \cdot \sum_{i=1}^{N} \pi \cdot a_i^2 \cdot \left(\sqrt{R_p^2 - \left(\frac{a_{0i}}{2}\right)^2} - R_p^{'} \right) \tag{40}$$

4.2.4. Dressing Algorithm

After firing, the wheels are trimmed and finish to expected dimensions, tested and labeled, which will not affect the quality and cutting effectiveness of the wheel. The only step that would influence the wheel surface properties and capabilities is the dressing operation. Figure 34 demonstrates two active mechanisms in dressing of vitrified bonded grinding wheels from literatures. One mechanism is the inducing of cracks into the abrasive grits, their splintering and break-out from the bonding. The other is caused by high dressing normal forces that destroy bonding bridges and break out grits and grit particles [13].

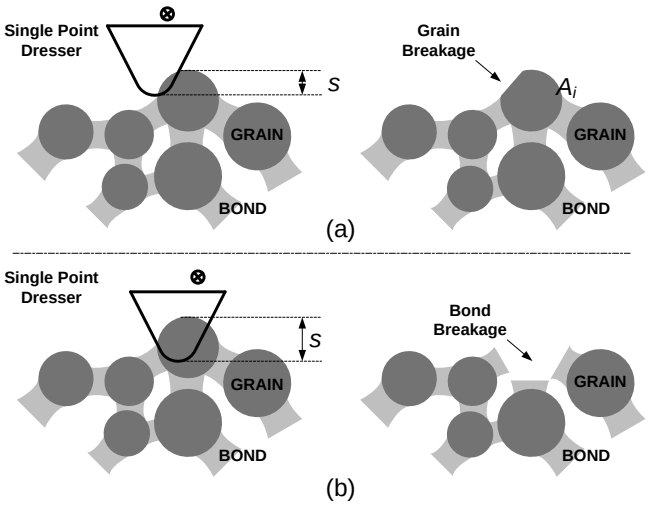

Figure 34 Dressing mechanisms: Grain breakage & Bond breakage.

For dressing simulation, the grain breakage and bond breakage can be determined through comparison of dressing force and the bonding force that holds the grain. If the dressing force is larger than the bonding force holding the grain, the grain will be pulled out; otherwise, the grain will splinter following the trace of the dresser. The dressing force for a dresser tip and grain engagement can be regarded as a linear function of the engagement depth, which is given as:

$$Dressing\_Force = K \times s \tag{41}$$

where, K is a constant related with grain properties.

And the bonding force for a grain can be regarded as the summation of the adhesion forces from the neck bridges attached to the grain. Then the bonding force for a single neck bridge can be obtained from the equation below.

$$\mathrm{Bonding\_Force} = \sum_{i=1}^{N} \mathrm{AS} \times \mathrm{A_i} \tag{42}$$

where, AS is the adhesion strength for the bond material; and Ai is the saturation area for the i^{th} bond bridge.

Till now, the methodology based on wheel fabrication process analysis has been presented to simulate the 3D morphology of vitrified bonded grinding wheels, from which both microscopic topographic and mechanical characteristics of a dressed wheel can be obtained. This through-the-process model, apart from providing a digitalized and visualized tool for grinding process simulation, would also enable an efficient and effective method for abrasive products design and evaluation.

4.3. Model Verification and Analysis

As for vitrified grinding wheels, there would be numerous property parameters to characterize their performance. And typically in the plant practice, the “density” in term of the porosity and the wheel matrix integrity in terms of the average bond post strength are two critical

index need to be well controlled. However, there are still a few other parameters which have significant impact on grinding process, and may not be measured in the manufacturing floor practices due to the complexity in the measurement. And the grinding wheel model enables the provision of those critical data as indicated below and further comparison with the experiment value.

- Static grain count.
- Grain protrusion height.
- Effective pore volume.
- Local wheel hardness (Bond post strength).

In this part, 6 simulations are carried out to compare the effect of grit size change on wheel property variation. The parameters are chosen as the constant grain and bond fraction such that the effect of grit number on wheel properties can be examined. For grit 46, the composition complies with the standard specification WA46L8V. The wheel parameters and dressing parameters are given in Table 2 and Table 3.

Grit Number	Avg. Grain Diameter (mm)	Grain Fraction	Bond Fraction
24	0.676	49%	10%
30	0.532	49%	10%
36	0.415	49%	10%
46 (WA46L8V)	0.323	49%	10%
54	0.273	49%	10%
60	0.233	49%	10%
Firing Time		20 Hours	
Characteristic Diffusion Time		290 Hours [51]	
Bonding Strength		~ 800 MPa [52]	

Table 2: Wheel parameters for simulation.

Wheel Diameter (mm)	250
Wheel Speed (mm/s)	20,000
Dresser Travel Speed (mm/s)	5
Dressing Depth (mm)	0.1
Dressing Lead (mm)	0.19625
Pass number	1

Table 3: Dressing parameters for simulation.

4.3.1. Digital Grinding Wheel Surface

In the simulation of wheel fabrication and preparation, the surface topography can be derived directly as a 3D texture. Figure 35 shows part (3mm*3mm) of the digital surface texture of WA46L8V under the specified dressing condition. For the kinematics simulation in Chapter 5, the wheel surface topography is stored in the computer as a matrix ***Z(m,n)***, where ***Z(m,n)***

equals to the height of the wheel surface point in the used coordinate system. The property of the wheel surface mesh point is stored with another matrix ***P(m,n)***. ***P(m,n)*** equals to the abrasive grain index or zero if that mesh point belongs to the bond material.

Therefore, for a specified wheel sample, the kinematic grain count, the protrusion height for all superficial abrasive particles, effective pore volume, and bond post strength can be derived from the virtual wheel structure.

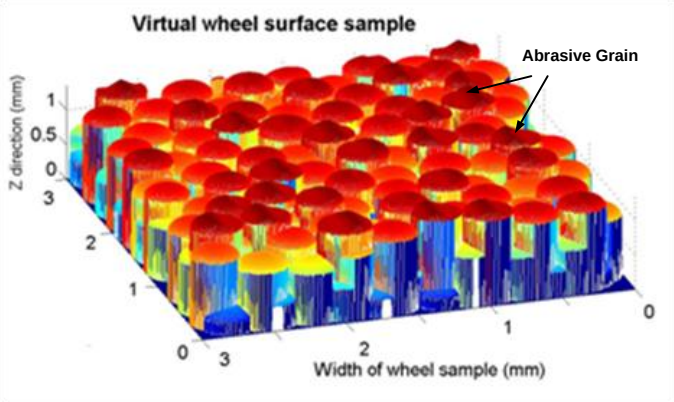

Figure 35 Surface for grit 46 wheel (WA46L8V).

4.3.2. Static Grain Count

The static grain count is the sum of all grains on the wheel surface per unit area, which belongs to the characteristic quantities of a grinding wheel [19]. Opposed is the kinematic grain count, which is the planar density of the grains actually interacting with the work to remove material. The kinematic grain count can be deduced by incorporating the process kinematics in the simulation. Figure 36 depicts the static grain count variation as the grit size increases. Each static grain count point is the average value of 5 sampling from 5 simulations; the error bar is given to indicate the variation of static grain count for the same wheels under the same dressing conditions. The simulation results can be seen to conform well to available reported experimental values for grit size 60, 54, and 46 [53; 54].

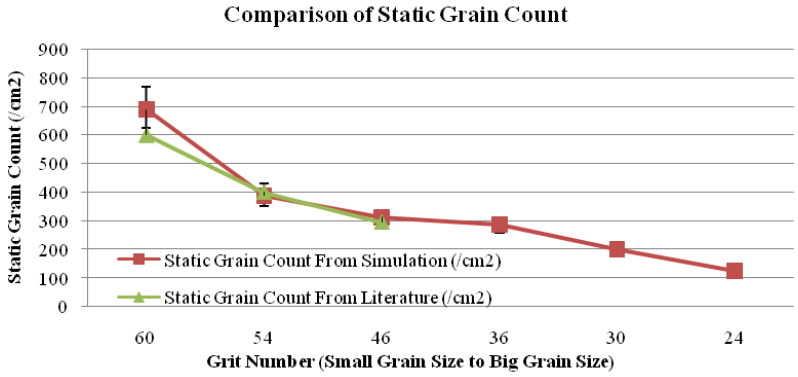

Figure 36 Comparison of static grain count.

4.3.3. Protrusion Height

The protrusion height, which is defined as the height of the grain tip from the bond surface, is an important parameter on which the roughness of the generated work surface and the wear of the wheel are dependent to a large extent. Inadequate protrusion of abrasive grains hampers the efficiency of material removal of grains while causing extra friction. The protrusion distribution also has a direct effect on the resultant workpiece surface, since an uneven protrusion height distribution increases the workpiece roughness [55]. For this reason, the information on the distribution of protrusion height facilitates selection of a wheel for a particular application, and for a selected dressing strategy to achieve a consistent wheel surface.

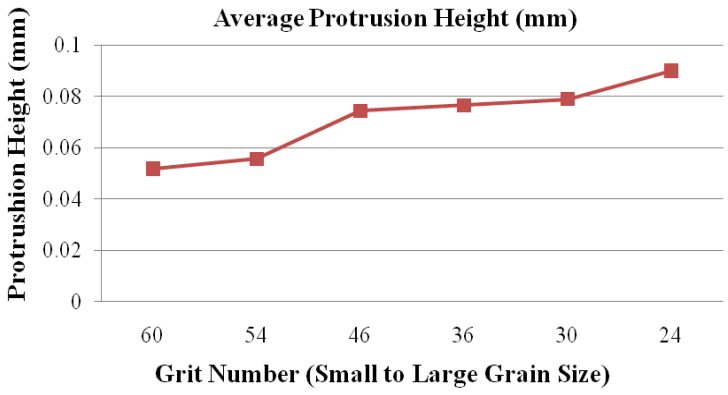

Figure 37 Variation of average protrusion height for various grit sizes

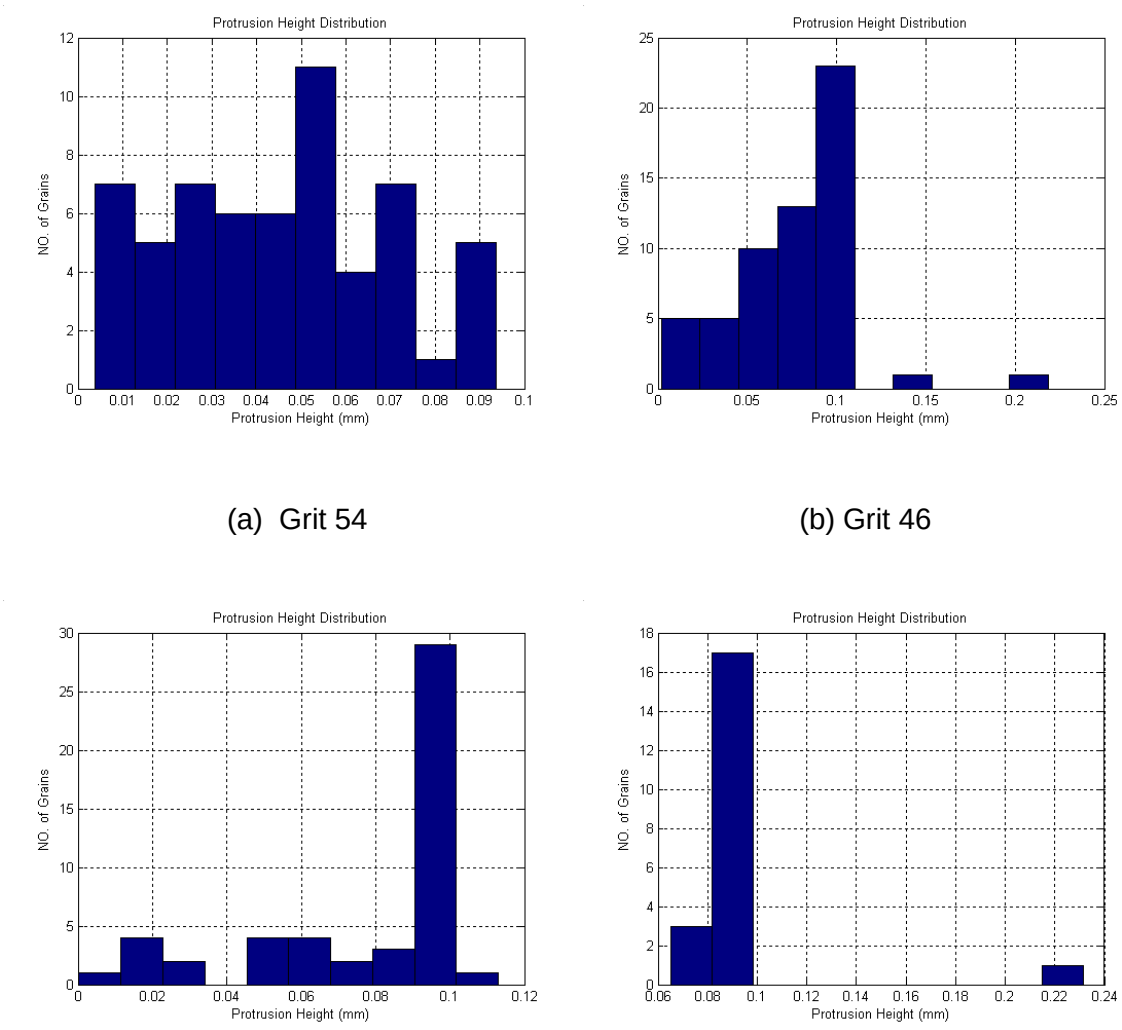

(a) Grit 54

(b) Grit 46

(c) Grit 36

(d) Grit 24

Figure 38 Protrusion height distribution for various grit sizes

Figure 37 depicts the variation of average protrusion height for different grit sizes under the same dressing condition. It indicates the average protrusion height decrease as the grit size reduces, and is independent of grain size within certain grit size range. This is in accordance with the results discovered in the literature [56]. And the in-depth analysis of protrusion height distribution in Figure 38 enables the discrimination of a 'good' dressing parameter from a 'bad' one. As grit size becomes smaller, the protrusion height distribution tends to be less

inconsistent, which suggests a finer dressing lead or more dressing passes are required for grit 46 or smaller grit wheels.

4.3.4. Effective Pore Volume

During grinding, the pores in front of grains provide channels for store lubrication and clearance for chips to escape from the wheel matrix [57]. In some high performance grinding applications, large pore volume is needed. Such applications include, but are not limited to, aerospace, high performance alloys, and parts with complex shapes. The effective pore volume, in conjunction with the protrusion height and the grinding kinematics, enables the prediction and control of grinding wheel loading. For an ideal 'non-loading' grinding process, the following principle can be deduced that the operational parameters should be selected so that the chip volume generated by a grain is smaller than the pore volume in front of it.

Understanding of effective pore volume in front of an abrasive grain as well as the statistics of all static grains helps predict the wheel loading. Figure 39 describes the calculation of the effective pore volume in front of a grain. And the change of average pore volume for various grit sizes is depicted in Figure 40, which provides a bench-mark for designing a 'non-loading' grinding process and determination of dressing duration.

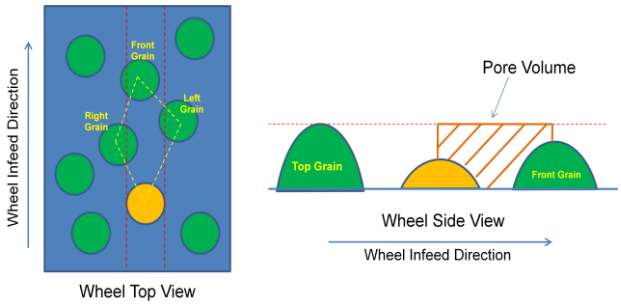

Figure 39 Schematic representation of pore volume calculation in front of a rain.

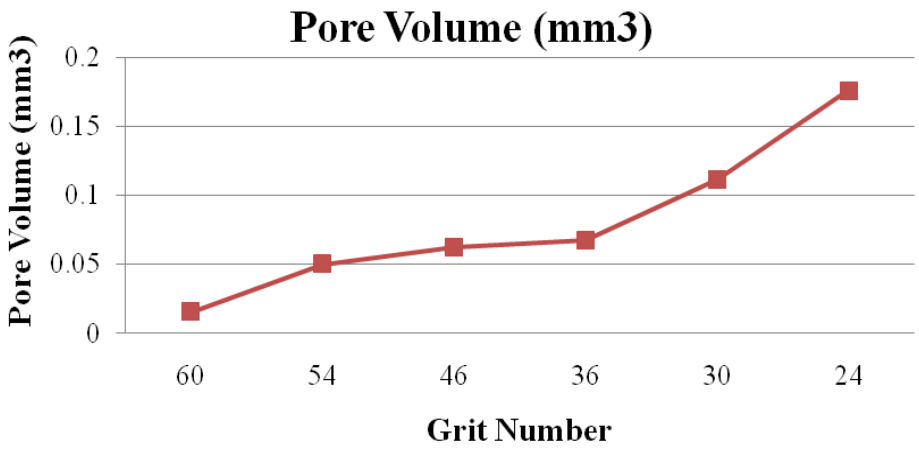

Figure 40 Variation of average pore volume for various grit sizes.

4.3.5. Local Wheel Hardness

Grinding wheel hardness is defined as the force causing the abrasive grains to break out of the bond composite. The productivity of grinding operations in industry is very sensitive to the wheel hardness [48]. Increased wheel hardness or bonding force would lead to a dramatically longer wheel life. Figure 41 shows the increase of the bonding force as the grit size increases from the simulation results. This can be explained that relatively more bond material is holding the individual abrasive grain as grit size becomes larger. The comparison of simulation results with literature data indicates that the model predicts the trend of bonding force change pretty well, although there is some difference [58]. The difference between them is mainly caused by the experimental measurement method used in the literature, as the experiment in fact measures the bonding force of a few adjacent grains instead of an individual grain. Figure 42 demonstrates the bonding force distribution for various grit sizes under the same dressing condition, which complies with the uniform distribution approximately.

The investigation of local wheel hardness enables the prediction of wheel consumption through comparing the cutting force applied on each single grain versus the localized grinding force. As the grain is broken away from the bond material, the wheel will lose its form causing

geometrical error. Therefore, the localized wheel hardness also presents a meaningful and quantitative basis for the prediction for wheel redressing frequency.

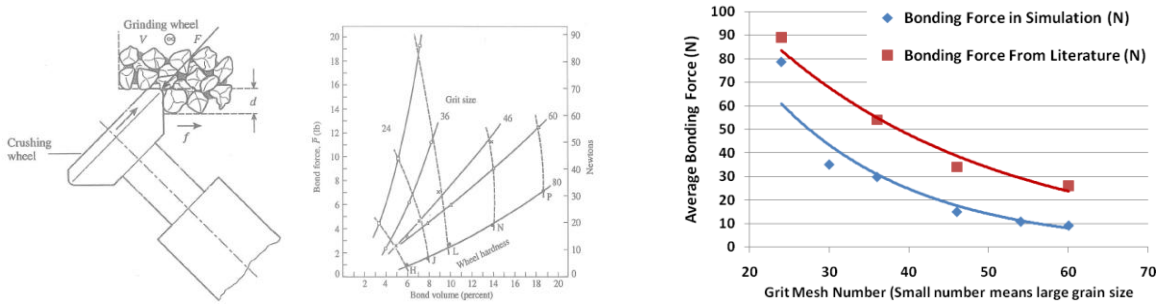

Figure 41 Average bonding force for various grit sizes.

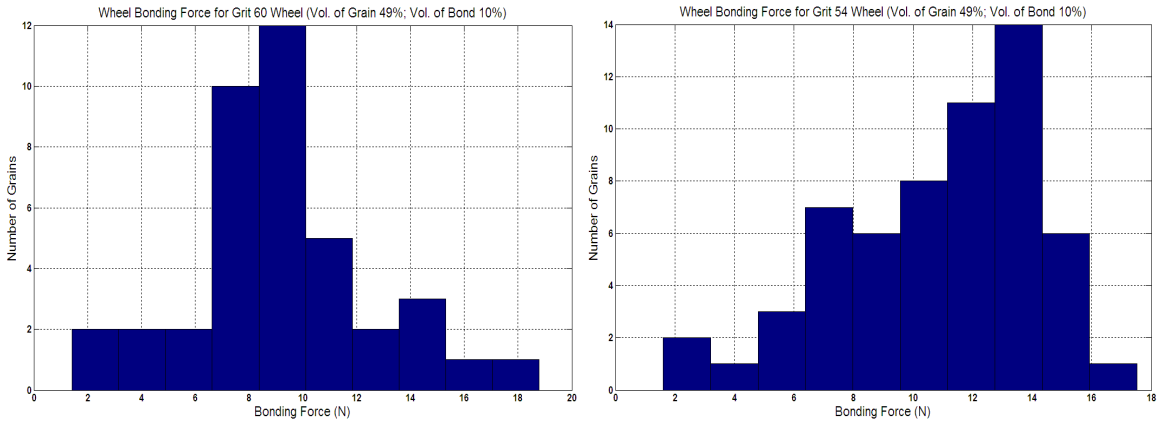

(a) Grit 60

(b) Grit 54

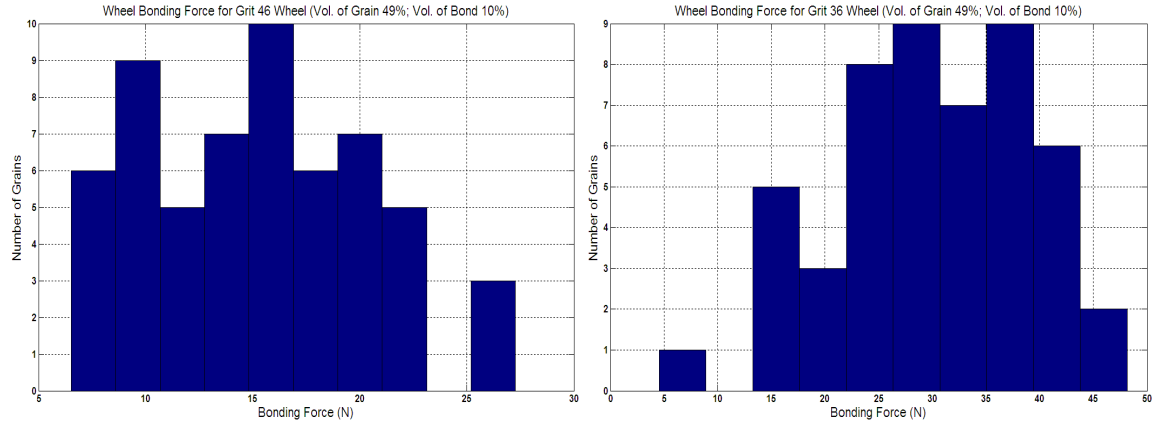

(c) Grit 46

(d) Grit 36

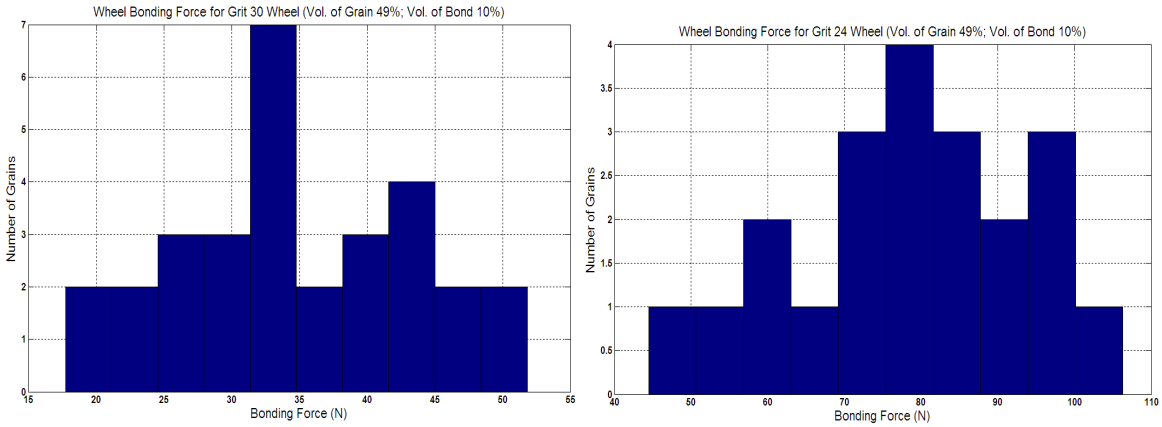

(e) Grit 30 (f) Grit 24

Figure 42 Bonding force distribution for various grit sizes

4.4. Summary

In this chapter, the grinding wheel modeling based on fabrication process analysis is discussed. Not only can it be used to model the vitrified wheels, but also it is applicable for organic bonded wheel and metal bonded wheels. The simulation results agree well with the available experimental data in terms of static grain count and bond post strength. In addition, the following general conclusions can be drawn through the simulations.

1. The distribution of protrusion height of a dressed wheel is a function of wheel composition and dressing parameters. A consistent protrusion height distribution is achievable via finer dressing lead.
2. The pore volume in front of a grain decreases as the grit size reduces.
3. The average bonding force decreases as the grit size declines, and the bonding force distribution on a dressed wheel surface complies with uniform distribution.

5. Microscopic Interaction Analysis

According to various mechanisms at the wheel-workpiece interface, different approaches are used toward the microscopic interaction analysis. For the abrasive – workpiece interface, finite element simulation for micro-cutting with ThirdWave AdvantEdge^{TM} is used; while an analytical model is developed for the loading model as it has a diverse mechanism compared with the abrasive/workpiece interface. The bond – workpiece, and grain – workpiece friction in the grinding with vitrified wheel are not prominent as the metal bonded wheel, therefore, they will be discussed but should not be considered within the research scope.

5.1. Abrasive – Workpiece Interface

For the abrasive/workpiece interface, the micro-cutting theory is applied for the single grain cutting process. In the study, finite element simulation is carried out to derive the specific force, side flow geometry, and chip formation that is required for the grinding process integration. In addition, the FEM simulation also helps understand the material removal mechanism of single abrasive grain, which may reveal the optimal grain geometry and process parameter for different functional requirements in grinding processes.

5.1.1. Introduction of Micro-machining

Micro-machining process is defined as the cutting process where the depth of cut is at the same order of cutting tool edge radius. In micro-machining process, the equivalent rake angle is usually negative, and the tool nose edge radius cannot be considered to be absolutely shape. Due to these 2 characteristics of micro-machining, it behaves in a different manner than conventional cutting in terms of the minimum chip thickness and the size effect [59]. The minimum chip thickness is defined as a critical depth of cut below which the material can only

be plastically deformed without any chip formation. And the size effect is defined as the reduction of specific cutting force as the depth of cut increase [60; 61; 62].

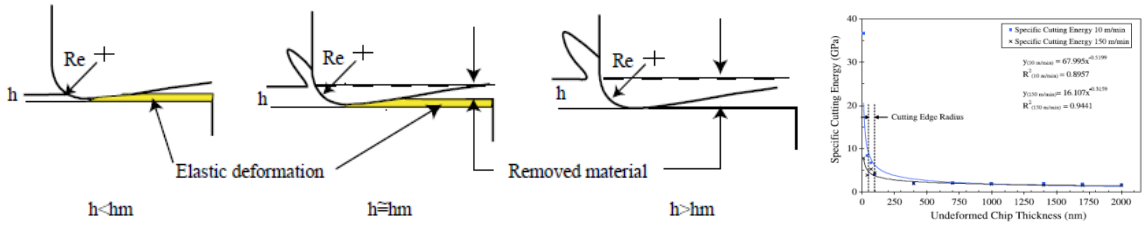

Figure 43 Micro-machining and size effect

5.1.2. Micro-machining in Grinding

Cutting and plowing are the most fundamental interactions in grinding, which modify the workpiece surface directly and dominate the material removal efficiency. Moreover, the chip generation in microscopic cutting also contributes to the chip/bond interface and chip/workpiece interface. Meanwhile, the surface modification by one grain influences the material removal of the successive grain. Therefore, mechanisms of cutting and plowing at microscopic level should be established for comprehensive understanding of grinding. Although a number of grinding experiments with a single abrasive grain were conducted, it is still quite intricate to establish the mechanisms in 3D due to the measurement difficulties of force, temperature and workpiece material deformation. The recent development of finite element models and packaged FEM software are capable to describe metal cutting processes explicitly. Therefore, there are great possibilities that finite element modeling can be applied to investigate the single grain material removal under a wide range of grinding conditions. This can clearly quantify the force (or energy) consumption, chip generation mechanism, as well as localized material deformation, which are difficult to acquire based on only the common sense of grinding and single grain test. In this research, the commercialized FEM software package AdvantEdge^{TM}, which incorporates the

thermo-mechanical properties of material, is employed for single grain material removal understanding.

In grinding, although the grain geometry may vary are irregular after breakage, an abrasive grain tip can still be considered to be an inverse cone shape [1]. Figure 44(a) demonstrates the shape of white aluminum oxide grits and their localized features. The deterministic parameters for an inverted cone include the nose radius r_n and the cone apex angle 2θ as in Figure 44(b). The nose radius and the apex angel typically reflect the sharpness of the grain and how aggressively the material can be removed.

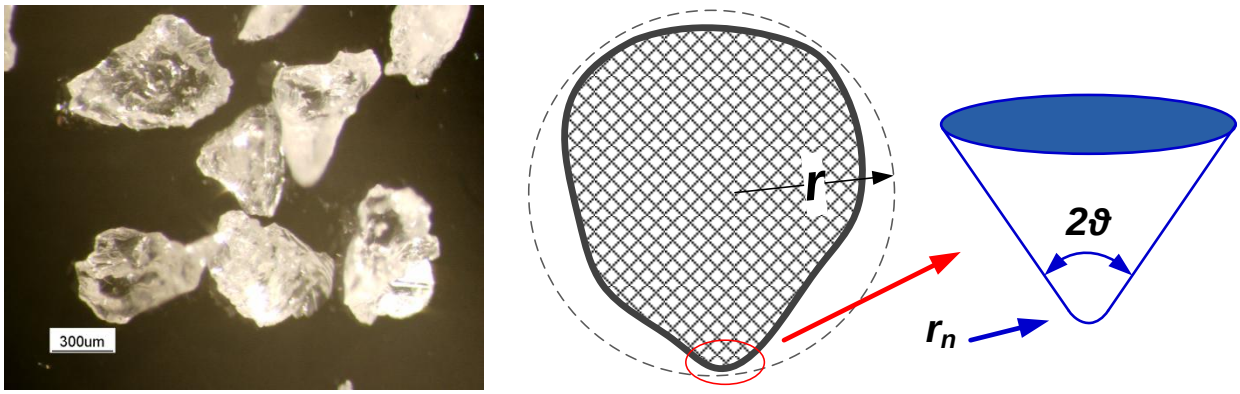

(a) White alumina: grit size 46 (b) Approximation of the cutting edge to a cone

Figure 44 Abrasive grains and effective cutting tip

During grinding, one abrasive grain seldom fully engaged with the workpiece, instead it will only contact partially with the workpiece. Therefore, the depth of cut may not be suitable to describe the engagement condition anymore. And the engagement cross-section area ***S*** is used to characterize the micro-cutting condition. Then, at any time instance ***t***, the force consumption can be expressed as a function grain-workpiece engagement cross-section area ***S(t)*** [63]. As the specific cutting force is no longer a constant according to micro cutting theory, hence the simulation should describe the single grain force as a function of grain-workpiece engagement cross-sectional area ***S***. In addition, the side flow formation for each single grain in cutting and

plowing are also need to be considered, as the side flow geometry will affect the material removal of the successive grains. The side flow shape can be considered as triangular, which is characterized by the width ***b*** and height ***h***. Apart from the side flow the rest of the material contacting with the abrasive grain should be removed in the form of chip. The chip volume generated during a time interval ***Δt*** can be derived for loading force calculation. Integration of the instantaneous chip generation for the entire grain-workpiece engagement duration will yield the chip generation volume. Through the FEM simulation, the force consumption, side flow geometry, and chip volume generation for each grain-workpiece contact couple can be deducted from following equations.

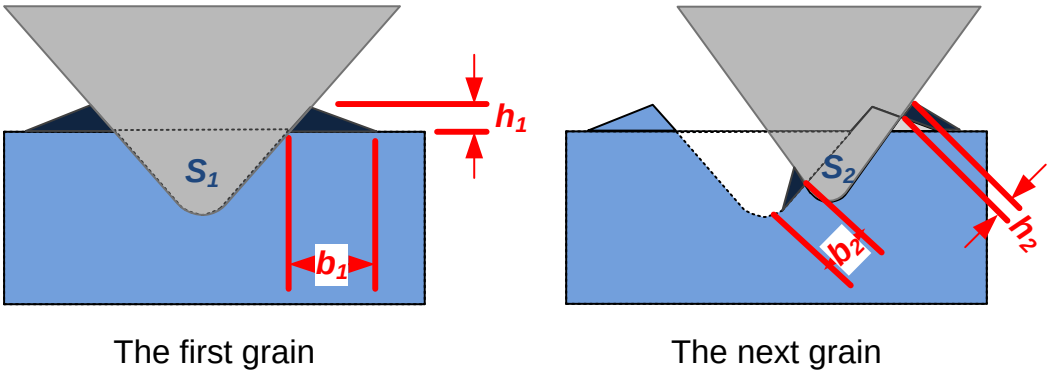

Figure 45 Single grain material removal in grinding

$$F_t = F(s) \tag{43}$$

$$b = b(s) \tag{44}$$

$$h = h(s) \tag{45}$$

$$V_{chip} = S - b(s) \times h(s) \tag{46}$$

5.1.3. FEM Simulation of Micro-machining

In recent years, finite element method has become the major tool for cutting process simulation. Using FEM for cutting process simulation mainly involves the material constitutive

modeling, chip formation and separation criteria, and workpiece re-mesh at each iteration step. Compared with other material removal analysis methods, e.g. analytical methods or indention tests, FEM, especially the AdvantEdge™, offers a higher accuracy and flexibility. The unique feature that distinguishes the FEM simulation with the analytical methods is the workpiece material constitutive model, which is developed specifically to describe the material's behavior under cutting conditions. The mechanical material properties take the strain hardening, strain rate dependency and thermal softening into consideration. The FEM simulation hence can provide both macro-output and micro-output, in terms of force, temperature, stress field, shear angle, and chip separation.

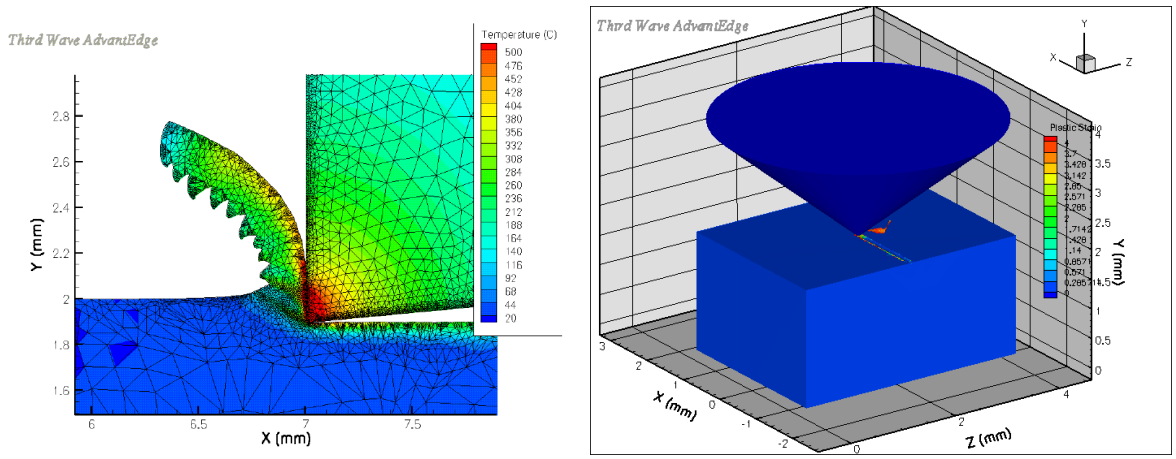

Figure 46 FEM simulation for 2D and 3D cutting process

5.1.4. Principle of FEM Cutting Simulation

For the FEM cutting simulation, the primary modules should cover at least, but not limited to material constitutive model, chip formation criterion, heat transfer model, and FEM computation algorithms. Among all the modules, the material constitutive model is of the most importance, through which the material properties at high strain rates, large strains, and short heating times are determined. And the material constitutive model is essential for prediction of cutting force and chips formation during cutting. For metallic material, the power law model is used in

AdvantEdge™ package, which is expressed as in Equation 53. $g(\varepsilon^p)$, $\Gamma(\dot{\varepsilon})$ and $\Theta(T)$ stand for the effect of strain (***ε***) hardening, strain rate sensitivity, and thermal (***T***) softening, respectively. And ***ε*** and ***T*** stand for the plastic strain and temperature. Detailed explanation of the power law constitutive model used in AdvantEdge™ can be found in its user manual [64]. In the simulation, the cutting tool is always considered to be perfectly rigid.

$$\sigma\left(\varepsilon^p, \varepsilon, \dot{T}\right) = g(\varepsilon^p) \cdot \Gamma(\dot{\varepsilon}) \cdot \Theta(T) \tag{47}$$

The strain hardening function $g(\varepsilon^p)$ for the power law is defined as:

$$g(\varepsilon^p) = \sigma_0 \cdot \left(1 + \frac{\varepsilon^p}{\varepsilon_0^p}\right)^{1/n}, if\ \varepsilon^p < \varepsilon_{cut}^p \tag{48}$$

$$g(\varepsilon^p) = \sigma_0 \cdot \left(1 + \frac{\varepsilon_{cut}^p}{\varepsilon_0^p}\right)^{1/n}, if\ \varepsilon^p \geq \varepsilon_{cut}^p \tag{49}$$

where σ_0 is the initial yield stress, ε^p is the plastic strain, ε_0^p is the reference plastic strain, ε_{cut}^p is the cutoff strain and n is the strain hardening exponent.

The strain rate sensitivity function $\Gamma(\dot{\varepsilon})$ for the power law is defined as:

$$\Gamma(\dot{\varepsilon}) = \left(1 + \frac{\dot{\varepsilon}}{\dot{\varepsilon}_0}\right)^{1/m_1}, if\ \dot{\varepsilon} \leq \dot{\varepsilon}_t \tag{50}$$

$$\Gamma(\dot{\varepsilon}) = \left(1 + \frac{\dot{\varepsilon}}{\dot{\varepsilon}_0}\right)^{1/m_1} \left(1 + \frac{\dot{\varepsilon}_t}{\dot{\varepsilon}_0}\right)^{(1/m_1 - 1/m_2)}, if\ \dot{\varepsilon} > \dot{\varepsilon}_t \tag{51}$$

Where $\dot{\varepsilon}$ is the strain rate, $\dot{\varepsilon}_0$ is the reference plastic strain rate, $\dot{\varepsilon}_t$ is the strain rate where the transition between low and high strain rate sensitivity occurs, m_1 is the low strain rate sensitivity coefficient, m_2 is the high strain rate sensitivity coefficient.

The thermal softening function $\Theta(T)$ for the power law is defined as:

$$\Theta(T) = (c_0 + c_1 T + c_2 T^2 + c_3 T^3 + c_4 T^4 + c_5 T^5), if\ T < T_{cut} \tag{52}$$

$$\Theta(T) = \Theta(T_{cut}) - \frac{T - T_{cut}}{T_{melt} - T_{cut}}, if\ T \geq T_{cut} \tag{53}$$

Where c_0 through c_5 are coefficient for the polynomial fit, T is the temperature, T_{cut} is the linear cutoff temperature and T is the melting temperature.

Figure 47 describes for given Compressive Split Hopkinson Pressure Bar tests (CSHB), how the strain, strain rate, and temperature would exhibit the nonlinear properties at different status[65]. Therefore, for any new developed material, as long as the CSHB experimental data is provided, all the coefficients in the constitutive model can be determined as the input for AdvantEdge™ simulation. In this chapter, the material constitutive mode parameters are well imbedded in the software already.

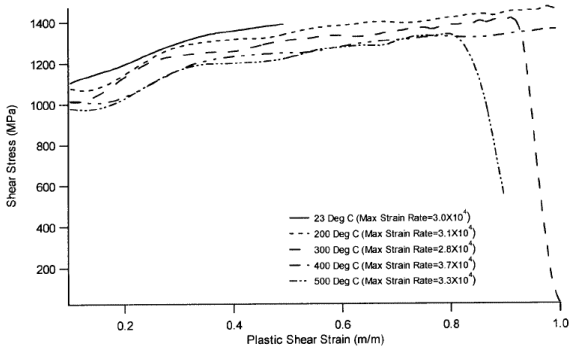

(a) Experimental data (D2 steel)

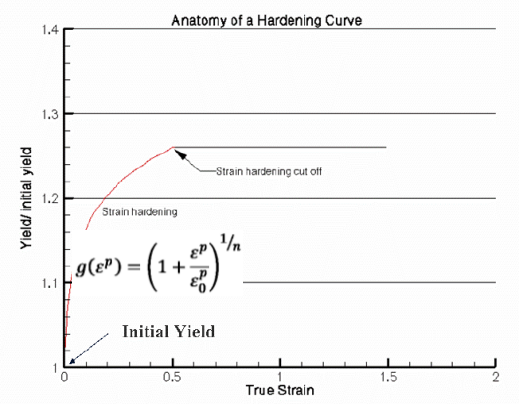

(b) Effect of strain

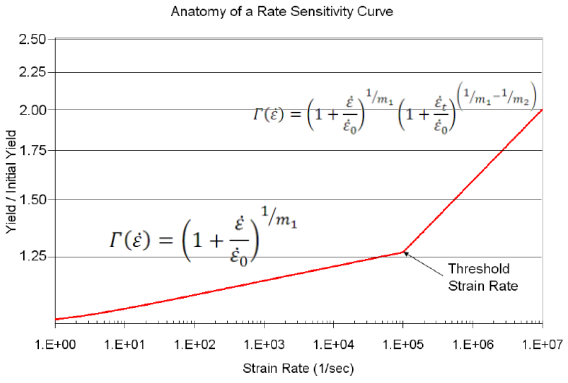

(c) Effect of strain rate

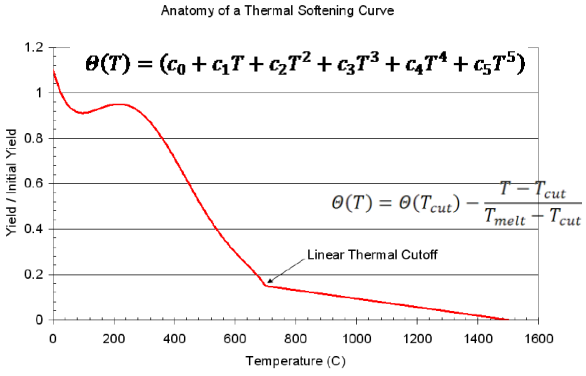

(d) Effect of temperature

Figure 47 Determination of constitutive model coefficients

The material separation or chip formation criterion is determined by material damage in AdvantEdge™, which is presented in Equation 54. The dimensionless cumulative damage D is expressed as the summation of ratio between instantaneous increment of strain and the instantaneous strain to failure. When the cumulative damage D exceeds a critical value (usually 1) given by the uniaxial tensile test [66], the material failure starts in the form of chip formation. The heat transfer model and FEM computation algorithm are well embedded into the FEM software, and will not be described in the dissertation in detail.

$$D = \sum_i \frac{\Delta \varepsilon_i^p}{\varepsilon_{f_i}^p} \leq 1 \tag{54}$$

The primary practice for validating the FEM cutting models is the evaluation of machining force and chip formation [61]. Comparison over a wide range of cutting conditions establishes the efficacy of the numerical-constitutive integration response. Once the models have been validated further analysis may be performed over a wider range of perspectives in terms of shear angle, Mises stress and plastic deformation, taking advantage of the numerical computation capability of FEM.

5.1.5. Efficacy Analysis of AdvantEdge Simulation

In order to compare with the experiments, the simulation parameters are chosen as specified in literature [67]. The abrasive grain is a conically shaped diamond grain with apex angle of 140◦ and nose radius of 0.06mm. The workpiece material is AISI 52100, and the single diamond grain is selected as a conical shape. The cutting speed is 30m/min; the depth of cut is 0.015mm, 0.02mm, 0.025mm, 0.03mm, and 0.035mm, respectively. Machining force, specific force, critical depth of cut, and chip formation are compare with the experiments to validate the software. In addition, the workpiece material stress field in the cutting zone, which is hardly obtained in experiments, is investigated for the mechanism understanding.

5.1.5.1. Determination of the friction coefficient

In the simulations, grit-46 white aluminum oxide grit is selected due to its wide application in steel grinding. Although the shape of abrasive grain is difficult to classify geometrically as the grains are made from mill breakage, it still can be estimated by experiment that the most of chip formation processes in actual grinding can be approximated as cutting with cone or sphere [68]. In this study, the grain is considered as a cone with cone angle 2θ and tip nose radius r, as indicated in Figure 65. Point A is the tangency point between tip arc and cone generatrix. In this case, when depth of cut is below point A, the contact zone is ball. It is like cutting with ball-shape grain. When depth of cut is above point A, the cone and ball part are both involved in the cutting. For grit-46 alumina grain, average tip nose radius and cone angle is 0.032mm and 80°, respectively [68; 69]. The workpiece is considered as a rectangular block because the cutting speed is much higher than the feed speed. The direction of cutting speed is parallel to the top surface of workpiece, as shown in Figure 65. Series of simulations have been conducted from low to high speed, with depth of cut from 0.015mm, 0.02mm, 0.025mm, 0.03mm, and 0.035mm. The workpiece material is D2 steel in hardened statues, and the constitutive model as well as the damage model is discussed in previous section. The grain-workpiece interface friction coefficient which is required in the simulation is determined by a ball-on-the-disk rotation experiment under a dry condition, as indicated in Figure 48. The ratio between measured normal force and tangential force gives the average friction coefficient of aluminum oxide – D2 steel couple, which is about 0.3.

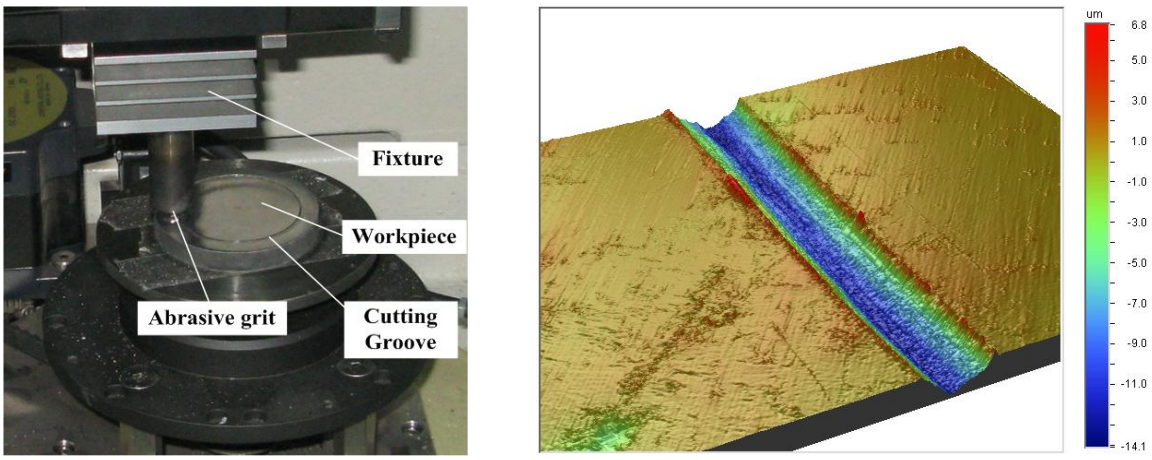

Figure 48 Experiment for friction coefficient determination

5.1.5.2. Machining Force and Specific Force.

The average steady state cutting and thrust forces at various DOC level are extracted and examined from the simulation results. A linear relationship can be obtained for the cutting force and material removal cross-section area in Figure 49, which is in correspondence with the experiment results [70]. To be able to compare the simulated cutting forces with the ones in literature the specific cutting forces were calculated. The calculation of specific cutting force is shown in Equation 55. And Figure 49 reveals that the specific cutting force agrees with the experiment data, and decreases with an increase in the cross-sectional engagement area. The nonlinear trend in the specific cutting force occurs when the undeformed chip thickness is about 0.015mm. This so-called “critical depth of cut” separates plowing and cutting modes. The values of the critical depth of cut are, therefore, effective for separating the cutting grains and plowing grains when the grain-workpiece engagement condition is determined from grinding kinematics simulation.

$$Specific\_cutting\_force = Cutting\_force/A \quad (55)$$

where, ***A*** is the cross-section area of the grain, as shown in Figure 49(a).

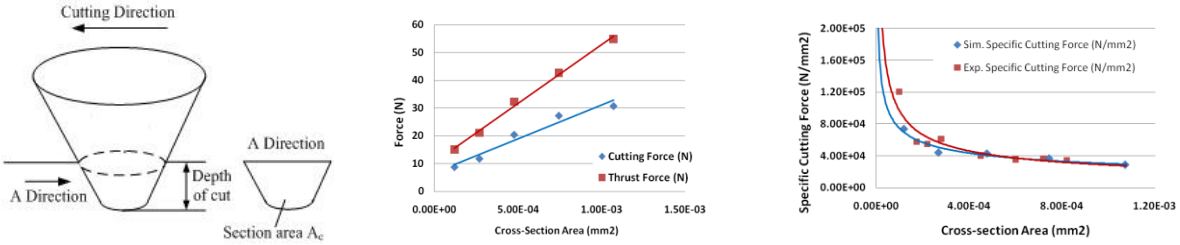

(a) Cross-section area calculation (b) Simulation data and comparison

Figure 49 Specific force calculation comparison of simulation and experiments

5.1.5.3. Chip Formation Comparison.

Although generated chip morphology and the chip thickness were not reported in literature [70], the material side flow cross-sectional area was plotted in the literature. In the simulation, the relationship between grain-workpiece engagement cross-sectional area and pile-up material cross-section area is analyzed to evaluate the chip formation. The geometry of side flow pile-up material is equivalent to a triangular shape, which can be characterized by the width d and height h. And the calculation of side flow cross-section area is indicated in Equation 50. The corresponding chip formation efficiency η can be calculated in Equation 51. As the grain-workpiece cross-section area increase, the area of pile-up material increases accordingly. An approximate linear relationship can be found for both simulation and experiment as in Figure 50.

$$Side\ flow\ cross\_section\ area = A_1 + A_2 = \frac{1}{2} \cdot (b_1 \cdot h_1 + b_2 \cdot h_2) \quad (56)$$

$$\eta = \frac{Ac - A_1 - A_2}{S} \quad (57)$$

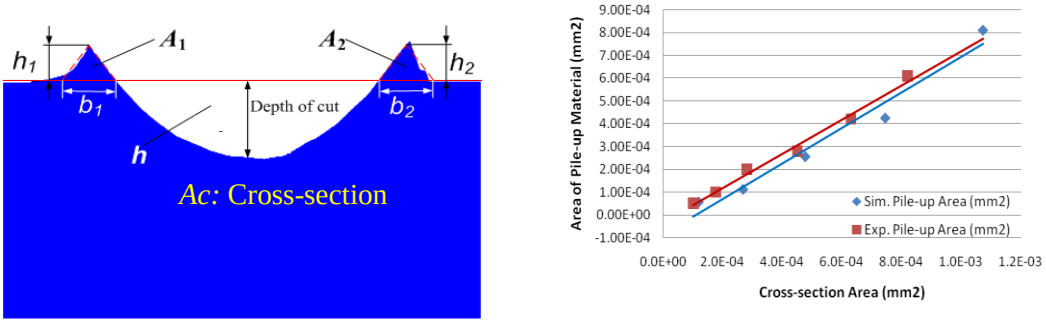

Figure 50 Measurement of pile-up material and comparison with experiments

The comparison of machining force and chip formation indicate a remarkable agreement of simulation results with the experiments, which testifies the efficacy of the software. Furthermore, the stress and plastic strain status of the workpiece material in and around the cutting zone are analyzed in order to reveal the mechanism that cannot be directly depicted from experiments.

5.2. Mechanism Study of Single Grain Micro-Machining

The micro-cutting simulation helps a sophisticated understanding of the process mechanism. For a single grain cutting process in Figure 51, the dominate factors include the cutting parameters in terms of cutting speed and depth of cut, grain geometry and material, workpiece material status, and the lubrication as well as coolant conditions. The expected output includes but not limited to the cutting force as a function of engagement cross-section area, the side flow width and height, and chip volume generated can be obtained, which has be stated in Chapter 2. To make the mechanism study more concrete, the simulations are carried out in such a way to reveal how following parameters affect the material removal in terms of the direct output and the derived output.

- Depth of cut ***h*** and cutting speed ***V***.
- Apex angle ***2θ*** of conical grain.
- Ferrous material with different hardness.

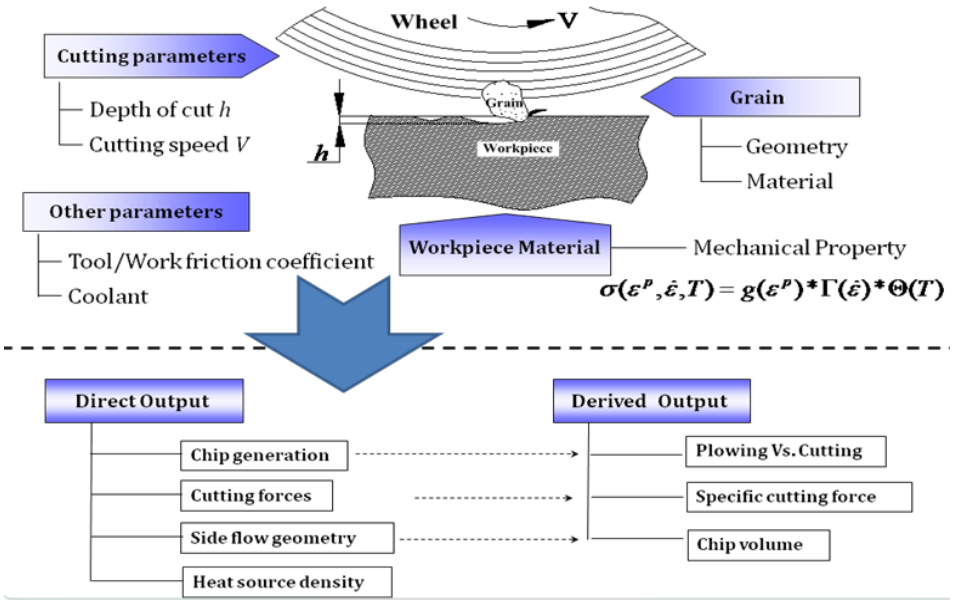

Figure 51 Input and output for micro-cutting simulation

In addition, the stress and strain status, which is difficult to obtain directly in experiments, can be quantified in the simulations in a straightforward manner. Therefore, the examination of the stress and strain in the cutting zone enables more sophisticated explanation of phenomena in grinding, too.

5.2.1. Effect of Micro-machining Parameters

The cutting parameters in terms of the depth of cut ***h*** and cutting speed ***v*** are 2 primary indexes to affect material removal process. Full factor experimental design of simulations is executed to examine the comprehensive impact of ***h*** and ***v***. The cutting speed ***v*** includes 4 levels from low to high: 1200m/min, 1800m/min, 4200m/min, and 5400m/min. The depth of cut ***h*** includes 0.006, 0.008mm, 0.010mm, 0.012mm, 0.032mm, 0.08mm, 0.12mm. While all the other parameters are fixed for all simulations, e.g. the conical aluminum oxide grain with 90 degree apex angle, D2 hardened workpiece material, and dry cutting.

5.2.1.1. Force and Specific Force

From the simulation results, when depth of cut is relative small compared to tip nose radius, cutting force hardly change at different cutting speed. As depth of cut continues to increase, cutting force increases sharply. At the conventional speed cutting, the cutting force increases with the increase of cutting speed. But cutting force decreases with the increase of cutting speed in the high speed cutting. It may be because of thermal softening of the material at high cutting speed enables material to be removed more easily, which yields smaller cutting force.

The specific cutting force ($\boldsymbol{SF_c}$) is an important indicator to evaluate the grinding process as well as the single grain cutting process. It may reflect the physical characteristic of workpiece materials in the cutting processes. Specific cutting force has the similar physical meaning with the specific energy. Figure 52 shows the specific cutting force with different cutting parameters. It is found that specific cutting force at small depth of cut is close to the specific melting energy of steels, 10.35J/mm^3, namely 10.35×10^3 N/mm^2. So the material flow occurs in the cutting zone, which is the main reason to form side flow. The specific cutting force decreases with the increase of depth of cut and it is approximately constant when the depth of cut is large compared to grain tip nose radius.

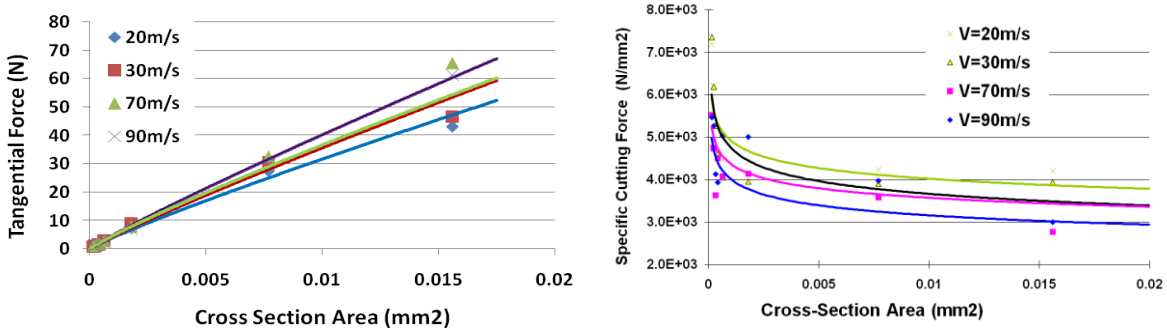

Figure 52 Effect of cutting parameters on specific cutting force

In addition, the plot of the specific cutting force also indicates the phenomenon of 'size effect' in Figure 52. A 'turning point' can be detected obviously when depth of cut is around 0.012mm or the engagement cross-section area of $4.55\times10^{-4}mm^2$ equivalently, which suggests the separation of cutting and plowing mode. During the plowing mode, the material will be mainly plastically deformed instead of forming chips; while for cutting, the majority of workpiece material will be taken away from the workpiece surface in the form of chip. This is also testified by the chip formation and side flow study.

5.2.1.2. Chip Formation

There are three types of cutting deformation in single grain cutting: chip, side burr and side flow, as shown in Figure 53. Continuous chips are obtained at small depth of cut. The chip is removed directly from the workpiece. With the increase of depth of cut, side burr which is hardened material with layer shape occurs. By analyzing the plastic strain, it is found that the material in the side burr area is experiencing severe deformation compared with side flow area, as shown in Figure 54. It can be inferred that the material area of side burr would be brittle and can be easily removed by the next cut.

At conventional speed cutting, 1200m/min and 1800m/min, severe side bur occurs when depth of cut is above 0.01mm; while in high speed cutting, 4200m/min and 5400m/min, it occurs when depth of cut is above 0.032mm. Take speed of 4200m/min as an example, the material deformation is chip formation and side flow at small depth of cut, as shown in Figure 53(a); while the material deformation is chip formation, side flow and side burr at larger depth of cut, as seen in Figure 53(b).

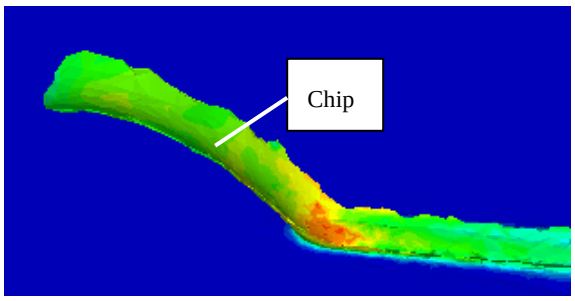

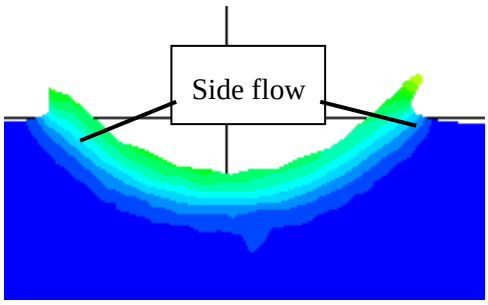

Chip and groove

Cross-section of groove

(a) V=4200m/min, depth of cut=0.01mm

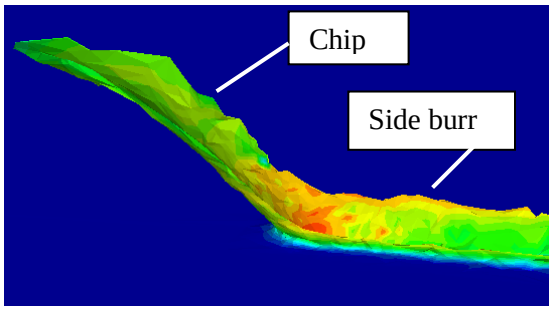

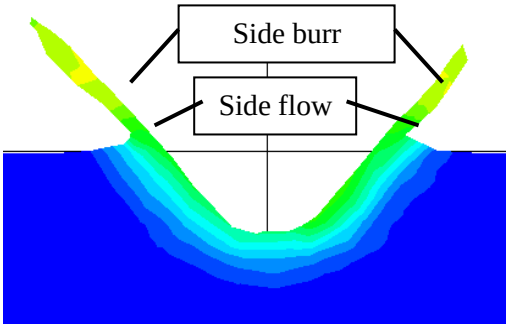

Chip and groove

Cross-section of groove

(b) V=4200m/min, depth of cut=0.008mm

Figure 53 Chip and side burr

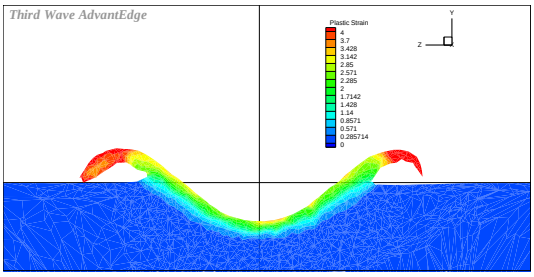

Figure 54 Plastic strain of side burr profile from simulation

Chip and side flow are the main types of cutting deformation in single grain cutting. Side flow is the pile-up of materials pushed to the groove edges by plastic deformation, and it does not

result in the removal of workpiece material. The material removal rate at different depth of cut and cutting speed is shown in Figure 55. The material removal rate η increases with increase of the depth of cut. And it increases as the cutting speed increases. As depth of cut continues to increase, material removal rate η seems to be constant value which means material removal rate does not increase anymore due to severe side flow.

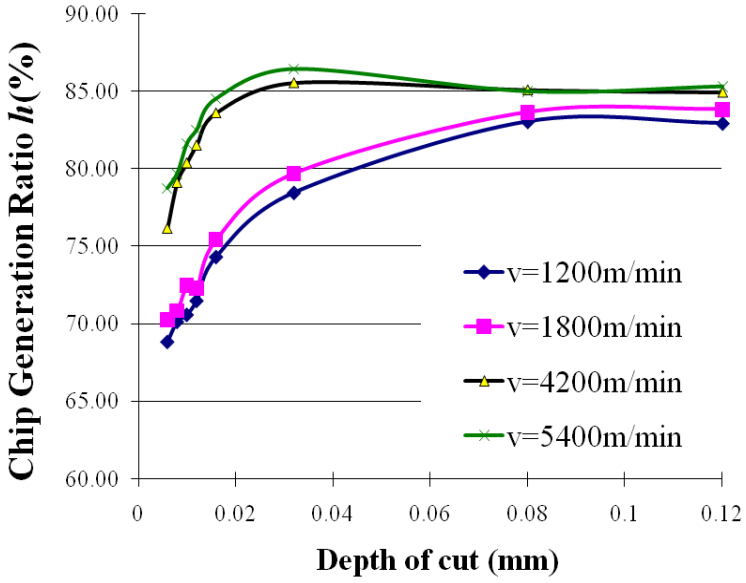

Figure 55 Effect of cutting parameters on material removal rate

5.2.2. Effect of Grain Geometry

The apex angle of conical grain is another critical parameter that affects the micro-cutting process. To examine its effect, the apex angle varies from 50, 60, 70, 80, 90, 100, 110, and 120 degree. The depth of cut is 0.012mm and cutting speed is 1200m/min, and all other input parameters are the same as before. Figure 57 describes the force and side flow variation as the apex angle increase. The cutting force barely changes while the normal force increases gradually. The examination of the side flow dimension indicates that for conical grains with the apex angle between 80~100 degree, there is a tendency of forming more side flow than removing the material. This could suggest the range for optimal grain nose apex angle. In

addition, the chip formation can be observed for all simulation cases, which implies that the chip formation may not be sensitive to cone angle.

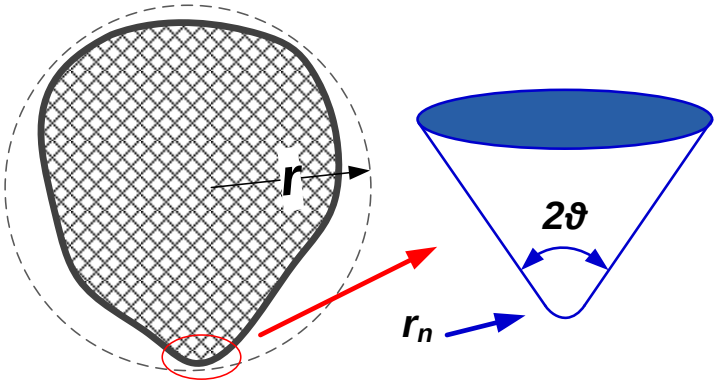

Figure 56. Representation of cone angle (2θ)

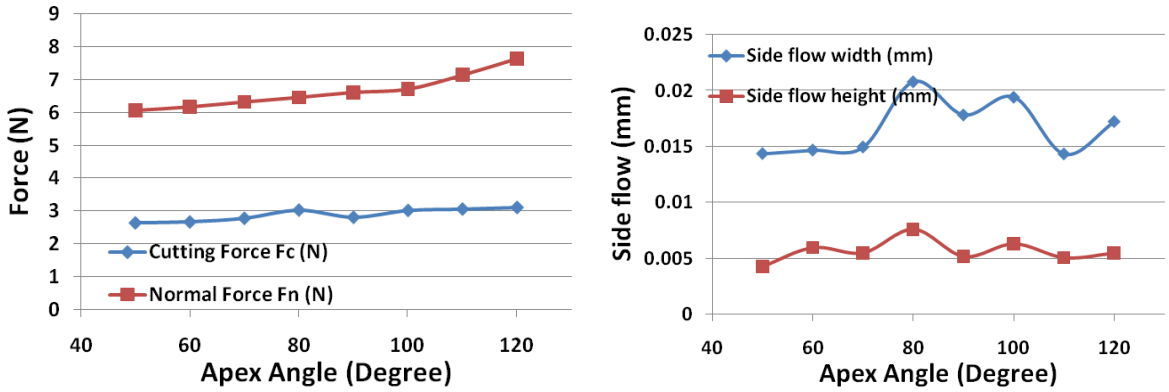

Figure 57 Micro-cutting force and side flow formation

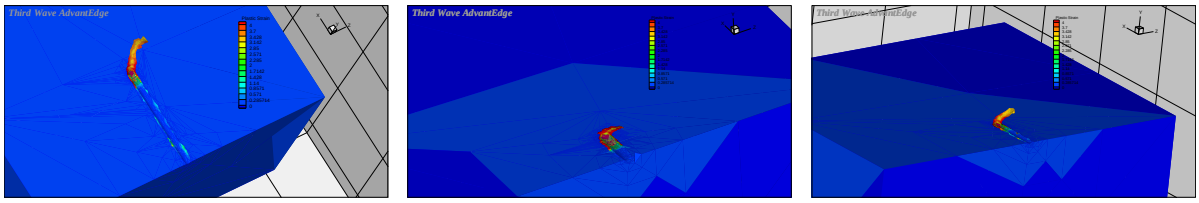

(a) 60 degree (b) 90 degree (c) 120 degree

Figure 58 Chip formation with various apex angles

5.2.3. Effect of Workpiece Material

The effect of workpiece material on the micro-cutting process is another intricate factor to study. To understand this, the ferrous material with different hardness are used in the simulation, including AISI1040(Bhn=149), AISI1045(Bhn=305), H13(Bhn=415), and D2(Bhn=615). Figure 59 describes the force and side flow variation as the material hardness increase. Both cutting force and normal force of AISI 1045 are higher than the rest of the materials. This unusual phenomenon maybe explained by the chip formation in Figure 60. It is observed that no obvious chip and severe side burr are formed for AISI 1045, causing material pile up in front of the cutting-edge. Therefore, the workpiece material will be mainly deformed plastically and excess force would be required to overcome the plastic deformation instead of shearing the material. For AISI 1040, side burr forms instead of chip during cutting, and severe side flow is observed compared with other material, which may cause the occurrence of loading more easily. From this perspective, this may well explain why soft materials are not suitable for grinding in nature.

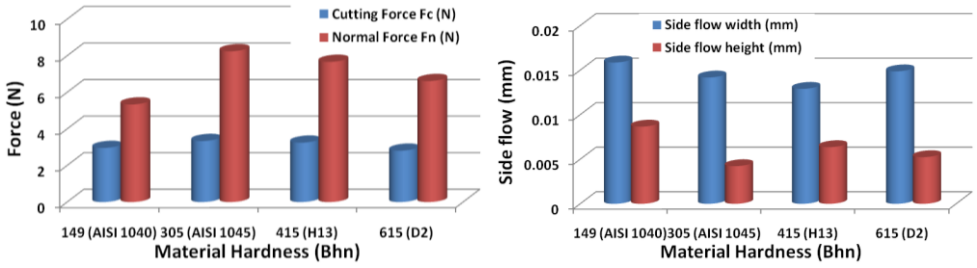

Figure 59 Micro-cutting force and side flow formation

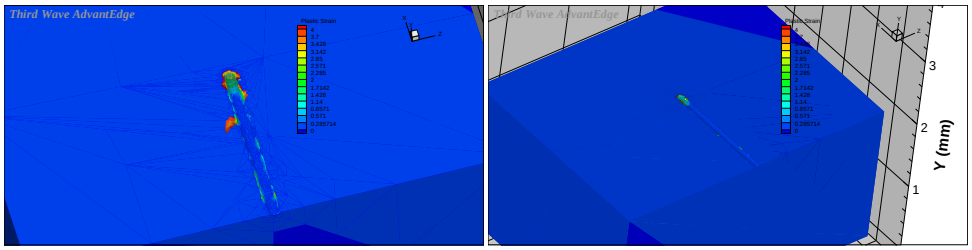

(a) AISI 1040 (b) AISI1045

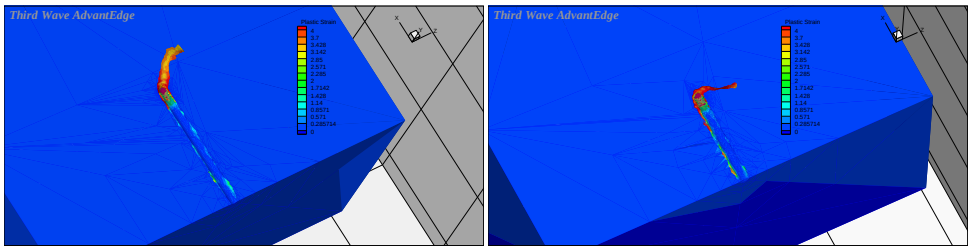

(c) H13 (d) D2

Figure 60 Chip formation for various workpiece materials

5.2.4. Workpiece Stress/Strain Field Analysis

Much effort is made to explain the mechanism of material removal in grinding, however, the material plastic flow and deformation mechanism is still not clear so far. The examination of the workpiece maximum pressure and Mises stress profile may open up a new vista for the understanding of material behavior and plowing occurrence. In the highlighted zone on the grain-workpiece interface, highest pressure and lowest Mises stress are achieved simultaneously. This phenomenon can be observed in all the simulations rather than occasionally. A careful examination and analysis of the stress status would help understand the material behavior in this area. Mises stress, which is known as the maximum distortion energy criterion, is often used to estimate the yield of ductile material in 3D. The Mises stress of material is defined as:

$$\sigma_v = \sqrt{\frac{(\sigma_1-\sigma_2)^2+(\sigma_1-\sigma_3)^2+(\sigma_2-\sigma_3)^2}{2}} \quad (58)$$

where, σ_1, σ_2, and σ_3 are the principle stresses in 3D.

And the maximum principle stress σ_{max} is defined as the maximum stress value of the principle stresses in 3D.

$$\sigma_{max} = \mathrm{MAX}(\sigma_1, \sigma_2, \sigma_3) \quad (59)$$

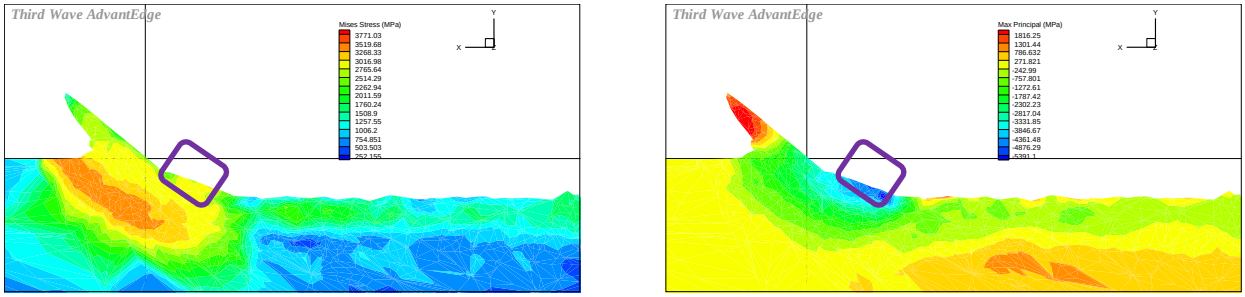

Figure 61 Pressure and Mises stress profile from simulation (DOC=0.020mm)

Therefore, it can be deduced that when the Mises stress achieves the maximum status, the differences of all 3 principle stress values are minimized. As one of the principles stresses reaches the maximum, the 3 principle stresses are all at their maximum status for the highlighted material compared with the material surrounding it. Then it can be inferred that the material in the highlighted area are experiencing most severe deformation than its immediate material, where most probably the material separation takes place and material plastic flow initiate. This finding suggests that the separation of chip from the matrix workpiece material initiated from some point on the rake face other than the tool nose tip. Even when the depth of cut exceeds the critical depth, the plowing effect still attains, which has been reported in the literatures [66; 71].

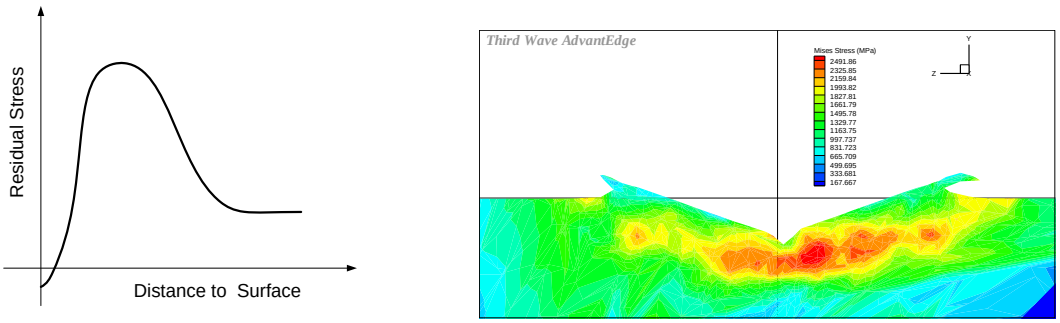

Figure 62. Typical residual stress curve in grinding and simulated Mises stress profile

The single grain cutting simulation provides another explicit explanation for the typical residual stress profile of grinding. For the single grain cutting, the maximum Mises stress can be

observed several microns beneath the grit cutting trace. This extreme stress would retain after the grain passing by, which contributes for the residual stress formation. This phenomenon explains why the maximum stress usually occurs beneath the workpiece surface rather than the workpiece surface [72]. From this perspective, the extreme stress in subsurface would be inherent with the negative rake angle cutting associated with grinding, and a proper selection of cutting parameter and grain geometry combination could minimize the residual stress without causing subsurface crack.

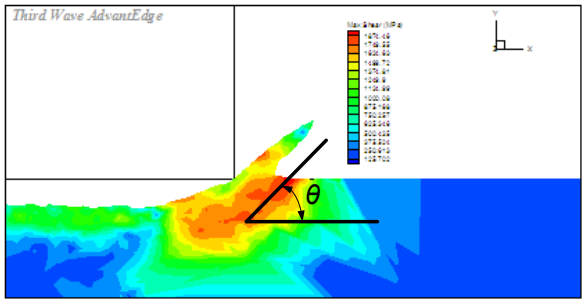

Figure 63 Shear angle measurement from simulation

The shear angle represents the orientation of the primary shear plane/zone in the work material during chip formation. This parameter can be derived from measurements of the deformed chip thickness and the tool rake angle. This is usually a tedious work, and involves a lot of measurement error. From the simulation, the maximum shear stress profile enables an efficient and accurate representation of the shear angle, as indicated in Figure 63.

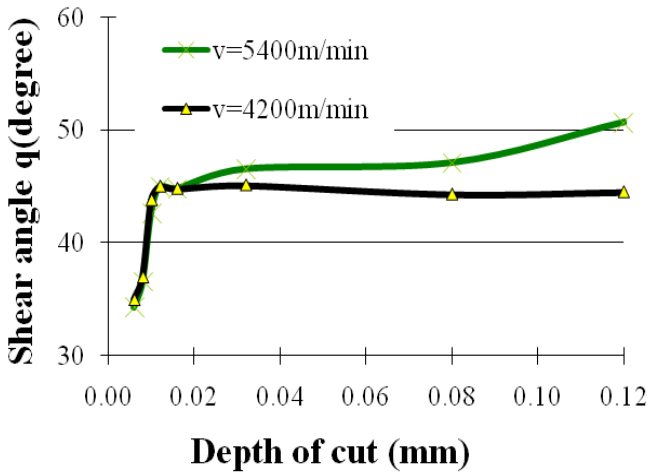

Figure 64 Effect of depth of cut and cutting speed on shear angle

The shear angles are derived from simulation results of the strain rate profile. It can be seen from Figure 64 that the shear angle increases with depth of cut up to 0.012mm for cutting speed of 5400m/min and 4200m/min. When depth of cut is larger than 0.016mm, the shear angle of cutting speed of 5400m/min is larger than that of cutting speed of 4200m/min. A consequence of the larger shear angle is a smaller cutting force. This can be seen in Figure 52 where, for depth of cut larger than 0.016mm, the cutting force of 5400m/min cutting speed is smaller than that of 4200m/min cutting speed.

5.3. Construction of Single Grain Micro-Machining Database

In order to establish the database to support the physics based simulation, simulations are examined focusing on how process parameters would affect the procedure with all other input parameters fixed. The cutting speed ***V*** and depth of cut ***h*** are 2 key variables, and all other parameters, e.g. grain parameters, cone angle, workpiece material are constant. In addition, as the abrasive particle seldom thoroughly contact with the workpiece, and depth of cut may not be suitable to describe the case in Figure 65. Therefore, the engagement cross-section area ***CSA*** is used to characterize the contact condition of grain – workpiece, and the regression equation

can be expressed in the exponential format in Equation 54. And the multi-variable data regression is necessary to derive the parameters ***K***, ***a***, and ***c***.

$$F_c, b\ or\ h = K \times CSA^{a} \times V^{c} \quad (60)$$

Where ***K*** is constant, indicating the factor affected by the grain, workpiece, and the cooling condition.

	CSA_1	……	CSA_j	……	CSA_m
V_1	$F_{1,1}$	……	……	……	$F_{1,m}$
……	……	……	$F_{i,j}$	……	
V_n	$F_{n,1}$	……	……	……	$F_{n,m}$

Table 4 Sample data for regression model

5.3.1. Multi-Variable Data Regression

In order to apply the linear regression model for data regression, logarithm is used to both sides of Equation 61, which is converted to multiple-regression linear model with 2 predictors. The general form for the linear regression model with 2 predictors is expressed in Equation 62.

$$log(F_c, b\ or\ h) = log(K) + a \times CSA + c \times V \quad (61)$$

$$y_i = a_0 + a_1 \times x_{i1} + a_2 \times x_{i2} + e_i \quad (62)$$

The variables e_1, e_2,…… e_n are independent random variables, with $E\{e_i\} = 0$ and $V\{e_i\} = \sigma^2, i = 1, \ldots\ldots n$. The principle of least squares calls for the minimization of the sum of square of residuals (SSE). Therefore, the regression Equation 63 can be reorganized into a matrix format.

$$\begin{bmatrix} y_1 \\ \vdots \\ y_{m\times n} \end{bmatrix} = [a_0 \quad a_1 \quad a_2] \cdot \begin{bmatrix} 1 & x_{11} & x_{12} \\ \vdots & \vdots & \vdots \\ 1 & x_{j1} & x_{j1} \\ \vdots & \vdots & \vdots \\ 1 & x_{m\times n\ 1} & x_{m\times n\ 2} \end{bmatrix} + \begin{bmatrix} e_1 \\ \vdots \\ e_{m\times n} \end{bmatrix} \quad (63)$$

In the general case it could have ***s*** predictors (***s>=1***). Let (***X***) denote an array of n rows and ***s+1*** columns, in which the first column consists of the value 1 in all entries and the second to (***s+1)***st columns consist of the values of the predictors $x_1, x_2 \ldots\ldots x_s$. (***X***) is called the predictor's matrix. Let ***y*** be an array of ***n*** rows and one column consisting of the values of the response. The linear regression model can be written in matrix notation as:

$$Y = (X)A + e \tag{64}$$

Where $A = [a_0 \quad \cdots \quad a_n]'$ is the vector of regression coefficients, and ***e*** is a vector of random residuals.

The sum of squares of residuals ***SSE*** can be written as:

$$SSE = (Y - (X)A)'(Y - (X)A) \tag{65}$$

Therefore, differentiating SSE partially with respect to the components of A, and equating the partial derivatives to 0, we obtain a set of linear equations in ***α***, namely.

$$(X)'(X)\alpha = (X)'Y \tag{66}$$

These linear equations are called the normal equations. ***α*** is the least-squares estimator LSE of ***A***.

Then the general formula of the least-squares regression coefficient vector ***α*** is given in matrix notation as by inversing Equation *:

$$\alpha = [(X)'(X)]^{-1}(X)'Y \tag{67}$$

In the dissertation, a MATLAB® program is developed based on the discussed algorithm for the regression coefficient vector calculation.

5.3.2. Regression of the Simulation Data

In the database, it provides the force and side flow geometry at various engagement cross-section areas under different cutting speed for a specified grain. The grain parameters and the cutting parameters are given in Table 5.

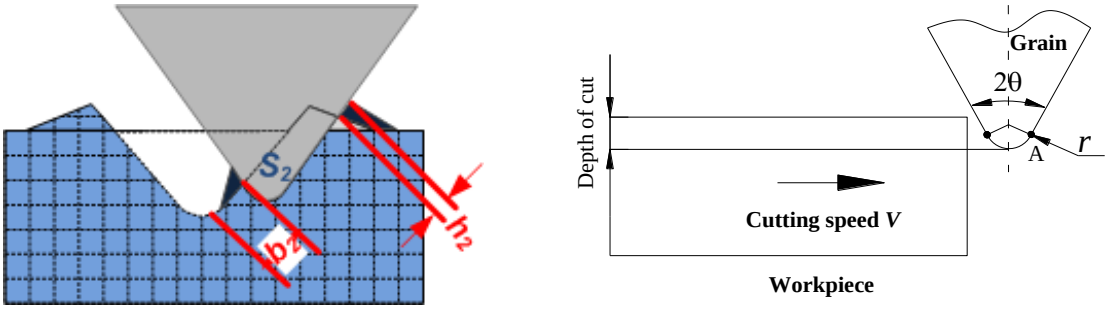

Figure 65 Representation of the grain-workpiece engagement cross-section area

Grain Material	46# Alumina (10~15% ZrO2)
Grain Shape	2θ = 80°; r=0.032mm
Workpiece material	D2 steel
Cutting speed (m/min)	1200, 1800, 4200, 5400
Depth of cut (mm)	0.006, 0.008, 0.01, 0.012, 0.032, 0.08, 0.12
Grinding coolant	No coolant

Table 5 Simulation data with different cutting speed and depth

The cutting force (F_c) at different cutting speed and engagement cross-section area is shown in Figure 66. For each specific cutting speed, data regression analysis can be carried out. And to formulate the database, the tangential force, as listed in Table 6, should be expressed as a function of the engagement cross-section area and the cutting speed as following. Therefore,

for the given grain – workpiece couple, the tangential force at any circumstance can be calculated based on the least square regression principle.

$$F_c = 76966 \times CSA^{0.6509} \times V^{-1.3782} \quad [68]$$

Speed (m/s)	Engagement Cross-Section Area (mm^2)							
	$1.52E^{-04}$	**$2.32E^{-04}$**	**$3.21E^{-04}$**	**$4.17E^{-04}$**	**$6.30E^{-04}$**	**$1.80E^{-03}$**	**$7.70E^{-03}$**	**$1.56E^{-02}$**
20	0.8403	1.100	1.163	1.876	2.564	7.436	27.54	43.13
30	0.8319	1.221	1.324	1.638	3.169	9.003	30.55	46.69
70	1.095	1.441	1.581	1.921	2.809	7.982	32.62	65.49
90	1.121	1.437	1.693	1.921	2.554	7.123	30.03	61.40
Remark	Tangential force (N) for various engagement cross-section area and speed.							

Table 6 Simulated tangential force with different cutting speed and engagement area

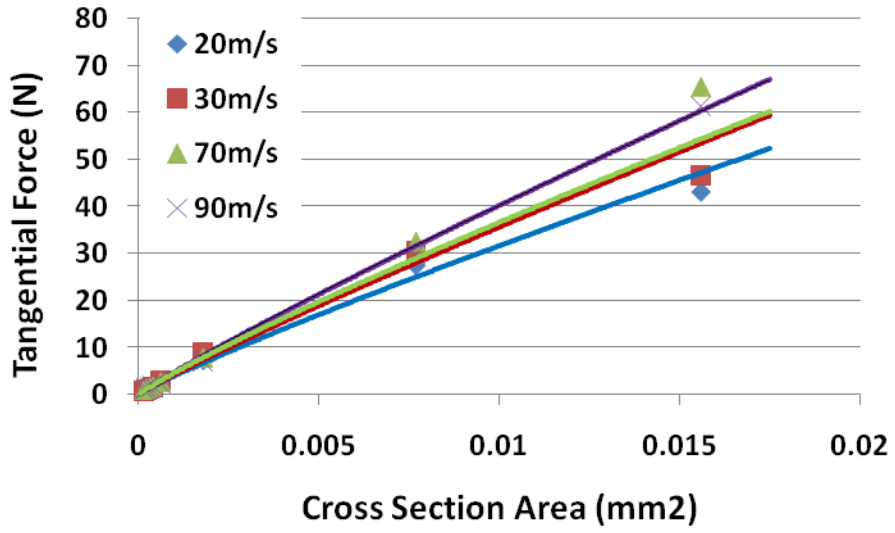

Figure 66 Effect of cutting parameters on cutting force

Similarly, the side flow geometry parameters ***b*** and ***h*** at different cutting speed and engagement cross-section area is shown in Figure 67. For each specific cutting speed, data regression analysis can be carried out. And to formulate the database, the tangential force, as

listed in Table 7 and Table 8, should be expressed as a function of the engagement cross-section area and the cutting speed as following. Therefore, for the given grain – workpiece couple, the side flow geometry at any circumstance can be calculated based on the regression equation at 95% confidence.

$$h = 1.2717 \times CSA^{0.2879} \times V^{-0.8743} \tag{69}$$

$$b = 3.3312 \times CSA^{0.2728} \times V^{-0.9398} \tag{70}$$

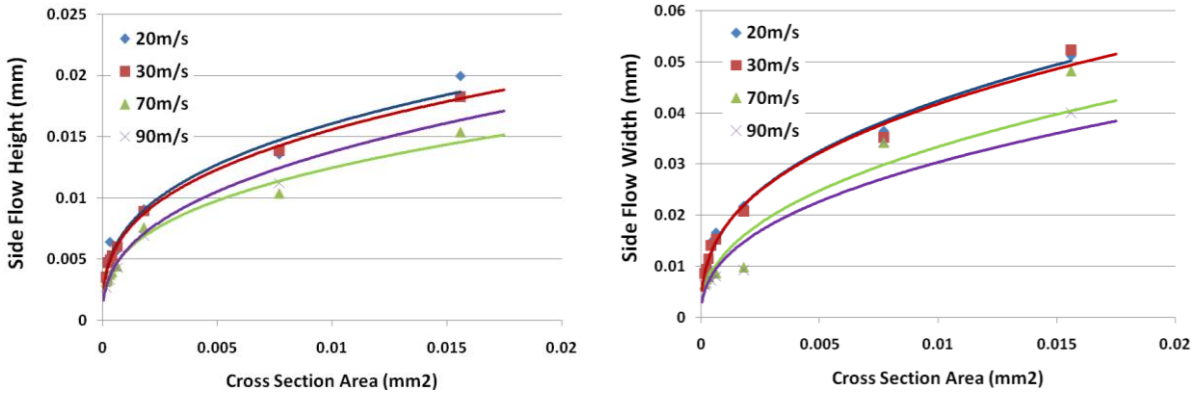

Figure 67 Simulated side flow height (*h*) and width (*b*)

Speed (m/s)	Engagement Cross-Section Area (mm^2)							
	$1.52E^{-04}$	**$2.32E^{-04}$**	**$3.21E^{-04}$**	**$4.17E^{-04}$**	**$6.30E^{-04}$**	**$1.80E^{-03}$**	**$7.70E^{-03}$**	**$1.56E^{-02}$**
20	0.003496	0.004832	0.006419	0.005100	0.005754	0.009091	0.01358	0.01996
30	0.003510	0.004700	0.004903	0.005248	0.005998	0.008901	0.01382	0.01827
70	0.003131	0.003267	0.003727	0.003927	0.004429	0.007583	0.01037	0.01539
90	0.002698	0.003534	0.003354	0.004309	0.004303	0.006927	0.01121	0.01823
Remark	Side flow height (***mm***) for various engagement cross-section area and speed.							

Table 7 Simulated side flow height with different cutting speed and engagement area

Speed (m/s)	Engagement Cross-Section Area (mm^2)							
	$1.52E^{-04}$	**$2.32E^{-04}$**	**$3.21E^{-04}$**	**$4.17E^{-04}$**	**$6.30E^{-04}$**	**$1.80E^{-03}$**	**$7.70E^{-03}$**	**$1.56E^{-02}$**
20	0.008992	0.009290	0.009447	0.01470	0.01660	0.02182	0.03649	0.05116
30	0.008580	0.009470	0.011473	0.01408	0.01530	0.02080	0.03527	0.05239
70	0.006593	0.007527	0.008026	0.00868	0.00867	0.00985	0.03423	0.04826
90	0.006334	0.006747	0.007997	0.00723	0.00801	0.00928	0.03441	0.04011
Remark	Side flow width (***mm***) for various engagement cross-section area and speed.							

Table 8 Simulated side flow width with different cutting speed and engagement area

5.4. Chip – Workpiece and Chip – Bond (Loading) Analysis

The loading phenomenon occurrence has been selected as a significant criterion in evaluating the grinding process [11]. The accumulated chip in the wheel pores is the major causative factor for this phenomenon, which creates additional steel-steel interact with a higher friction coefficient than grain-steel in the wheel-workpiece contact zone, as indicated in Figure 68. The extra friction couple will results in increased power consumption, causing more grinding wheel wear, higher temperature, and surface degradation. Since loading occurs whenever the grinding wheel structure is unable to cope with the quantity of chips produced, it is believed that using the wheels with porous structure will definitely alleviate the loading phenomenon [36].

For the frictional analysis, therefore, the loading force, which is the summation of chip/bond and chip/workpiece friction force, can described as a function of the accumulated chip volume and pore volume ratio. And the accumulated chip volume is derived from the kinematics simulation. While the bond/workpiece friction is prominent for the vitrified wheel grinding, as the brittle bond would be broken away when contacting with the workpiece.

$$F_{f,t} = \mu_{avg} \cdot p_{chip} \cdot \left({V_{chip}}/{V_{pore}} \right) \tag{71}$$

where,

$F_{f,t}$ is the tangential loading force.

μ_{avg} is the Coulomb Friction coefficient for steel-steel contact couple, which is chosen to be 0.5 in the research according to literature [73].

P_{chip} is associated with the flow stress of the chip. For hardened D2 steel, the chip is the same material as the workpiece matrix, and the flow stress is 800Mpa on average [74].

V_{chip} and V_{pore} are the accumulated chip volume and effective pore volume, respectively.

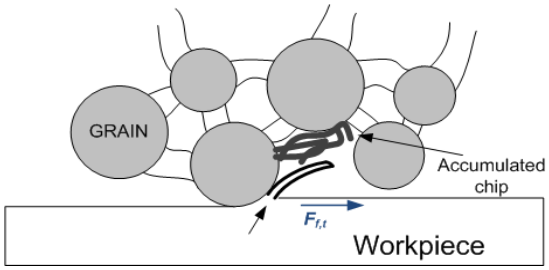

Figure 68 Occurrence of loading phenomenon

5.5. Grain-workpiece Friction and Bond-workpiece Friction

Figure 69 shows the grain-workpiece sliding occurrence when wear flat is developed on the grain tips. The area of wear flat gradually increases with grinding time and the rate of growth depends on the grain-workpiece combination, grinding parameters and the environment parameters. With the growth of wear flat, both the tangential and the normal forces increase, thus resulting in further increase in grinding energy consumption, grinding temperature and thermal damage [1]. The total wear flat area, which is the summation of wear flat area on each grain tip, is found to be in linear relationship with the grinding force [75]. Considering the proportional relationship between the grain-workpiece friction force and grain-workpiece contact area, Equation 16 shows the sliding force (power) consumption.

$$F_{G-W} = \mu_{G-W} \cdot \bar{p} \cdot A_{G-W} \quad (72)$$

Where, $\boldsymbol{\mu_{G-W}}$ is the friction coefficient between grain and workpiece material;

$\bar{\boldsymbol{p}}$ is the pressure on the interface, which can be derived from previous cutting simulation;

$\boldsymbol{A_{G-W}}$ is the area of grain and workpiece contact.

According to the tool wear model developed by Usui [76], the wear flat development during grinding can be estimated as a function of time as in Equation 67.

$$dA_{G-W}/_{dt} = C \cdot \delta_n \cdot V_s \cdot exp\left(-\lambda/_{\theta}\right) \quad (73)$$

Therefore, Equation 68 shows the calculation of the sliding force, which is equivalent to the glazing force.

$$F_{G-W} = \mu_{G-W} \cdot \bar{p} \cdot C \cdot \delta_n \cdot V_s \cdot \exp\left(-\lambda/_{\theta}\right) \cdot dt \quad (74)$$

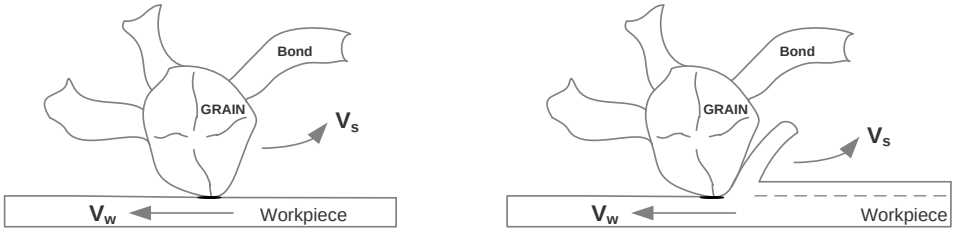

(a) Grain-workpiece friction

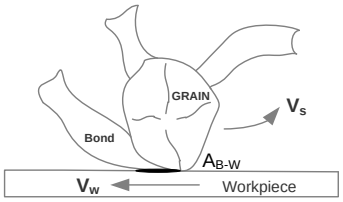

(a) Bond-workpiece friction

Figure 69 Grain-workpiece and bond-workpiece sliding in grinding

Bond-workpiece is another key area that differs grinding from cutting. As grain wars or breaks down from the bond material, some of bond material rubs against the workpiece material consuming energy and as a result raising the specific energy requirement and heat generation, as shown in Figure 69. The bond-workpiece friction seems insignificant in conventional grinding, however, would play an important role in super-abrasive machining where the metal bond is used as bonding agent [77]. The calculation of friction force between bond and workpiece material is similar to grain-workpiece sliding, the proportional relationship between the bond-workpiece friction force and bond-workpiece contact area still applies. Therefore, the bond-workpiece friction force can be expresses as:

$$F_{B-W} = \mu_{B-W} \cdot \bar{p} \cdot A_{B-W}(t) \tag{75}$$

Where, μ_{B-W} is the friction coefficient between bond and workpiece material;

$\bar{p}$ is the strength of the bond, which is associated with the wheel hardness;

A_{B-W} is the contact area of bond and workpiece contact.

5.6. Summary

In this chapter, the microscopic interaction analysis is carried out by means of Finite Element Method and analytical approach. For the analytical study of loading phenomenon, it correlates the loading occurrence with the process kinematics and enables the quantification of the loading force. For the FEM study of single grain cutting, the mechanism of single grain cutting can be studied and the database can be established for further data retrieval for the physical based simulation. In addition, following conclusions for single grain cutting can be drawn.

- A method is developed to apply single grain cutting FEM simulation into grinding simulation.

– The material removal mechanism is studied through single grain cutting simulation. The effect of cutting parameter, grain parameter, and workpiece material on material removal are studied qualitatively.

– A database is established to support the physics based simulation by providing the single grain force and the resultant workpiece side flowing geometry under a range of cutting conditions.

6. Process Integration

While the virtual wheel model is determined and the microscopic interaction analysis is specified, the process integration is initiated as indicated in Figure 70. The process integration carried out in form of iteration, and can be divided into kinematics simulation and kinetics analysis. When the kinematics simulation starts, the wheel surface and the workpiece are transferred into the same coordinate system. At ***t=0***, the grinding wheel stays away from the workpiece for some distance without contacting the workpiece. For each time incremental ***Δt***, the wheel rotates and translate linearly toward the workpiece with respect to the wheel speed and in-feed rate. As soon as the wheel contacts the workpiece, the localized contact condition for each individual active grain ***i*** is determined in terms of the grain – workpiece engagement cross-section area $\boldsymbol{CSA_i}$. Through calling the data from the microscopic interaction analysis, 6 modes could be recognized and identified. The plastic material pile-up on both sides of grain tip should also be considered as a function of ***CSA***, therefore, the workpiece surface updates at each simulation iteration step. The chip volume generation can also be determined as a function of ***CSA***. In the kinetics analysis, single grain force for material removal can be determined as a product of engagement cross-section area *A*. And the loading force can be calculated based on the accumulated chip volume. When taking the wheel-workpiece contact zone as a whole, the number of cutting and plowing grains, the grinding force, and the resultant surface texture can be derived from the integration. The iteration keeps on till the time reaches the pre-set value *T*.

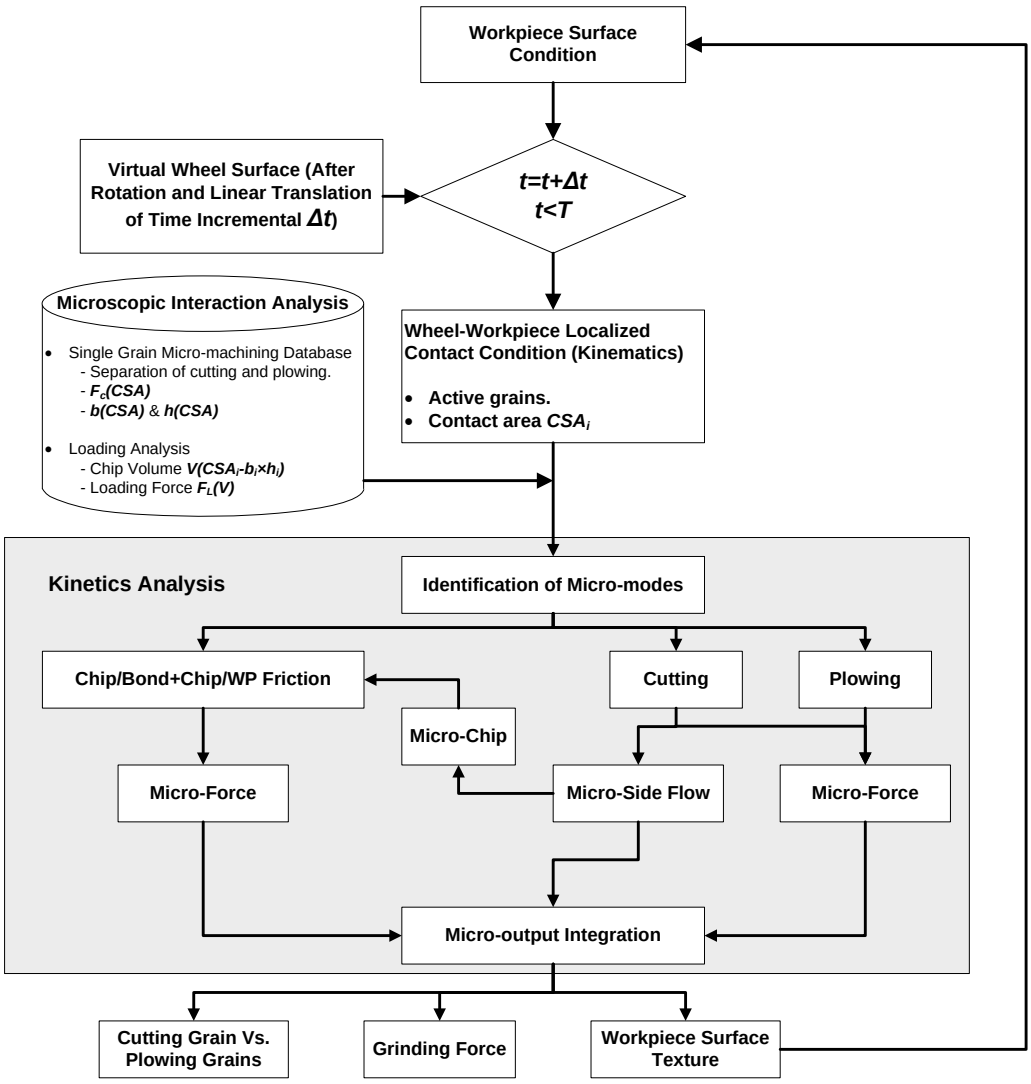

Figure 70 Flowchart of process integration

6.1. Kinematics Simulation

The kinematics model serves to simulate the wheel moving against the workpiece under the specified process parameters. The simulation provides the number of active grains and contact cross-section area for each grain CSA_i, as indicated in Figure 70. In a down grinding process, during each iteration interval Δt, the wheel surface move relatively respect to the workpiece complying with the grinding parameters. For any point $W(x,y,z)$ on the wheel surface, the new position of the wheel surface $W(x',y',z')$ after Δt can be calculated by the equation below.

$$x' = x - v_s \cdot \Delta t - v_w \cdot \Delta t \tag{76}$$

$$y' = y \tag{77}$$

$$z' = z + h - \sqrt{h^2 - (v_s \cdot \Delta t + v_w \cdot \Delta t)^2} \tag{78}$$

where,

$\boldsymbol{V_s}$ is the grinding speed,

$\boldsymbol{V_w}$ is the wheel in-feed speed,

h is the protrusion height of the corresponding wheel point, which is defined as the distance between the wheel surface point and wheel center in the wheel model. Then the workpiece surface is updated by comparing the wheel surface profile with the workpiece surface profile.

$$WP[x', y', z(t + \Delta t)] = min\{WP(x', y', z'), W(x', y', z')\} \tag{79}$$

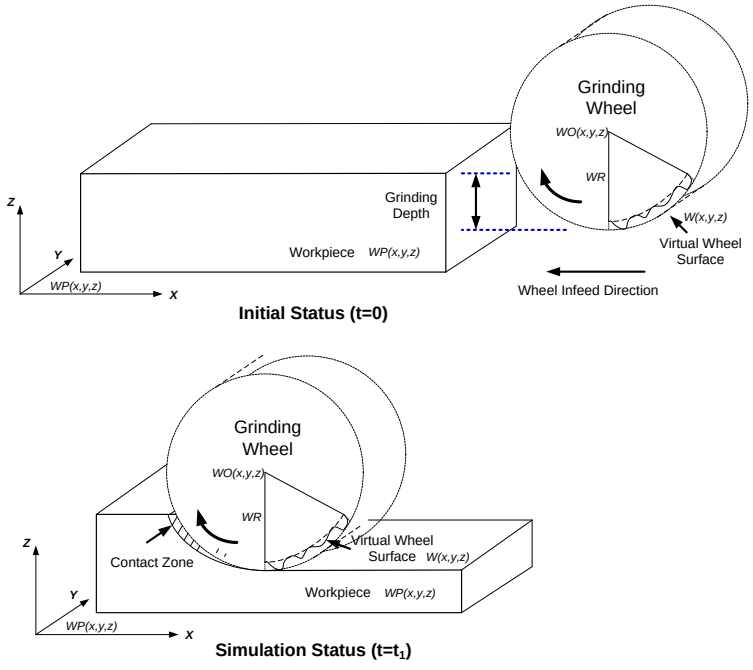

Figure 71 Coordinate system for kinematics simulation

This kinematic simulation provides the engagement condition of each grain and workpiece, through which the cross-section area ***CSA*** of material removal by each grain can be deduced. By calling the side flow geometry parameters from the single grain micro-machining database in Chapter 4, the generated side flow is adding to the workpiece surface. In addition, multiplying specific force with the cross-section area of grain-workpiece engagement, the force consumption on each single grain can be obtained. Integration of the all the microscopic force gives the grinding force (power) consumption in global scale, which also gives a discrete heat source moving along the workpiece surface for future grinding temperature calculation.

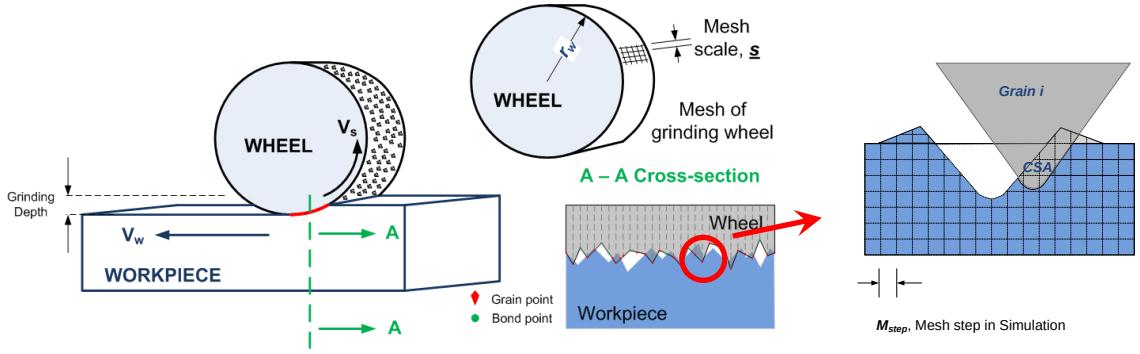

Figure 72 Kinematics simulation

In this study, the kinematics simulation is carried out to imitate the grinding process of a fresh dressed wheel. Therefore, the grain-workpiece sliding and bond-workpiece are not significant. Therefore, only cutting and plowing, chip/bond friction, and chip/workpiece friction modes are considered in the simulation.

The direct output from the kinematics simulation is the engagement cross-section area of grain – workpiece. The other two kinematics output, side flow formation and the chip generation are calculated based on the derived cross-section area. All the kinematics output measures provide the basis for kinetics analysis. The mathematics to determine the kinematics output is described as following.

The grain-workpiece engagement cross-sectional area needs to be determined for all active abrasive particles in the wheel-workpiece contact zone as indicated in Figure 72. For a specific time instance ***T***, all the active abrasive particles can be detected in the simulation, and the engagement cross-section area ***CSA*** for any active grains will be determined.

6.2. Kinetics Analysis

While the engagement condition of grain-workpiece CSA_i is detected for all active grains, the single grain force $F_{c,i}$, the side flow geometry in terms of ***b*** and ***h*** can be derived from the micro-cutting simulation database. Figure 73 shows the interrelation of the kinematics simulation results with regard to the database. In the database, the grain is conical aluminum oxide with 90° apex angle, cutting of hardened ***D2*** steel at for various cutting conditions as described in Chapter 5.

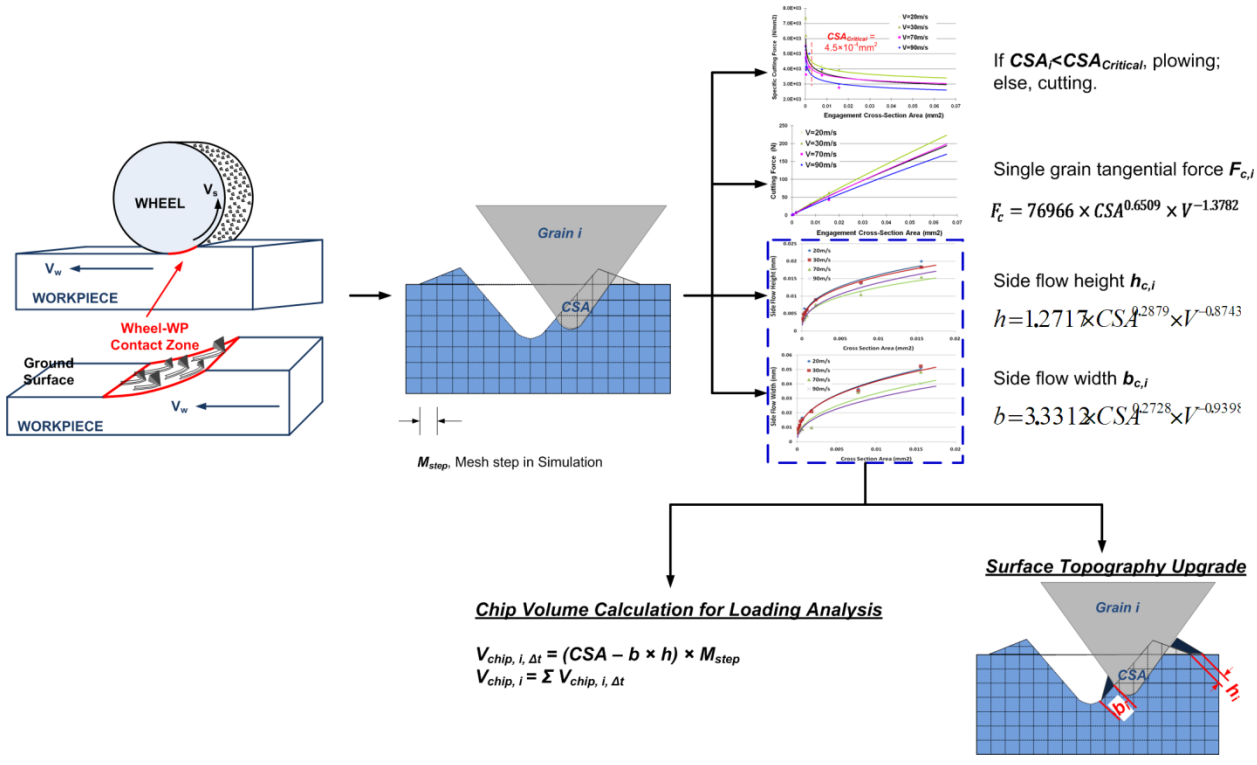

Figure 73 Supportive database for kinetics analysis

6.2.1. Plowing/Cutting Mode and Tangential Force

From the contacting condition of all active grains, the number of cutting and plowing grain can be deduced for mechanism study. The single grain micro-machining database suggests that the specific force decrease sharply while the ***CSA*** value increases up to $4.5 \times 10^{-4} mm^2$. Hence the critical contacting cross-section area $\boldsymbol{CSA_{Critical}}$ can be defined as $4.5 \times 10^{-4} mm^2$. Therefore, for the grains whose ***CSA*** values are smaller than $\boldsymbol{CSA_{Critical}}$ are regarded as plowing grains, and the others are regarded as cutting grains. Similarly, the tangential force $\boldsymbol{F_c}$ can also be calculated based on the regression equation derived from the single grain micro-machining database.

6.2.2. Side Flow Geometry

Due to the material plastic deformation, the side flow always forms whenever an abrasive grain contact with the workpiece. The side flow is regarded as a triangular shape and characterized by its width ***b*** and height ***h***. On one side, the side flow pile-up, as an effect of material plastic deformation, causes additional material removal for the successive grain and forms the final surface roughness. On the other hand, the side flow reflects the chip formation of the single grain micro-machining. More side flow generation means less chip formation. Therefore, the side flow formation can also be used to quantify the chip formation of an active grain for loading force analysis.

6.2.2.1. Surface Texture Update

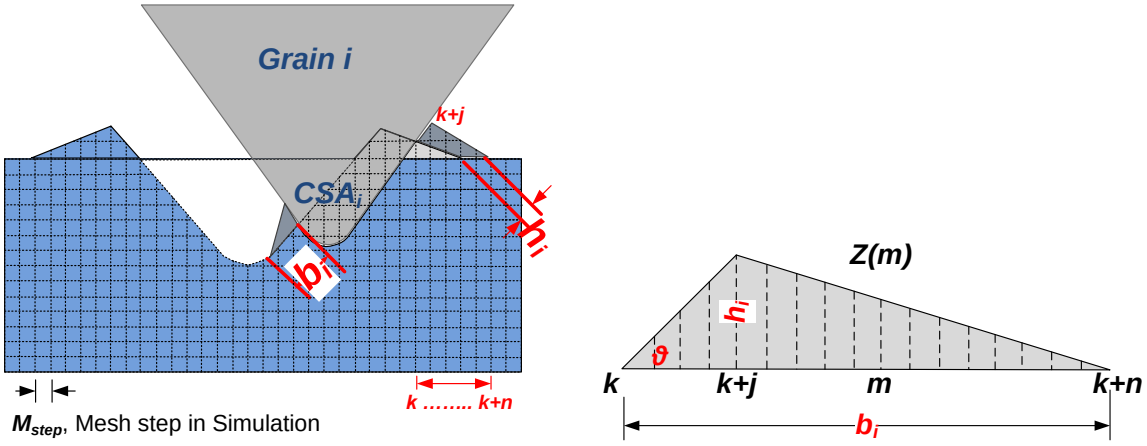

Figure 74 Surface update considering side flow

In the simulation, while the side flow geometry b_i and h_i are determined for the i^{th} grain, the material pile-up is modeled as a function of the engagement condition. Figure 74 demonstrates the algorithm for surface texture update in one iteration step. In this case, while grain ***i*** contact with the workpiece, the workpiece surface ***Z*** update due to the side flow on the right is expressed as:

$$Z'(m) = Z(m) + (m-k) \times M_{step} \times \cot\theta \,; k \le m \le (k+j) \tag{80}$$

$$Z'(m) = Z(m) + \left[b_i - (m-k-j) \times M_{step}\right] \times h_i/(b_i - h_i \times \cot\theta); (k+j) < m \le (k+n) \tag{81}$$

where, ***k*** is the immediate mesh number on the right for the grain-workpiece contact, ***j*** is the immediate mesh number where the tip of the side flow is, ***n*** is the immediate mesh number where the side flow ends, ***θ*** is half cone angle.

6.2.2.2. Chip Generation and Loading Force Calculation

Although in grinding most active abrasive grains contact partially with the workpiece, the chip formation can still be calculated if the engagement cross-section area is derived. Therefore, the chip volume generated from the grain start to cut the workpiece till the grain leave the workpiece can be regarded as the integration of the small chip segment generated at all steps during the procedure. For each step at the length of $\boldsymbol{M_{step}}$, the chip volume for this minute duration is expressed as below.

$$V_{chip}^{i} = \left(CSA_1^i - b_1^i \times h_1^i\right) \times M_{step} \tag{82}$$

And the chip volume generated by this cut can be described as following.

$$V_{Chip} = \sum_{i=1}^{n}\left(CSA_1^i - b_1^i \times h_1^i\right) \times M_{step} \tag{83}$$

As in grinding process, one grain may interact with the workpiece a number of times as the wheel spins, if a grain interacts with the workpiece for m times, the accumulated chip volume in front a grain can be calculated given the chip retaining coefficient is $\boldsymbol{\eta}$.

$$V_{Chip} = \sum_{i=1}^{m} V_{Chip,i} \times \eta \tag{84}$$

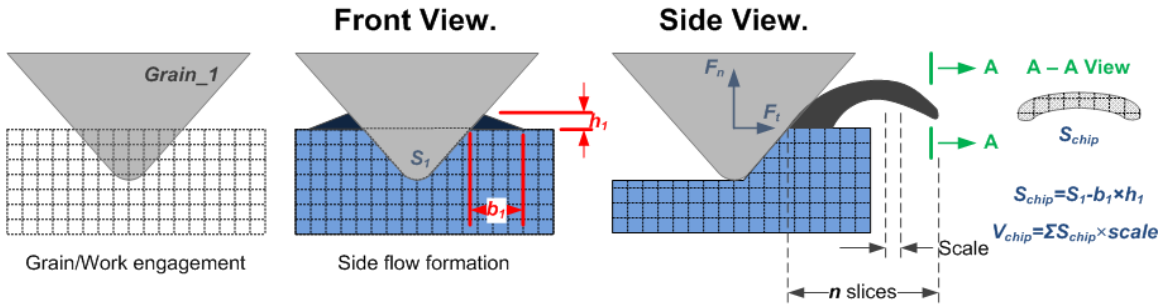

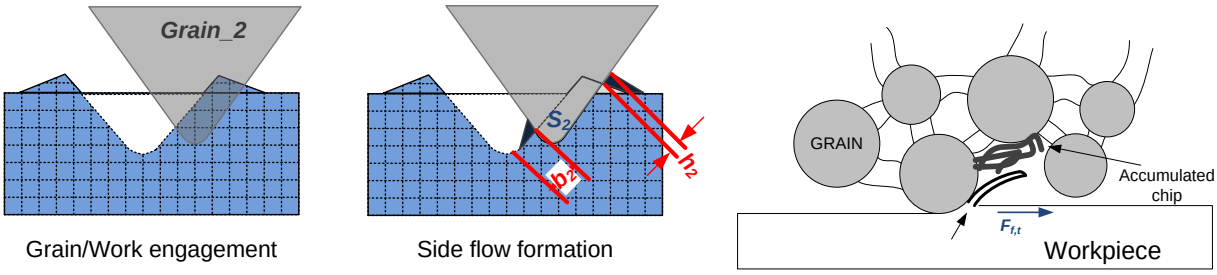

Grain/Work engagement Side flow formation

Figure 75 Chip volume calculation

In the simulation, the loading force is expressed as a function of the ratio between the generated chip volume versus the average effective pore volume. For the loading force calculation, unlike the grain-workpiece interface, chip-workpiece friction dominates at the interface. Therefore, the loading force can be regarded as a frictional force complying with Columbus Law. For an individual grain, the average loading force is calculated as below.

$$F_{f,t} = \mu_{avg} \cdot p_{chip} \cdot \left({}^{V_{chip}}\!/_{V_{pore}} \right) \tag{85}$$

6.3. Force Integration

The force integration serves to sum up all the microscopic force into the global scale. In the wheel-workpiece contact zone, there would be hundreds of grains interacting with the workpiece on a curled surface as indicated in the Figure 76. Therefore, the tangential grinding force equals to the product of scalars of all single grain cutting force on the ***x*** direction.

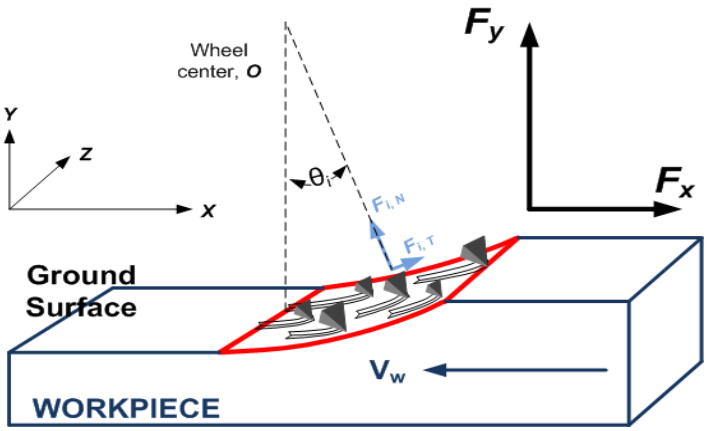

Figure 76 Force integration for kinetics analysis

$$F_x = \sum_{i=1}^{n} F_{i,T} \cdot \cos\theta_i - F_{i,N} \cdot \sin\theta_i \quad (86)$$

$$F_y = \sum_{i=1}^{n} F_{i,N} \cdot \cos\theta_i - F_{i,T} \cdot \sin\theta_i \quad (87)$$

where,

F_x and F_y are the tangential and normal grinding force, respectively; n is the number of active grains; $F_{i,T}$, $F_{i,N}$ are the tangential and normal force of the microscopic mode, respectively; and θ_i is the angle between the axis of the i^{th} grain and the normal direction of the workpiece coordinate system.

6.4. Simulation Results Analysis

In order to verify the effectiveness of the simulation, the result from the simulation is compared with the experiment. The grinding is performed on the M7120 universal grinding machine with white corundum grinding wheel P250_25_75 WA46L8V, which means grinding wheel's external diameter is 250 mm, and the width is 25 mm, the inner diameter is 75mm. In the grinding process, severe abrasion of grinding particles in the surface of grinding wheel would induce larger grinding force and high temperature, which exerted negative influence on the surface integrity. To retain the right shape and the sharpness of grinding wheel, dressing

diamond was used to dress the grinding wheel. The cutting force was measured by Kistler model 9272 four-component piezoelectric dynamometer.

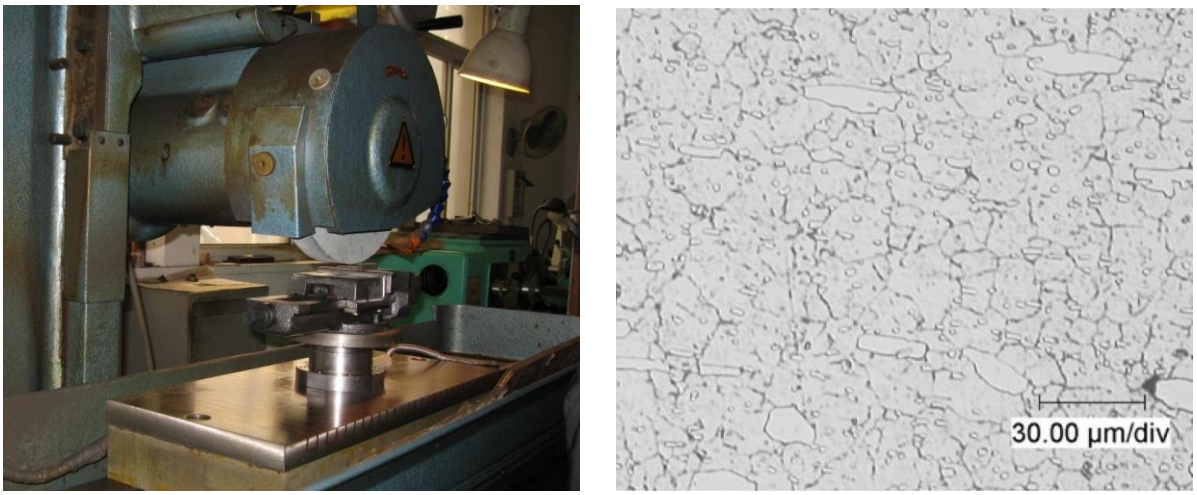

Figure 77 Experimental setup and the metallurgy structure of workpiece (D2)

The workpiece material is D2 steel in hardened state with an average hardness about HRC60. And the grinding process parameters are carried out as following:

TEST	Depth of Grinding (mm)	Feed Rate (mm/min)	Grinding Speed (m/s)	Tangential Force (N)	Ra (µm, cross the wheel in-feed)	Remark
A	0.03	360	20.0	67.1	1.308	Down grinding without coolant.
B	0.08	360	20.0	91.4	1.217	
C	0.12	360	20.0	102.4	1.474	
D	0.15	360	20.0	201.4	1.562	

Table 9 Experiment parameter

6.4.1. Simulation Results

The workpiece surface texture is the direct output from the simulation as indicated in Figure 78. The peak and valley can be observed clearly from the simulated ground surface. The simulated surface is also able to provide the profile information, based on which the surface

roughness ***Ra*** can be calculated. Figure 79 shows the comparison of simulated surface roughness with the experiment data, which indicates that the simulated values are close to the experimental data. It also implies that the surface roughness is less sensitive to the depth of grinding, which are proved to be reasonable from literature and experiments [78]. The differences of the simulation and the experiment may lie in 2 folds: 1. In the experiment, the system is not perfectly rigid, the grinding wheel and abrasive grains may retreat somewhat during grinding, resulting in smaller roughness; 2. The current mesh size in the physics based simulation is 5μm, and a smaller mesh size may be required for higher accuracy.

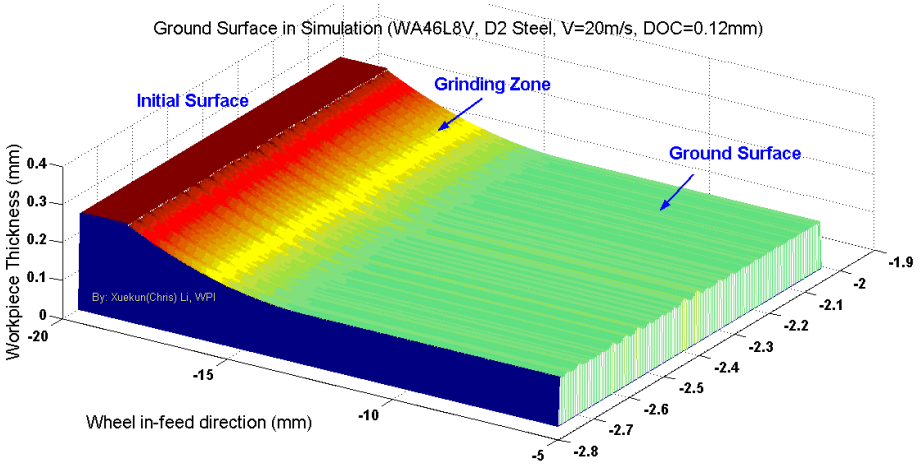

(a) 3D surface texture of the ground surface in simulation

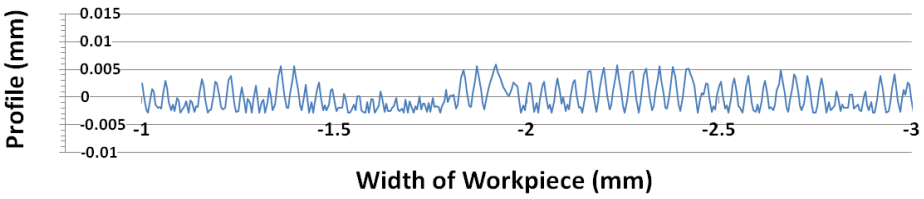

(b) Surface profile of the ground surface in simulation

Figure 78 Ground workpiece surface and roughness *Ra* in simulation

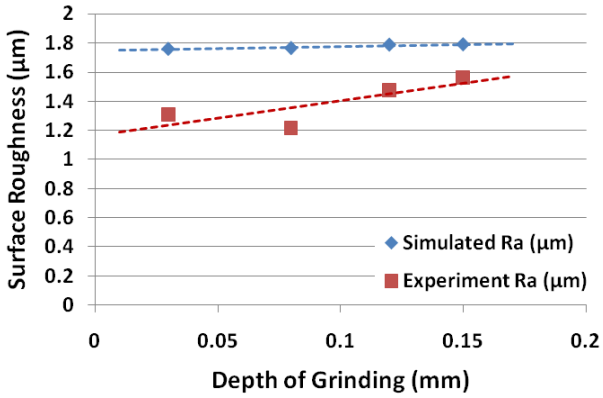

Figure 79 Comparison of surface roughness *Ra*

The comparison of grinding force shows good agreement of simulation results with the experimental data in Figure 80. Figure 80(b) indicates the development of tangential grinding force on a time dependent basis. And the grinding force increase as the depth of grinding raises. In the simulation, about 20% power is consumed by cutting, and the value will increase by 50% as the depth of grinding increase. However, the 20% power is consumed only by less than 5% grains, which suggest that the grinding process is indeed sensitive to the cutting/plowing ration by Figure 81 and Figure 82. The differences between the experimental value and simulation may mainly result in the lack of wheel loading analysis.

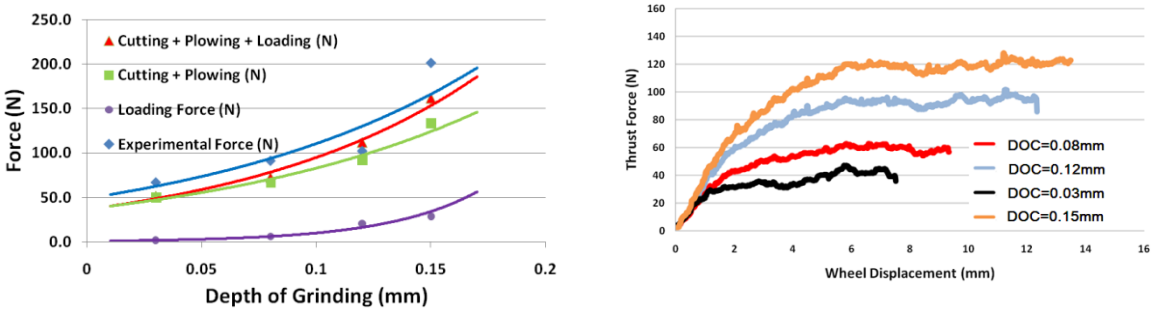

(a) Simulation Vs. Experiment (b) The thrust force curve from the simulation

Figure 80 Comparison of experiment and simulation

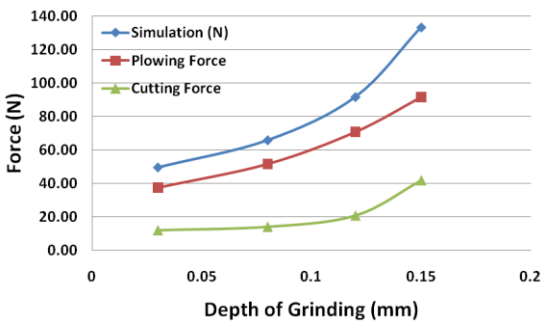

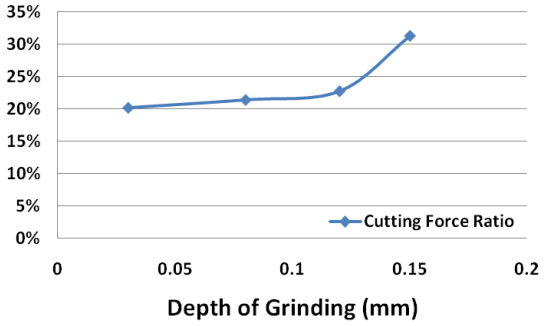

(a) Cutting Vs. Plowing **(b) Cutting force / (Cutting force + plowing force)**

Figure 81 Cutting force Vs. plowing force in simulation

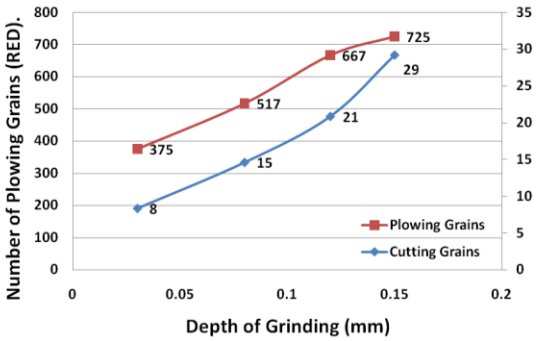

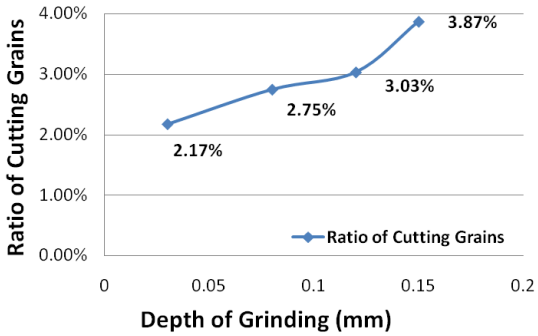

(a) Cutting grains Vs. Plowing grains **(b) The ratio of cutting grains**

Figure 82 Cutting grains Vs. Plowing grains

For a better predictability, the loading force should also be taken into consideration in the simulation. The chip volume generated in grinding process is necessary, as loading force is described as the ratio between accumulated chip volume versus the pore volume. Assuming that only 1% chip can be retained in the pore due to the coolant flushing and centrifugal force, the average accumulated chip volume for an active grain is described in Figure 83. The average pore volume for the selected wheel is 0.0621mm^3. Then the global loading force can be calculated with Equation 80.

$$F_{Loading} = \mathrm{N} \cdot \mu_{avg} \cdot p_{chip} \cdot \left({}^{V_{chip}}\!/_{V_{pore}} \right) \quad (88)$$

Where, $\boldsymbol{N}$ is the number of active grains; $\boldsymbol{\mu_{avg}}$ is the friction coefficient, which is about 0.5 for D2 steel; $\boldsymbol{p_{chip}}$ is estimated as 66800Mpa*mm^2 for D2 steel.

The global grinding force in Figure 83, therefore, is the summation of cutting force, plowing force, and loading force. It indicates that the loading force may become prominent when the depth of grinding increases, reaching up to 15% in the overall power consumption.

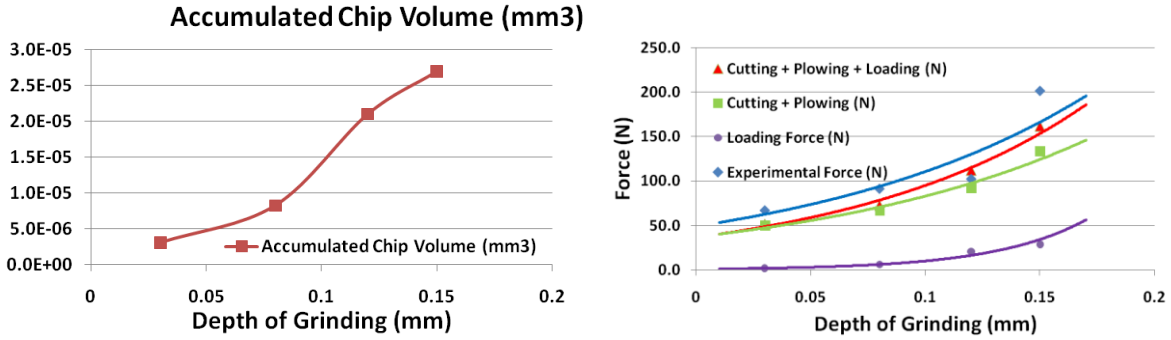

Figure 83 Accumulated chip volume, simulation results Vs. Experimental value

6.4.2. Discussion on the Time Dependent Behavior

As the grinding wheel surface condition changes due to loading whilst the grinding process, the grinding force or power curve will exhibit some time dependent behavior. Typically the power curve can be decomposed into 2 straight lines with different slopes as indicated in Figure 84. Line 1 typically reflects the dynamic process as the grinding wheel goes into the workpiece; while line 2 indicates the power incremental as a function of the wheel displacement as the wheel get loaded with chips.

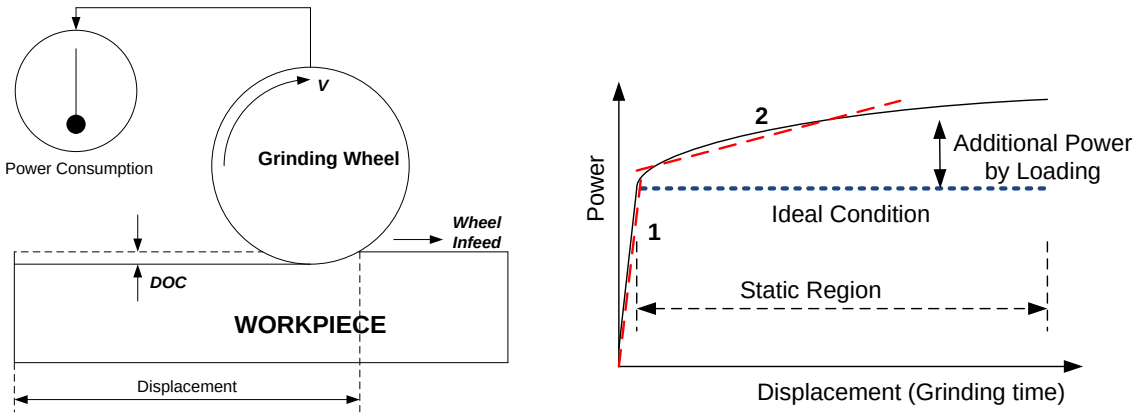

Figure 84 Time dependent behavior of surface grinding process

Therefore, for a specific depth of grinding, the force curve can be expressed with Equation 81 and 82. Figure 85 describes the force draw for various grinding depth, which can provide the basis for force prediction for grinding cycle with different stages.

$$f_t = k_1 \cdot x;\ (0 < x < grinding\ arc\ length) \tag{89}$$

$$f_t = k_2 \cdot x + b; (x \geq grinding\ arc\ length) \tag{90}$$

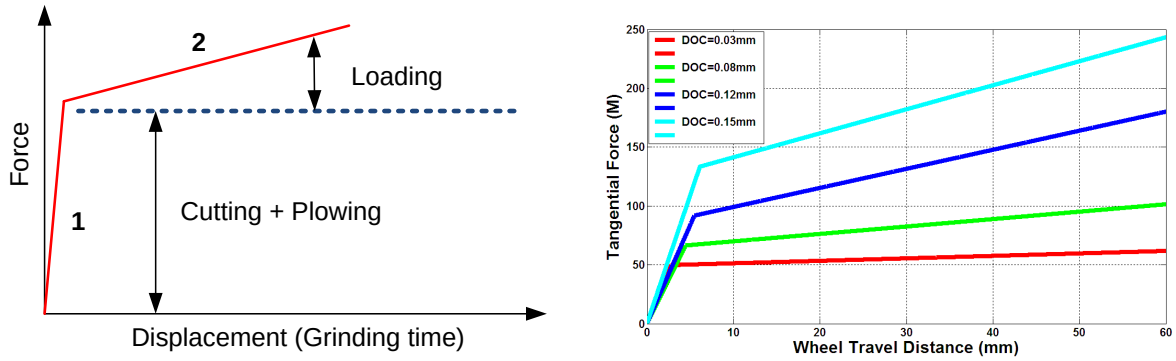

Figure 85 Force draw for different grinding depth (WA46L8V-D2 steel)

To study the time dependent behavior for a grinding cycle, 2 sample grinding cycles are initiated. For the first grinding cycle, it include 3 stages, 1 rough grinding with a 0.12mm material removal, 1 semi-finish grinding with a 0.08mm material removal, and 1 finish grinding with a

0.03mm material removal. The grinding wheel is dressed before cycle starts, and no in-process dressing is used. For the second grinding cycle, it has the same 3 stages, the differences is that the wheel is dressed after each stage to eliminate the loading phenomenon.

To facilitate the data acquired in previous analysis, it is assumed that the workpiece material is hardened D2 steel, the grinding wheel is WA46L8V, no coolant is used during the process. The grinding wheel diameter is 250mm, at a grinding speed of 20m/s, the length of the workpiece is 30mm, and the width is 3mm. Assuming that the cutting and plowing condition don't alter too much, and the chip loading is the major cause of the time dependent behavior. In the simulation, the chip accumulation can be calculated and is stored in the model to determine the loading force. To simplify the problem, the transient stage is not considered.

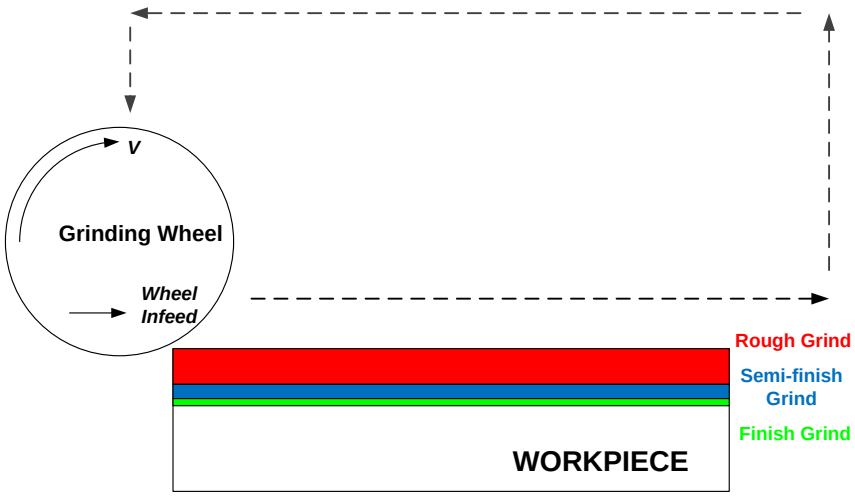

Figure 86 A grinding cycle with multiple stages

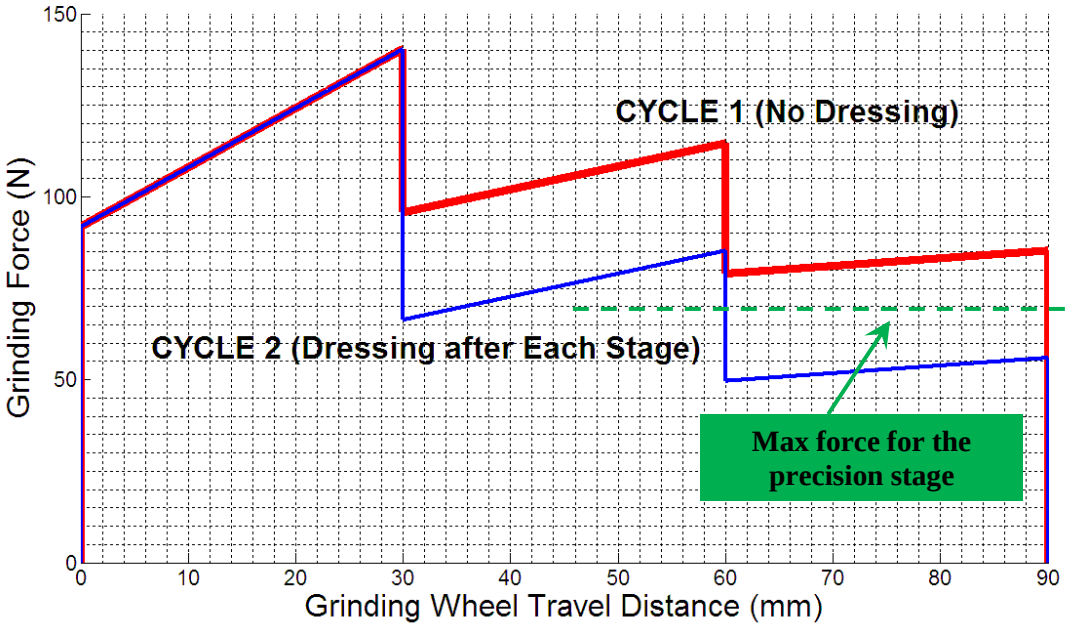

Figure 87 Tangential grinding force comparison for 2 cycles

The tangential force comparison of the 2 cycles is demonstrated in Figure 87. For a specific application, the maximum force allowed the precision stage can usually be estimated. Therefore, with the data provided by the model, cycle 1 may not be suitable to meet the requirement. Cycle 2 may meet the requirements, but other cycle design may still apply depending on the detailed process specification.

6.5. Summary

In this chapter, the physics based grinding process model is developed, and the programming with MATLAB is accomplished. The simulation could be able to depict the cutting, plowing, and loading in the process, and calculate the force used by each mode. The simulated results complies with the experiments well, and establishes the correlation of grinding input with output measures through the microscopic mode quantification. In addition, the data acquired from the model can also be applied for predictive multi-stage grinding process design and

optimization, which can make the grinding process less ambiguous and eliminate the ‘trial and error’.

7. Conclusions and Future Work

This research involves a systematic and comprehensive study on the grinding process modeling from a microscopic point of view. The physics that takes place in grinding are analyzed, which can enhance the grinding process understanding, process modeling and optimization. The method covers a grinding wheel model, microscopic mode analysis, and process integration. This chapter summaries this dissertation and proposes potential works for future research.

7.1. Conclusions and Contributions

Modeling of the physics in grinding process is always challenging due to the complexities in the process. Understanding and modeling the physics in terms of characterization and quantification of microscopic modes in grinding can be a powerful tool to enhance grinding mechanism understanding, process optimization, and proactive design. In addition, the advancement in grinding science understanding also promotes the innovation of grinding technology awareness in terms of novel product and process development. The dissertation develops the grinding process model from a microscopic point of view, which bridges the gap between the theoretical research and the industrial need. In general the contribution of this research includes:

- The development of the research methodology to characterize and quantify the microscopic modes in grinding processes, which includes the fabrication process analysis based grinding wheel modeling, FEM based microscopic interaction analysis, and process integration. The research methodology covers the comprehensive process phenomenon, and correlates process technical output with input through calculation of the micro-output measures. In addition, the methodology also enables the investigation of the time dependent behavior for proactive process design as well as optimization.

- The development of fabrication process analysis based grinding wheel model, on one hand, enables the modeling of the microscopic models; on the other hand, provides an effective tool for wheel fabrication procedure analysis, diagnosis, and proactive design. Therefore, the grinding wheel model itself can be used to evaluate the wheel composition selection, wheel manufacturing procedure analysis, as well as wheel behavior quantification study to minimize the 'trial and error' in current wheel fabrication process and make the wheel properties more predictable and controllable.
- The Finite Element Analysis based microscopic mode study incorporate the up-to-date technique in micro-machining simulation into grinding process analysis, which is capable to cope with various grinding conditions when constructed as database. In addition, the FEA simulation advances the understanding of single grain micro-machining. It could reveal the optimal grain parameters or process parameters in micro-machining, which assists the grain selection for wheel making or operational parameter selection for grinding process. Furthermore, the stress/strain field analysis from the FEA simulation also enhances the theoretical and fundamental synthesis of single grain micro-machining.
- The final output of the process model includes but is not limited to grinding force, and 3D workpiece surface texture. The simulations results comply with the experimental results well, which proves the viability of the methodology. Apart from that, the number of cutting, plowing grains, force usage for cutting, plowing, and loading modes can be derived from the model, too. When assisted with more experimental observation and measurements, this would help the process quantification and proceed the mechanism understanding.

7.2. Limitations, Potential Applications, and Future Work

In general, this dissertation formulates the research framework and methodology of investigating into the physics of grinding processes, and proves the viability of the model. However, due to the complex nature in terms of instantaneous behaviors in grinding, following phenomenon may not be modeled only if advancements in the framework and methodology are made.

- The instantaneous response of the workpiece material in terms of the work-hardening, thermal softening, and the workpiece metallurgy structure change should be taken into consideration in the process integration level. Figure 88 shows the plastic strain and temperature profile after single grain micro-machining. It is observed that the workpiece material exhibits some work-hardening and thermal softening effect, which would affect the material properties for the next cut. The work-hardening makes the workpiece tougher, while the elevated temperature softens the workpiece material. In addition, the high temperature also induces phase transformation of the workpiece material, which makes the prediction of workpiece properties more difficult. So far, in the dissertation work the material that piles on both sides as well as beneath the cutting traces is considered to be of the same properties as the initial matrix.

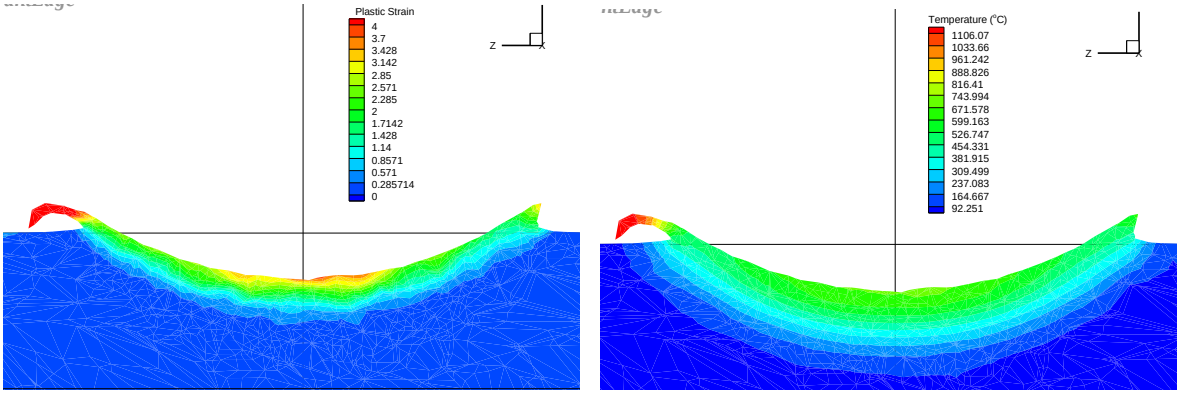

Figure 88 Plastic strain and temperature profile of workpiece material

- For the loading analysis, the reason of its occurrence may range from chip-grain material adhesion, chip-bond adhesion, and chemical affinity. While in this dissertation, the loading phenomenon is regarded as a pure friction process, and described as a function of the chip accumulation volume versus the effective pore volume.
- In the single grain micro-machining simulation, the material constitutive model is one dominant factor that impacts the accuracy of the Finite Element simulation. Currently, the constitutive model is constructed in the power law format, which assumes the uniformity of the workpiece in phase. This would be valid when the depth of cut is much larger than the grain size. However, when the nominal depth of cut is at the same order of the grain size, usually around 10 microns as indicated in Figure 89, it may not be proper to consider the material to be uniform. The imbedded phase and the grain boundary usually behave differently than the matrix material, and would influence the material removal and chip formation in the micro-level. Further improvement of the FEM simulation relies on the advancements of the material constitutive modeling determination.

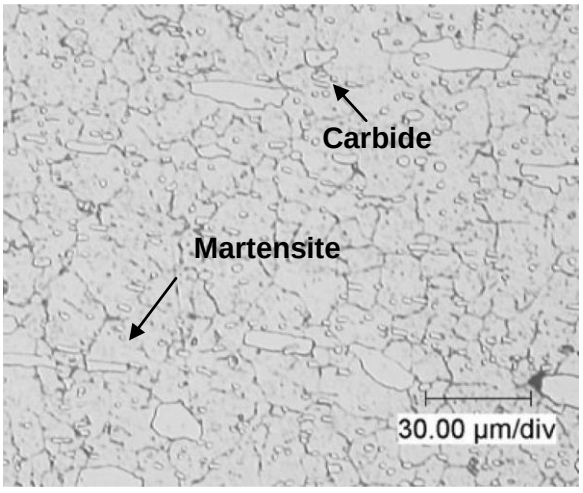

Figure 89 Metallurgy structure of D2 steel (hardened)

7.3. Potential Applications and Future Work

The entire grinding process model can be effective in predicting the technical output measures of the process and explaining the mechanism in grinding process. This leads to a qualitative justification of power draw shift, which assists the grinding cycle optimization as well as proactive process parameter design. The grinding wheel model itself can be used to optimize and design the wheel composition as well as its fabrication parameters, which could minimize the 'trial and error' in current wheel design procedure and be able to proactive design wheels tailored to specific applications. The FEM based single grain micro-machining analysis visualizes the process. Therefore, the grain or process parameter optimization, and mechanism study can be carried out with the aid of FEM package.

Although proved to be viable, the process model still needs to be improved. Based on the scope of the present research on grinding process modeling, the following recommendations are made for future work.

- Within current research scope, the grinding heat and temperature is the next goal to accomplish. The heat source generation can be determined through the process integration and calling the data from the single grain micro-cutting analysis. In addition the heat transfer model should be developed for the temperature calculation and surface integrity prediction. Furthermore, the grain wear and grinding wheel wear can be estimated through comparing microscopic force with wheel localized properties. This would enable the model an improved predictability on the wheel consumption and future cost analysis. Finally, the system stiffness can be incorporated into the process integration module for better approaching the real situation.
- For the grinding wheel model, more grit geometries should be considered, such as the pyramid or the column. The introduction of complex geometry could increase the

computation requirement, which should also be considered for further improvement. In addition, the chemical reaction as well as the rheology behavior the vitrified bond material should be understood for enhancement of the wheel model. In addition, the dressing simulation, which involves the contacting mechanics and the material sciences, should be improved to take the real grain breakage effect into consideration. The improvement in the overall wheel model also helps the accurate prediction of wheel modulus with the real product.

- The FEM simulation visualizes the micro-machining processes and assists the factorial analysis for grain geometry as well as process parameter analysis. Therefore, more single grain micro-machining simulations should be carried out for various grain geometry factors to achieve a comprehensive understanding on micro-material removal in grinding processes. The grain geometry may cover other regular shapes from the tetrahedron, elongated column, to the geometry from measurement.
- In terms of verification of the process model, advanced monitoring and measurement techniques may be necessary to capture and quantify the loading phenomenon and to measure the cutting and plowing grains. Last but not the least in the increase of the computational capability of the virtual wheel model and the process integration module, which enables obtaining of simulation results within shorter time.

8. References

1. **Malkin, S. and Guo, C.** *Grinding technology - Theory and applications of machining with abrasives.* New York : Industrial Press, 2008.

2. *Abrasive machining in the future.* **Inasaki, I., Tonshoff, H.K. and Howes, T.D.** 2, 1993, Annals of the CIRP, Vol. 42, pp. 723-732.

3. *Grinding process achievements and their consequences on machine tools challenges and opportunities.* **Tonshoff, H. K., Karpuschewski, B. and Mandrysch, T.** 2, 1998, Annals of the CIRP, Vol. 47, pp. 651-668.

4. *Process monitoring in grinding.* **Tonshoff, H. K., Friemuth, T. and Becker, J. C.** 2, 2002, Annals of the CIRP, Vol. 51, pp. 551-571.

5. *Contributions of CIRP research to industrial problem in grinding.* **Peters, Ir. J.** 2, 1984, Annals of the CIRP, Vol. 33, pp. 451-468.

6. *The characterisation of grinding wheels usding 3D surface measurement techniques.* **Butler, D. L., et al.** 2002, Journal of Materials Processing Technology, pp. 234-237.

7. *A system approach for the used of vitrified bonded superabrasive wheels for precision production grinding.* **Subramanian, K. and Lindsay, R. P.** 1992, Vol. 114, pp. 41-52.

8. *Mechanisms of material removal in the precision production grinding of ceramics.* **Subramanian, K., Ramanath, S. and Tricard, M.** 1997, Journal of Manufacturing Science and Engineering, pp. 509-519.

9. *Modelling abrasive wear.* **Torrance, A. A.** 2005, Wear, Vol. 258, pp. 281-293.

10. *Temperatures and energy partition for grinding with vitrified CBN wheels.* **Guo, C., et al.** 1, 1999, Vol. 48, pp. 247-250.

11. *Loading of the grinddng wheel phenomenon and measurement.* **Konig, W.** 1, 1978, Annals of the CIRP, Vol. 27, pp. 217-219.

12. *Phenomenon of wheel loading mechanisms in grinding.* **Lauer-Schmaltz, H. and Konig, Ing. W.** 1, Aachen : s.n., 1980, Annals of the CIRP, Vol. 29, pp. 201-206.

13. *Dressing process model for vitrified bonded grinding wheels.* **Linke, B.** 1, 2008, Vol. 57, pp. 345-348.

14. *Theoretical analysis of heat partition and temperatures in grinding.* **Ju, Y., Farris, T. N. and Chandrasekar, S.** 1998, Journal of Tribology, Vol. 120, pp. 789-794.

15. *Local contact deflections and forces in grinding.* **Saini, D. P. and Wager, J. G.** 1, 1985, Annals of the CIRP, Vol. 34, pp. 281-285.

16. *Local contact deflections in grinding - Groups of grains and single grains.* **Wager, J.G. and Saini, D.P.** 1, 1986, Annals of the CIRP, Vol. 35, pp. 245-248.

17. *Local elastic deflections in grinding.* **Brown, R. H., Saito, K. and Shaw, M. C.** 1, 1971, Annals of the CIRP, Vol. 21, pp. 105-113.

18. *Measurement and analysis of grinding processes.* **Subramanian, K.** 1999, Abrasives Magazine, Vol. Aprial/May, pp. 1-6.

19. *Modelling and simulation of grindnig processes.* **Tonshoff, H.K., et al.** 2, 1992, Annals of the CIRP, Vol. 41, pp. 677-688.

20. *Framework of an intelligent grinding process advisor.* **Shin, Yung C., Chen, Yu-to and Kumara, Soundar.** 1992, Journal of Intelligent Manufacturing, Vol. 3, pp. 135-148.

21. *An intelligent multiagent approach for selection of grinding conditions.* **Rowe, W. Brian, et al.** 1997, Annals of the CIRP, pp. 233-238.

22. *An intelligent system for grinding wheel condition monitoring.* **Lezanski, Pawel.** 2001, Journal of Materials Processing Technology, pp. 258-263.

23. *Closed loop simulation of grinding.* **Steffens, K.** 1, 1983, Annals of the CIRP, Vol. 32, pp. 255-259.

24. *Grinding process simulation based on the wheel topography measurement.* **Inasaki, I. and Shi, Yokohama.** 1, 1996, Annals of the CIRP, Vol. 45, pp. 347-350.

25. *A comparison of two models to predict grinding forces from wheel surface topography.* **Badger, J. A. and Torrance, A. A.** 8, 2000, International Journal of Machine Tools & Manufacture, Vol. 40, pp. 1099-1120.

26. *Analysis and simulation of the grinding process. Part I: Generation of the grinding wheel surface.* **Chen, Xun and Rowe, W. Brian.** 8, 1996, International Journal of Machine Tools & Manufacture, Vol. 36, pp. 871-882.

27. *Modelling of ceramic grinding processes Part I. Number of cutting points and grinding forces per grit.* **Li, Kun and Liao, T. Warren.** 1997, Journal of Materials Processing Technology, Vol. 65, pp. 1-10.

28. *Grinding force and power modeling based on chip thickness analysis.* **Hecker, Rogelio L., et al.** 2007, International Journal of Advanced Manufacturing Technology, Vol. 33, pp. 449-459.

29. *On the mechanics of the grinding process – Part I. Stochastic nature of the grinding process.* **Hou, Zhenbing and Komanduri, Ranga.** 2003, International Journal of Machine Tools & Manufacture, Vol. 43, pp. 1579-1593.

30. *A stochastic grinding force model considering random grit distribution.* **Chang, Huang-Cheng and Wang, J.-J. Junz.** 2008, International Journal of Machine Tools & Manufacture, Vol. 48, pp. 1335-1344.

31. *Analysis and simulation of the grinding process. Part II: Mechanics of grinding.* **Chen, Xun and Rowe, W. Brian.** 8, 1996, International Journal of Machine Tools & Manufacture, Vol. 36, pp. 883-896.

32. *Simulation of surface grinding process, part 2: interaction of the abrasive grain with the workpiece.* **Nguyen, T. A. and Butler, D. L.** 2005, International Journal of Machine Tools & Manufacture, Vol. 45, pp. 1329-1336.

33. *A three-dimensional model for the surface texture in surface grinding, Part 1: Surface generation model.* **Salisbury, Erik J., et al.** 2001, Journal of Manufacturing Science and Engineering, Vol. 123, pp. 576-581.

34. *Industrial challenges in grinding.* **Oliveira, J.F.G., et al.** 2009, Annals of the CIRP, pp. 1-18.

35. *Laser cleaning and dressing of vitrified grinding wheels.* **Jackson, M.J., et al.** 2007, Journal of Materials Processing Technology, Vol. 185, pp. 17-23.

36. *Grinding wheel selection.* **Jones, R.** 6, 1997, Metalworking Production, Vol. 141, pp. 43-56.

37. *A comparison of orthogonal cutting data from experiments with three different finite element models.* **Bil, Halil, Kılıc, S. Engin and Tekkaya, A. Erman.** 2004, International Journal of Machine Tools & Manufacture, Vol. 44, pp. 933-944.

38. *Slip-line modeling of machining with a rounded-edge tool - Part II analysis of the size effect and the shear strain-rate*. **Fang, N.** 2003, Journal of the Mechanics and Physics of Solids, Vol. 51, pp. 743-762.

39. *The size effect in metal cutting.* **Shaw, Milton C.** 2003, Sadhana, Vol. 28, pp. 875-896.

40. *Grinding process size effect and kinematics numerical analysis.* **Cooper, William L. and Lavine, Adrienne S.** 2000, Journal of Manufacturing Science and Engineering, Vol. 122, pp. 59-69.

41. *Development of a virtual machining system, part 1 approximation of the size effect for cutting force prediction.* **Ko, Jeong Hoon, et al.** 2002, International Journal of Machine Tools & Manufacture, Vol. 42, pp. 1595-1605.

42. *Finite element analysis of the influence of tool edge radius on size effect in orthogonal micro-cutting process.* **Liu, Kai and Melkote, Shreyes N.** 2007, International Journal of Mechanical Sciences, Vol. 49, pp. 650-660.

43. *Effect of plastic side flow on surface roughness in micro-turning process.* **Liu, Kai and Melkote, Shreyes N.** 2006, International Journal of Machine Tools & Manufacture, Vol. 46, pp. 1778-1785.

44. *Effects of process parameters on material side flow during hard turing.* **Kishawy, H.A. and Elbestawi, M.A.** 1999, International Journal of Machine Tools & Manufacture, Vol. 39, pp. 1017-1030.

45. *Analysis of the grain depth-of-cut in plunge grinding.* **Sharp, K.W., Miller, M.H. and Scattergoodc, R.O.** 2000, Precision Engineering, Vol. 24, pp. 220-230.

46. *Grinding forces in regular surface texture generation.* **Stepien, Piotr.** 2007, International Journal of Machine Tools & Manufacture, Vol. 47, pp. 2098-2110.

47. *A survey of recent grinding wheel topography models.* **Doman, D.A., Warkentin, A. and Bauer, R.** 2006, International Journal of Machine Tools & Manufacture, Vol. 46, pp. 343-352.

48. *The importance of abrasive grinding wheel hardness control for the productivity of production grinding operations.* **Bhateja, C. P.** 1, 1981, Annals of the CIRP, Vol. 30, pp. 247-249.

49. *Effect of rearrangement on simulated particle packing.* **Kim, J., Martin, D. M. and Lim, C.** 2002, Powder Technology, Vol. 126, pp. 211-216.

50. *Discrete-particle investigation of friction effect in filling and unsteady/steady discharge in three-dimensional wedge-shaped hopper.* **Balevičius, R., et al.** 2008, Powder Technology, Vol. 187, pp. 159-174.

51. *Simulation of the change of sintering neck between two grains in two dimensions.* **Zhu, Y. Y., et al.** 2006, Acta Metallurgica Sinica, Vol. 19, pp. 397-404.

52. **Shackelford, J. F.** *Introduction to materials science for engineers.* NJ : Upper Saddle River, 2005.

53. *On the mechanics of the grinding process, Part III—thermal analysis of the abrasive cut-off operation.* **Hou, Zhenbing and Komanduri, Ranga.** 2004, International Journal of Machine Tools & Manufacture, Vol. 44, pp. 271-289.

54. *Final report concerning CIRP cooperative work on the characterization of grinding wheel topography.* **Verkerk, J. and Delft, T.** 2, 1977, Annals of the CIRP, Vol. 26, pp. 385-395.

55. *Development of a superabrasive grinding wheel with difined grain structure using kinematic simulation.* **Aurich, J. C., Braun, O. and Wamecke, G.** 1, 2003, Annals of the CIRP, Vol. 52, pp. 275-280.

56. *Stochastic simulation approach to modeling diamond wheel topography.* **Koshy, P., Jain, V. K. and Lal, G. K.** 6, 1997, International Journal of Machine Tools & Manufacture, Vol. 37, pp. 751-761.

57. *A route to highly porous grinding wheels by selective extraction of pore inducers with dense carbon dioxide, Vol. 30: 349–358.* **Davis, T. D., et al.** 2004, Journal of Supercritical Fluids, Vol. 30, pp. 349-358.

58. **Shaw, Milton C.** *Principles of abrasive processing.* s.l. : Oxford Science Publications, 1996.

59. *Recent advances in mechanical microchining.* **Dornfeld, D., Min, S. and Takeuchi, Y.** 2, 2006, Annals of the CIRP, Vol. 55, pp. 745-768.

60. *Energy dissipation in the ultraprecision machining of copper.* **Lucca, D. A., Komanduri, R. and Rhorer, R. L.** 1, 1991, Annals of the CIRP, Vol. 40, pp. 69-72.

61. *Experimental study of micro- and nano-scale cutting of aluminum 7075-T6.* **Ng, Chee Keong, et al.** 2006, International Journal of Machine Tools & Manufacture, Vol. 46, pp. 929-936.

62. *Investigation of micro-cutting operations.* **Chae, J., Park, S.S. and Freiheit, T.** 2006, International Journal of Machine Tools & Manufacture, Vol. 46, pp. 313-332.

63. *Research on microscopic grain-workpiece interaction in grinding through micro-cutting simulation, part 1: mechanism study.* **Li, Xuekun, et al.** 2009, Advanced Materials Research, Vols. 76-78, pp. 9-14.

64. **Systems, Third Wave.** *Third Wave Systems AdvantEdge™ FEM User's Mannual.* Minneapolis, MN : s.n., 2008.

65. *High strain rate shear evaluation and characterization of AISI D2 tool steel in its hardened state.* **Becze, C. E., Worswick, M. J. and Elbestawi, M. A.** 1, 2001, Machining Scinece and Technology, Vol. 5, pp. 131-149.

66. *FEM simulation of orthogonal cutting: serrated chip formation.* **Ceretti, E., Lucchi, M. and Altan, T.** 1999, Journal of Materials Processing Technology, Vol. 95, pp. 17-26.

67. *Effect of grain shape on cutting force in superabrasive single-grit tests.* **Matsuo, T., et al.** 1, 1989, Annals of the CIRP, Vol. 38, pp. 323-325.

68. **Chi, Z.Y.** *Abrasive Machining and Grinding Tool Selection.* Beijing : Weapons Industry Press, 1990. pp. 3-4.

69. *Research on microscopic grain-workpiece interaction in grinding, Part 2 - Factorial Analysis.* **Yan, Lan, et al.** 2009, Advanced Materials Research, Vols. 76-78, pp. 15-20.

70. *Effect of grain shape on cutting force in superabrasive single-grit tests.* **Matsuo, T., et al.** 1, 1989, Annals of the CIRP, Vol. 38, pp. 323-326.

71. *Cutting forces modeling considering the effect of tool thermal property—application to CBN hard turning.* **Huang, Y. and Liang, S. Y.** 3, 2003, International Journal of Machine Tools & Manufacture, Vol. 43, pp. 307-315.

72. *The use of the size effect in grinding for work-hardening.* **Heinzel, C. and Bleil, N.** 1, 2007, Annals of the CIRP, Vol. 56, pp. 327-330.

73. **Elert, Glenn.** Coefficients of Friction for Steel. [Online] http://hypertextbook.com/facts/2005/steel.shtml.

74. *Process modeling in machining. Part I: determination of flow stress data.* **Shatla, Mahmoud, Kerk, Christian and Altan, Taylan.** 2001, International Journal of Machine Tools & Manufacture, Vol. 41, pp. 1511-1534.

75. *An investigation of high speed grinding with electroplated diamond wheels.* **Hwang, T. W., Evans, C. J. and Malkin, S.** 2000, Annals of the CIRP, Vol. 49, pp. 245-248.

76. *Analytical prediction of cutting tool wear.* **Usui, E., Shirakashi, T. and Kitagawa, T.** 1984, Wear, Vol. 258.

77. *Friction, cooling and lubrication in grinding.* **Brinksmeier, E., Heinzel, C. and Wittmann, M.** 2, 1999, Annals of the CIRP, Vol. 48, pp. 581-598.

78. *Predictive modeling of surface roughness in grinding.* **Hecker, Rogelio L. and Liang, Steven Y.** 2003, International Journal of Machine Tools & Manufacture, Vol. 43, pp. 755-761.

79. *A study on the grinding action by single grit.* **Takenaka, Norio.** 1966, Annals of the CIRP, Vol. 13, pp. 183-190.

80. *An investigation on grinding wheel wear in internal grinding.* **Mecheletti, G. F., Filippi, A. De and Ippolito, R.** 1967, Annals of the CIRP, Vol. 14, pp. 433-441.

81. *The application of three-dimensional surface measurement techniques to chracterizing grinding wheel topography.* **Blunt, L. and Ebdon, S.** 11, 1996, International Journal of Machine Tools & Manufacture, Vol. 36, pp. 1207-1226.

82. *Study on surface grinding-hardening of SKD11 hardened steel.* **Chen, M., Li, X. and Yang, P.** 2007, International Journal of Manufacturing Technology and Management, Vol. 12, pp. 236-245.

83. *A comparison of topographic characterization parameters in grinding.* **Terry, Andrew J. and Brown, Christopher A.** 1, 1997, Annals of the CIRP, Vol. 46, pp. 497-500.

84. *Advances in modeling and simulation of grinding processes.* **Brinksmeire, E., et al.** 2, 2006, Annals of the CIRP, Vol. 55, pp. 667-696.

85. *The effect of deformation on the contact area in grinding.* **Rowe, W.B., et al.** 1, 1993, Annals of the CIRP, Vol. 42, pp. 409-412.

86. *What grinding swarf reveals.* **Ramanath, S., Ramaraj, T.C. and Shaw, M.C.** 1, 1987, Annals of the CIRP, Vol. 36, pp. 245-247.

87. *A three-dimensional model for the surface texture in surface grinding, Part 2: Grinding wheel surface texture model.* **Salisbury, Erik J., et al.** 2001, Journal of Manufacturing Science and Engineering, Vol. 123, pp. 582-590.

88. *Simulation of precision grinding process, part 1: generation of the grinding wheel surface.* **Nguyen, T. A. and Butler, D. L.** 2005, International Journal of Machine Tools & Manufacture, Vol. 45, pp. 1321-1328.

89. *Fang, 2003 - Slip-line modeling of machining with a rounded-edge tool - Part I new model and theory.* **Fang, N.** 2003, Journal of the Mechanics and Physics of Solids, Vol. 51, pp. 715-742.

90. *Porous Fine CBN Stones for High Removal Rate Superfinishing.* **Onchi, Y., Matsumori, N. and Ikawa, N.** 1, 1995, Annals of the CIRP, Vol. 44, pp. 291-294.

91. *On the mechanics of the grinding process, Part II—thermal analysis of fine grinding.* **R. Komanduri, Zhenbing Hou.** 2004, International Journal of Machine Tools & Manufacture, Vol. 44, pp. 247-270.